Lehrstuhl für Theoretische Chemie

Ultrafast non-adiabatic nuclear dynamics in systems with strong Jahn-Teller effects

Swarnendu Bhattacharyya

Vollständiger Abdruck der von der Fakultät für Chemie der Technischen Universität München zur Erlangung des akademischen Grades eines Doctors der Naturwissenschaften genehmigten Dissertation.

Vorsitzender:		Univ.-Prof. Steffen J. Glaser
Prüfer der Dissertation:	1.	Univ.-Prof. Dr. Wolfgang Domcke
	2.	Univ.-Prof. Dr. Ville R. I. Kaila

Die Dissertation wurde am 03.12.2015 bei der Technischen Universität München eingereicht und durch die Fakultät für Chemie am 12.01.2016 angenommen.

Contents

Acknowledgement

Foremost, I would like to convey my sincere gratitude to my thesis supervisor Prof. Wolfgang Domcke, for his continuous guidance, patience, enthusiasm and for his immense scientific insight which have always shown me the right path. I would also like to thank him for providing such a pleasant environment to work under the Chair of Theoretical Chemistry.

I am thankful to Dr. Daniel Opalka for a successful collaboration and for many valuable discussions. I am also thankful to many of my friends and colleagues not only for the scientific discussions but also for their support in every respect. Mrs. Mösch needs a special mention for her continuous help, without which it would have been very difficult to manage all the paper works.

Thanks to all my Indian friends in Munich for making my stay in Germany so pleasant. A special mention is needed for Padmadi for her extensive help especially during the beginning days. It would be incomplete if I would not take the opportunity to thank Riddhimanda for being such a special friend, both inside the campus and outside.

Last but not the least, I would like to express my deepest gratitude to my family: my parents for believing in me as I grew up and for giving me all the freedom to follow my dreams, my brother for always being a silent support and my wife for standing by me through all the difficulties of my life.

0. Acknowledgement

Chapter 1

Introduction

The Jahn-Teller (JT) effect, since its emergence in 1937 [1], has remained a key concept in explaining structural instabilities in molecules, complexes and crystals. The JT theorem in its original form, as described by H. A. Jahn and E. Teller [1, 2], reads

"*A configuration of a polyatomic molecule for an electronic state having orbital degeneracy cannot be stable with respect to all displacements of the nuclei unless in the original configuration the nuclei all lie on a straight line.*"

One exception to the above is the so-called *Kramers degeneracy* [3] which cannot be broken by any nuclear displacement since it is enforced by the time-reversal invariance of the Hamiltonian. The original proof of the JT theorem is based on the concepts of perturbation theory and group theoretical symmetry-selection rules. JT effect typically involves strongly interacting electronic states and the Born-Oppenheimer (BO) approximation [4] loses its validity. Different JT coupling mechanisms are often explained in the light of the theory of vibronic coupling and are considered as a special case of the latter.

The so-called conical intersections (CI) [5, 6] are a central concept of vibronic coupling theory which have been employed frequently to explain the ultrafast dynamical processes in photophysics and photochemistry. While the existence of a CI is not, in general, restricted by the fulfilment of any *a priori* symmetry-selection rule, the JT-intersections constitute a special class of CIs where the intersections are symmetry-required and the relative sizes and signs of the JT-coupling constants are determined by symmetry as well.

The idea of the JT effect has also been extended to the more general concept of the so-called pseudo-JT (PJT) effect [7, 8], defined as the interaction of a degenerate electronic state with another energetically close (non-degenerate or degenerate) electronic state through a non-totally symmetric

vibrational mode, which essentially includes a vast majority of vibronic coupling problems [9] and can explain many chemical phenomena arising from the structural instabilities of high-symmetry molecular configurations.

Despite the venerable history of almost 80 years, the JT effect is still an active field of research in chemistry and physics [1, 10–17]. Remarkable developments have been made [18, 19] and are applied successfully to the fields of spectroscopy, stereochemistry and structural phase transitions. Once major inspiration from the JT effect was the discovery of high temperature superconductivity [20], which is recognised by the Nobel Prize in Physics in 1987. Among many other important applications, the JT effect has been found to be instrumental in explaining the properties of fullerenes and the colossal magnetoresistance [21] is also explained in the light of it.

The simplest and the most well-studied JT problem is the so-called $E \times e$ JT effect [9, 18], where the two-fold electronic degeneracy is lifted in first order in displacements along vibrational modes of e symmetry. Traditionally, the Hamiltonian represented in a two-dimensional diabatic electronic basis has been expanded in a Taylor series up to quadratic terms in the vibrational normal modes and has been applied successfully to a number of systems to analyze their spectroscopic properties. However, with the significant advancement of *ab initio* electronic structure methods, the insufficiency of the standard model has gradually been realized. Viel and Eisfeld were the first to treat the $E \times e$ JT [22] and the $(E + A) \times e$ PJT coupling [23] in trigonal systems systematically up to 6th order. However, their procedure, being tedious, becomes essentially impractical for applications in larger point groups. To overcome this difficulty, Opalka and Domcke have applied invariant theory of homogeneous polynomials to construct high-order expansions of the $T_2 \times t_2$ and $T_2 \times e$ JT Hamiltonians in tetrahedral systems [24, 25].

The $E \times e$ JT Hamiltonian has been revisited in the present work to obtain a high-order expansion scheme by employing the invariant theory of homogeneous polynomials [26]. The $(E + A) \times (e + a)$ JT/PJT Hamiltonian in trigonal symmetry serves as a generic JT/PJT problem. Appreciating the fact that the $(E + A) \times (e + a)$ JT/PJT problem in D_{3h} can be considered as a low symmetry analog of the $T_2 \times t_2$ problem in T_d, an arbitrarily high-order expansion has been obtained for the former in the present work [27]. These developed JT/PJT Hamiltonians are then applied to a series of radical cations to construct highly accurate PE surfaces and the effects of the high-order coupling terms have been assessed in the simulated vibronic spectra [28].

As a result of many investigations in the past two to three decades, the concept of CIs has now become a natural language for the description of the non-adiabatic dynamics in the excited molecular electronic states [5, 6]. They

are often found indispensable for the microscopic explanation of, for example, internal conversion, photostability, photoisomerization and photodissociation processes. Quenching of fluorescence from the excited state is explained, in many cases, by the existence of an ultrafast internal conversion process through an energetically accessible CI. This non-radiative decay of the excited state, typically occurring in a femtosecond timescale, is much faster than the radiative process (fluorescence) and the quantum yield of the latter often drops below the detection threshold ($\approx 10^{-4}$).

The earliest study of the dynamics at CIs goes back to 1932, where the Landau-Zener-Stückelberg approach [29–31] provided a recipe to understand the one-dimensional avoided crossing situations. However, its extension to multi-dimensional cases was not straightforward. Full-dimension quantum dynamical studies reach a bottleneck quite quickly with increasing system size. Fortunately, from several decades of research, it has been understood that in most cases a reduction in the dimensionality, consisting of a few strongly coupled vibrational modes, is sufficient in explaining an efficient ultrafast electronic-population transfer through CIs [9, 32]. However, as an artifact of reduced dimensional calculations, the system is left with a large excess vibrational energy at the end of the initial fast dynamics, which can only be dissipated if there exists a coupling mechanism between the active and the less-active modes (or with an environment). The system-bath formulation employing the reduced density matrix formalism has been used very successfully to incorporate the effect of a dissipative environment on the dynamics through CIs, especially when the system-bath interaction time is considerably larger than the fast internal conversion dynamics [33, 34]. Another possibility is the employment of numerical techniques specially designed for the solution of the TDSE for the high-dimensional quantum systems. The multiconfiguration time dependent Hartree (MCTDH) method is a major breakthrough in this area [35, 36].

The exploitation of the high symmetry often simplifies the understanding of the complex excited-state dynamics of JT-active systems. This does not always apply to larger bio-organic chromophores typically having lower symmetry. Therefore, small representative JT systems, with rich dynamic properties, serve as ideal test-beds for different dynamical approximations and may help achieve a better microscopic understanding of the ultrafast vibronic dynamics in general. Several studies on the JT-induced excited-state dynamics have frequently demonstrated ultrafast deactivations typically falling in the fs timescale. To mention a few examples, Mahapatra and co-workers have thoroughly studied the dynamics of the cyclopropane radical cation in its excited electronic states and an internal conversion rate of ≈ 10 fs has been reported [37]. The complex multi-state multi-mode dynamics of

benzene radical cation and its mono and poly-fluorinated derivatives have been investigated by Köppel and co-workers employing the MCTDH method [38]. Along with accurately simulating the photoelectron spectra and mass analyzed threshold ionization (MATI) spectra, they have also calculated the electronic population dynamics of the ground and excited states and it has been shown that different non-radiative transitions occur, ranging from 20 fs to 200 fs [39]. Another particularly interesting and well-studied example is the H_3 system, where the electronic population of the JT-split upper component of the $\tilde{X}E'$ state decays to the lower one within the extremely short timescale of only $\approx 3-6$ fs, which is possibly the fastest known internal conversion process [40]. Quantum dynamical calculations performed in the present work demonstrate that the seam of JT/PJT-induced CIs induce a series of truly ultrafast electronic transitions from the excited states to the ground state in the NH_3^+ and PH_3^+ cations, which occur within the range of 5-20 fs [41, 42].

Chapter 2

Theoretical background

2.1 Born-Oppenheimer approximation and adiabatic and diabatic representations

The Born-Oppenheimer (BO) approximation [4, 43], since its advent in 1927, has played the central role in molecular physics and chemistry. Its elegance lies in the fact that it allows an approximate separation of the nuclear and electronic motions in molecular systems. The validity of this idea arises from the large difference between the mass of a typical nucleus and that of an electron. The BO picture is in general accurate, especially when the molecule moves on a single energetically isolated potential-energy (PE) surface, where the faster electrons can instantaneously follow any change in the configuration of the slower nuclei. There exist mainly three variations of the approximation in the literature which are slightly different from one another. Following the nomenclature of Ballhausen and Hansen [44, 45], we call them (1) *Born-Oppenheimer adiabatic approximation*, (2) *Born-Huang adiabatic approximation* and (3) *crude adiabatic approximation*.

The molecular Schrödinger equation reads

$$H\Psi(\boldsymbol{r}, \boldsymbol{R}) = E\Psi(\boldsymbol{r}, \boldsymbol{R}) \tag{2.1}$$

where $\Psi(\boldsymbol{r}, \boldsymbol{R})$ and E are the eigenfunctions and the eigenvalues, respectively, of the molecular Hamiltonian H which is written (at the non-relativistic level) as

$$\begin{aligned} H &= T_n + T_e + U(\boldsymbol{r}, \boldsymbol{R}) \\ &= T_n + H_e \end{aligned} \tag{2.2}$$

where T_n and T_e are the kinetic energy operators of the nuclei and the electrons, respectively. $U(\boldsymbol{r}, \boldsymbol{R})$ is the combined PE of all the electrons and the

nuclei. The vectors $\boldsymbol{R}$ and $\boldsymbol{r}$ represent, respectively, the set of electronic and the nuclear coordinates. H_e is the electronic Hamiltonian which describes the motion of electrons in a molecule with fixed nuclei. The eigenvalues $V_i(\boldsymbol{R})$ and the eigenfunctions $\Phi_i(\boldsymbol{r}, \boldsymbol{R})$ of H_e depend parametrically on $\boldsymbol{R}$ which satisfy the electronic Schrödinger equation

$$H_e\Phi_i(\boldsymbol{r}, \boldsymbol{R}) = V_i(\boldsymbol{R})\Phi_i(\boldsymbol{r}, \boldsymbol{R}). \tag{2.3}$$

The set $\{\Phi_i(\boldsymbol{r}, \boldsymbol{R})\}$ forms a complete basis in the electronic Hilbert space for any value of $\boldsymbol{R}$, i. e.,

$$\sum_i |\Phi_i(\boldsymbol{r}, \boldsymbol{R})\rangle\langle\Phi_i(\boldsymbol{r}, \boldsymbol{R})| = \mathbf{1} \tag{2.4}$$

where $\mathbf{1}$ is the identity operator. The completeness of the electronic basis enables one to expand the total molecular wavefunction $\Psi(\boldsymbol{r}, \boldsymbol{R})$ in terms of the electronic eigenfuntions as

$$\Psi(\boldsymbol{r}, \boldsymbol{R}) = \sum_i \Phi_i(\boldsymbol{r}, \boldsymbol{R})\chi_i(\boldsymbol{R}). \tag{2.5}$$

Eq. (2.5) is known as the *Born-Oppenheimer expansion* [43].

Inserting *ansatz* (2.5) into Eq. (2.1), multiplying from the left by $\Phi_j^*(\boldsymbol{r}, \boldsymbol{R})$ and integrating over $\boldsymbol{r}$ one obtains the coupled equations for the expansion coefficients $\chi_i(\boldsymbol{R})$

$$[T_n + V_j(\boldsymbol{R}) - E]\chi_j(\boldsymbol{R}) = \sum_i \Lambda_{ji}\chi_i(\boldsymbol{R}) \tag{2.6}$$

where the so-called non-adiabatic couplings (NAC) Λ_{ji} are given by

$$\Lambda_{ji} = \delta_{ji}T_n - \int d\boldsymbol{r}\Phi_j^*(\boldsymbol{r}, \boldsymbol{R})T_n\Phi_i(\boldsymbol{r}, \boldsymbol{R}). \tag{2.7}$$

If the nuclear kinetic-energy operator is taken to be of the general form [46]

$$T_n = -\sum_{m,n=1}^{M} \frac{\partial}{\partial R_m}\alpha_{mn}(\boldsymbol{R})\frac{\partial}{\partial R_n}, \tag{2.8}$$

each of the NAC decomposes into a differential operator and a c-number in $\boldsymbol{R}$ space

$$\Lambda_{ji} = \boldsymbol{F}_{ji} \cdot \boldsymbol{\nabla} + G_{ji} \tag{2.9}$$

The elements of the derivative coupling vector are given by

$$\boldsymbol{F}_{ji}^{(m)}(\boldsymbol{R}) = 2\sum_{n=1}^{M}\int d\boldsymbol{r}\Phi_j^*(\boldsymbol{r},\boldsymbol{R})\alpha_{mn}\frac{\partial}{\partial R_n}\Phi_i(\boldsymbol{r},\boldsymbol{R}) \tag{2.10}$$

and the scalar couplings take the form

$$G_{ji}(\boldsymbol{R}) = \int d\boldsymbol{r}\Phi_j^*(\boldsymbol{r},\boldsymbol{R})(T_n\Phi_i(\boldsymbol{r},\boldsymbol{R})). \tag{2.11}$$

Neglecting all the elements of the non-adiabatic coupling matrix $\boldsymbol{\Lambda}$, one obtains the well-known *Born-Oppenheimer adiabatic approximation*. Under this approximation, it is possible to separate electronic and nuclear coordinates completely and the total wavefunction can be expressed as a product of the nuclear and the electronic wavefunctions

$$\Psi(\boldsymbol{r},\boldsymbol{R}) = \chi_i(\boldsymbol{R})\Phi_i(\boldsymbol{r}). \tag{2.12}$$

A similar but slightly improved representation is obtained by retaining only the diagonal terms of $\boldsymbol{\Lambda}$, where the electronic wavefunctions remain unchanged but PE surfaces are slightly refined in energy by the additional $G_{ii}(\boldsymbol{R})$ term. Notice here that by virtue of being an anti-hermitian matrix ($\boldsymbol{F}^\dagger = -\boldsymbol{F}$), the diagonal elements of $\boldsymbol{F}$ are all zero if the electronic wavefunctions are assumed to be real. This is known as *Born-Huang adiabatic approximation*.

The third alternative approximation is obtained by solving the electronic Schrödinger equation for nuclei fixed at some suitably chosen reference configuration ($\boldsymbol{R_0}$)

$$H_e^0\Phi_i^0(\boldsymbol{r},\boldsymbol{R_0}) = V_i^0(\boldsymbol{R_0})\Phi_i^0(\boldsymbol{r},\boldsymbol{R_0}). \tag{2.13}$$

where

$$H_e^0 = H_e - \Delta U(\boldsymbol{r},\boldsymbol{R}). \tag{2.14}$$

The molecular wavefunction, when expressed in terms of $\{\Phi_i^0(\boldsymbol{r},\boldsymbol{R_0})\}$, takes the form

$$\Psi(\boldsymbol{r},\boldsymbol{R}) = \sum_i \Phi_i^0(\boldsymbol{r},\boldsymbol{R_0})\chi_i^0(\boldsymbol{R}) \tag{2.15}$$

where the expansion coefficients, $\chi_i^0(\boldsymbol{R})$, are of course different than those in Eq. (2.5). The coupled equations for $\chi_i^0(\boldsymbol{R})$ reads

$$[T_n + V_j^0(\boldsymbol{R_0}) + \Delta U_{jj}(\boldsymbol{R}) - E]\chi_j^0(\boldsymbol{R}) + \sum_{i\neq j}\Delta U_{ji}(\boldsymbol{R})\chi_i^0(\boldsymbol{R}) = 0 \tag{2.16}$$

where

$$\Delta U_{ji}(\boldsymbol{R}) = \langle \Phi_j^0(\boldsymbol{r}, \boldsymbol{R_0}) | \Delta U(\boldsymbol{r}, \boldsymbol{R}) | \Phi_i^0(\boldsymbol{r}, \boldsymbol{R_0}) \rangle. \tag{2.17}$$

As long as $\{\Phi_i^0(\boldsymbol{r}, \boldsymbol{R_0})\}$ is a complete set in electronic space, Eq. (2.16) is totally equivalent to *ansatz* (2.5). However, if we assume that the off-diagonal elements, $\Delta U_{ji} (j \neq i)$ are negligible, then the total wavefunction becomes

$$\Psi(\boldsymbol{r}, \boldsymbol{R}) = \Phi_i^0(\boldsymbol{r}, \boldsymbol{R_0}) \chi_i^0(\boldsymbol{R}) \tag{2.18}$$

and the corresponding potential-energy surface is given by

$$V_i'(\boldsymbol{R}) = V_i^0(\boldsymbol{R_0}) + \Delta U_{ii}(\boldsymbol{R}) \tag{2.19}$$

This approximation is known as *crude adiabatic approximation*. The crude adiabatic approximation is connected to the Born-Oppenheimer adiabatic approximation through the *Herzberg-Teller expansion* [47] which incorporates the $\boldsymbol{R}$-dependence of the electronic wavefunction through a perturbative treatment of $\boldsymbol{\Delta U}$. Despite its limitations, the *crude adiabatic approximation* is historically important for being employed to interpret various phenomena, including intensity borrowing [48], Jahn-Teller effect [49], vibronic coupling [45] and resonance Raman spectra [50].

While the above approximations are proved to be good in many cases, there exist ample situations, which have become standard examples in the past two to three decades, where the adiabatic approximations cannot give the correct picture [5, 9, 32]. The situation can be explained by considering the off-diagonal elements of the derivative coupling matrix which can be expressed (after some straightforward algebra) as an *off-diagonal analogue* of the Hellmann-Feynman theorem:

$$\boldsymbol{F}_{ji}(\boldsymbol{R}) = \frac{\langle \Phi_j(\boldsymbol{r}, \boldsymbol{R}) | \boldsymbol{\nabla} H_e | \Phi_i(\boldsymbol{r}, \boldsymbol{R}) \rangle}{V_i(\boldsymbol{R}) - V_j(\boldsymbol{R})}. \tag{2.20}$$

Eq. (2.20) clearly shows that when the denominator becomes smaller than a vibrational quantum, the non-adiabatic couplings (Λ_{ji}) no longer remain negligible and play a significant role in Eq. (2.6). Of special interest are the situations where two PE surfaces become exactly degenerate, the so-called *conical intersections*, where the right hand side of Eq. (2.20) becomes a singular function of nuclear coordinates and the adiabatic approximation breaks down completely [9]. At CIs, the adiabatic electronic wavefunctions become discontinuous, making it very cumbersome to study the quantum dynamics of the nuclei in the adiabatic representation. However, for practical purposes, one usually deals with a rather small subset of electronic states which are

vibronically coupled strongly to each other when the members of the complementary set of electronic states is energetically sufficiently apart. Within this manifold of interacting electronic states there is always a freedom of choice for the electronic basis. A unitary transformation, applied simultaneously to the adiabatic electronic basis and the nuclear basis vectors, which leaves the total wavefunction invariant

$$\Psi = \boldsymbol{\chi}^\dagger \boldsymbol{\Phi} = \boldsymbol{\chi}^\dagger \boldsymbol{U}^\dagger \boldsymbol{U} \boldsymbol{\Phi} = (\boldsymbol{U}\boldsymbol{\chi})^\dagger (\boldsymbol{U}\boldsymbol{\Phi}) = \tilde{\boldsymbol{\chi}}^\dagger \tilde{\boldsymbol{\Phi}} \tag{2.21}$$

can provide the so-called *diabatic basis* which are weakly dependent functions of the nuclear coordinates and in which the derivative coupling (ideally) vanishes [51–54]. In the diabatic basis, the derivative coupling matrix undergoes a transformation known as *local gauge transformation* [55]

$$\tilde{\boldsymbol{F}} = \boldsymbol{U}^\dagger \boldsymbol{F} \boldsymbol{U} + \boldsymbol{U}^\dagger (\nabla \boldsymbol{U}). \tag{2.22}$$

If we restrict ourselves to a two-state problem, the coordinate-dependent adiabatic-to-diabatic transformation matrix can be written as

$$\boldsymbol{U}(\boldsymbol{R}) = \begin{pmatrix} \cos\alpha(\boldsymbol{R}) & \sin\alpha(\boldsymbol{R}) \\ -\sin\alpha(\boldsymbol{R}) & \cos\alpha(\boldsymbol{R}) \end{pmatrix}. \tag{2.23}$$

Using this definition of $\boldsymbol{U}(\boldsymbol{R})$, it is easy to show that the single non-zero element of the $\boldsymbol{F}$ matrix ($\boldsymbol{F}_{12} = -\boldsymbol{F}_{21}$) is represented in the diabatic basis as

$$\tilde{\boldsymbol{F}}_{12} = \boldsymbol{\nabla}\alpha(\boldsymbol{R}) + \boldsymbol{F}_{12} \tag{2.24}$$

The vanishing of the derivative couplings in the diabatic representation leads to the equation

$$\boldsymbol{\nabla}\alpha(\boldsymbol{R}) = -\boldsymbol{F}_{12}. \tag{2.25}$$

In order to achieve a well-defined solution of the above equation, one must fulfill the *curl condition*

$$\boldsymbol{\nabla} \times \boldsymbol{F}_{12} = 0. \tag{2.26}$$

As has been pointed out by Mead and Truhlar, apart from the trivial case of diatomics, there is no solution to the above equation in general for polyatomic molecules [56].

However, a number of schemes has been constructed with an aim to minimize the derivative couplings which gives rise to the so-called *quasidiabatic* states. A criterion for quasidiabaticity, as has been proposed by Cederbaum and co-workers [55], is given by

$$\boldsymbol{\nabla} \cdot \tilde{\boldsymbol{F}}_{12} = 0. \tag{2.27}$$

In an optimally diabatic basis, the nuclear kinetic energy is (nearly) diagonal and the PE matrix has off-diagonal coupling terms

$$\tilde{\boldsymbol{V}} = \boldsymbol{U}^{\dagger}\boldsymbol{V}\boldsymbol{U} \tag{2.28}$$

which in the case of two electronic states takes the form

$$\tilde{\boldsymbol{V}} = \frac{V_1 + V_2}{2}\mathbf{1} + \frac{V_1 - V_2}{2}\begin{pmatrix}\cos(2\alpha) & \sin(2\alpha) \\ \sin(2\alpha) & -\cos(2\alpha)\end{pmatrix}. \tag{2.29}$$

2.2 Jahn-Teller and pseudo-Jahn-Teller effects: conventional approach

The JT theorem states that a non-linear molecule in a symmetry-induced orbitally degenerate electronic state is unstable with respect to spontaneous distortions along certain non-totally symmetric vibrational modes, Kramers degeneracy being an exception [1, 2]. While it may be considered a special case of general vibronic coupling theory, the JT effect was discovered long before the development of vibronic coupling theory and actually many aspects of vibronic coupling had already been introduced by JT theory [9]. The conventional formulation of the various JT Hamiltonians relies on the availability of a (sufficiently) diabatic electronic basis and can be split into the following steps

1. Representation of the Hamiltonian operator in the diabatic electronic basis.

2. Expansion of the PE operator in a Taylor series at the reference geometry of high symmetry.

3. Use of symmetry selection rules to determine the non-vanishing matrix elements.

Following the above recipe, the JT Hamiltonian matrix elements take the general form

$$\mathcal{H}_{\alpha\beta} = H_0\delta_{\alpha\beta} + \sum_i \left(\frac{\partial V_{\alpha\beta}}{\partial Q_i}\right)_0 Q_i + \sum_{i,j}\left(\frac{\partial^2 V_{\alpha\beta}}{\partial Q_i \partial Q_j}\right)_0 Q_i Q_j + \cdots \tag{2.30}$$

where

$$V_{\alpha\beta} = \langle\tilde{\Phi}_\alpha|V|\tilde{\Phi}_\beta\rangle \tag{2.31}$$

are the matrix elements of the PE operator in the diabatic electronic basis, $Q_i (i = 1, \ldots, n)$ are the normal modes of vibration and H_0 is the zero-order term of the Taylor series and often approximated by an n-dimensional isotropic harmonic oscillator. In the standard model of JT theory the Taylor expansion is truncated, in most of the cases, after the linear or the quadratic terms [17–19].

While the above prescription is essentially identical to the construction of vibronic coupling Hamiltonians in its general form, the relative sizes and signs of the JT coupling constants are strictly determined by symmetry. The proof of the JT theorem rests on group theory. The symmetries of the JT-active vibrational modes are determined by the requirement that the irreducible representation of the vibrational mode (Γ_{vib}) must be included in the symmetrized direct product of the irreducible representation (Γ_{el}) of the degenerate electronic manifold

$$[\Gamma_{el}]^2 \supset \Gamma_{vib}. \tag{2.32}$$

The so-called $E \times e$ JT effect is the most well-studied JT problem in the literature [9, 10, 18]. This JT model demonstrates that the two-fold electronic degeneracy (E) is lifted in first order in displacements along the vibrational modes of e symmetry if the molecule contains at least one three-fold principal axis of rotation. The $E \times e$ JT Hamiltonian in the liner-plus-quadratic approximation may conveniently be expressed in the complex electronic basis and complex vibrational coordinates as

$$\mathcal{H} = [-\frac{\hbar\omega}{2\rho^2}\left(\rho\frac{\partial}{\partial\rho}\rho\frac{\partial}{\partial\rho} + \frac{\partial^2}{\partial\varphi^2}\right) + \frac{1}{2}\hbar\omega\rho^2]\mathbf{1} + [\kappa\rho e^{i\varphi} - \frac{1}{2}g\rho^2 e^{-2i\varphi}]\boldsymbol{\sigma}_x \tag{2.33}$$

where $\mathbf{1}$ is the two-dimensional identity matrix and $\boldsymbol{\sigma}_x$ is one of the Pauli matrices. The new complex bases of the electronic states and the vibrational modes are related to the old ones as

$$\begin{aligned} |\tilde{\Phi}_\pm\rangle &= \frac{1}{\sqrt{2}}\left(|\tilde{\Phi}_x\rangle \pm i|\tilde{\Phi}_y\rangle\right) \\ Q_\pm &= Q_x \pm iQ_y = \rho e^{\pm i\varphi}. \end{aligned} \tag{2.34}$$

Diagonalization of the PE part gives the adiabatic PE surfaces. For vanishing quadratic coupling ($g = 0$), this yields

$$V_\pm = \frac{1}{2}\hbar\omega\rho^2 \pm \kappa\rho. \tag{2.35}$$

The shape of $V_\pm$ as functions of the nuclear coordinates $Q_\pm$ is often referred to as *mexican hat*, see Fig. 2.1. The azimuthal symmetry of the adiabatic

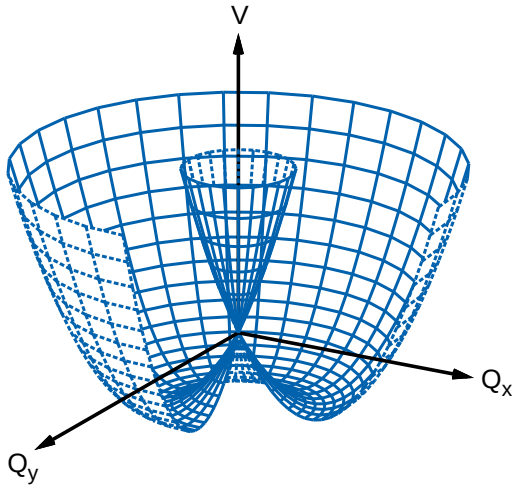

Figure 2.1: The *Mexican hat* shape of the $E \times e$ JT PE surfaces which includes only linear JT coupling terms: a perspective drawing.

potentials reflects the existence of an additional constant of motion, the so-called *vibronic angular momentum*

$$\boldsymbol{J} = \hbar \begin{pmatrix} -\frac{1}{2} + \frac{1}{i}\frac{\partial}{\partial\varphi} & 0 \\ 0 & \frac{1}{2} + \frac{1}{i}\frac{\partial}{\partial\varphi} \end{pmatrix} \tag{2.36}$$

which commutes with the linear $E \times e$ JT Hamiltonian. However, the rotational symmetry is broken upon addition of the quadratic JT coupling terms and the lower sheet of the adiabatic PE surface exhibits three equivalent minima separated by three equivalent saddle points which reflects the three-fold rotational symmetry of the system. The vibronic angular momentum quantum number is no longer a good quantum number.

For real molecular systems, there are often other electronic states sufficiently close in energy to the E state which can vibronically interact with the latter, leading to the so-called *pseudo-Jahn-Teller effect* [9, 18]. For example, in trigonal systems, a close lying non-degereate A state can couple to an E state through the same JT-active e vibrational mode, giving the so-called $(A+E)\times e$ PJT effect, which is the simplest of its kind. In a similar notation as above, the linear $(A + E) \times e$ PJT coupling Hamiltonian, which includes

the JT interaction within the E state as a part of it, is given by

$$\mathcal{H} = H_0\mathbf{1} + \begin{pmatrix} E_A & \lambda Q_x & \lambda Q_y \\ \lambda Q_x & E_E + \kappa Q_x & \kappa Q_y \\ \lambda Q_y & \kappa Q_y & E_E - \kappa Q_x \end{pmatrix}, \tag{2.37}$$

where λ is the linear PJT coupling constant, E_A and E_E are the energies of the A and the E states at the reference geometry, respectively and $\mathbf{1}$ is the 3-dimensional unit matrix. For the limiting case of vanishing linear JT coupling ($\kappa = 0$), the PE surfaces exhibit rotational symmetry and two of three eigenvectors of the Hamiltonian exhibit a *glancing intersection* where the degeneracy is lifted in second order. However, for $\kappa \neq 0$, the linear JT+PJT model shares many features with the quadratic $E \times e$ JT model. In presence of both types of interaction, the cylindrical symmetry of the PE surface is replaced by a three-fold rotational symmetry and in addition to the JT CI, three additional CIs occur within the electronic manifold, which has also been observed in pure $E \times e$ JT problems for sufficiently large quadratic JT coupling constant. While the low-energy vibronic dynamics does not show geometric phase effects (unlike JT situation) in pure PJT case, the situation becomes complicated if both types of couplings are important and the final outcome depends on the competition between them. Finally, the existence of a totally symmetric mode, which modulates the $E - A$ energy gap, may lead to a triple CI at the reference geometry [17].

2.3 Theory of invariant polynomials and Jahn-Teller potential-energy surfaces

The exploitation of symmetry in quantum mechanics is carried out with the help of the powerful tools of group theory [57]. The symmetry of molecules and clusters has been classified by the 32 different molecular point groups. However, there exist instances where multiple molecular point groups are isomorphic to one more general abstract algebraic group. This isomorphism indicates the existence of redundancies in the construction of molecular point groups. Ascher and Gay have pointed out that there exist only 17 different molecular point groups and the number of different matrix groups of the irreducible representations can be further reduced to only 14 [58, 59]. Naturally, the exploitation of the algebraic properties of the abstract groups underlying the regular molecular point symmetry groups facilitates the construction of symmetry-adapted molecular PE surfaces.

The established description of the JT effect relies on the symmetry of the irreducible representations of the molecular point group defined at the

configuration of highest symmetry. It will be shown below that in many cases of interest the irreducible representations of the molecular point groups (matrix groups) are isomorphic to those of the permutation symmetry groups. Therefore, the methods of invariant algebra can be employed for the efficient derivation of JT Hamiltonians.

The potential-energy (PE) surfaces of polyatomic molecules containing N identical nuclei are subject to permutational invariance of like nuclei. The permutations of the identical nuclei in a molecule form a group, the so-called *Complete Nuclear Permutation* (CNP) group which is nothing but the symmetry group of N identical nuclei (S_N) [60]. Being a proper subgroup of the full symmetry group of the molecular system, the elements of the CNP group commute with the Hamiltonian. In case of several sets of identical nuclei in the same molecule, the CNP group of the molecule is given by the direct product of the symmetry groups of the different smaller sets

$$S_N = S_{N_1} \times S_{N_2} \times S_{N_3} \times \cdots \tag{2.38}$$

Sometimes, it becomes necessary to include another group of order 2, known commonly as the inversion group, to the above construction and the resulting symmetry group is then called the *Complete Nuclear Permutation Inversion* (CNPI) group of the molecule [60]. The molecular point group, on the other hand, is defined (locally) if a well-defined equilibrium geometry exists in a certain region of the PE surface. In recent years, the exploitation of permutation symmetry has been of increasing interest in the construction of analytic representations of global PE surfaces. Polynomials, invariant in the CNP group, have been employed to form a set of invariant functions which provide an approximation space for analytic PE surfaces.

To proceed further we need to define a linear representation (Γ) of a finite abstract group (G) on an n-dimensional vector space (V) over the field of real numbers, which can be expressed mathematically as $\Gamma : G \to GL(n, \mathbb{R})$. We are interested in the set of homogeneous polynomials which are invariant under the action of the group G. All such polynomials form the ring of invariants and is denoted as $\mathbb{R}[V]^G$. The invariance of a polynomial $p(\boldsymbol{v})$ under G is defined as

$$\sigma \circ p(\boldsymbol{v}) = p(\sigma^{-1}\boldsymbol{v}) = p(\boldsymbol{v}) \tag{2.39}$$

where σ represents the matrices (in the representation Γ) corresponding to the elements of the group G and $\boldsymbol{v}$ is an element of the underlying vector space V. From Eq. (2.39), it is clear that the evaluation of the group action on the polynomials requires the matrix representations of the elements of the group. The generating set of polynomials invariant under the action of a

finite linear group G can be efficiently calculated by the successive application of the *Reynolds operator* [61] (which is a G-invariant projection) to all terms of a general polynomial expansion

$$\mathcal{R}(p) = \frac{1}{|G|} \sum_{\sigma \in G} \sigma \circ p, \tag{2.40}$$

where $|G|$ represents the order of the group G. It is interesting to note that the Reynolds operator is essentially the well-known projection operator in molecular group theory [57]. It should be emphasized that, inspite of its simplicity, the application of the Reynolds operator is limited to groups of low orders. The computational cost for the symmetric group S_N scales with the factorial of the identical nuclei (N) and the number of monomials that have to be included for an expansion of degree d in n coordinates is given by

$$\binom{d+n}{d} = \frac{1}{d!}(n+1)^{d-1} \tag{2.41}$$

which also indicates an exponential scaling with respect to the degree of expansion.

Hilbert has given the proof that the ring of invariant polynomials $\mathbb{R}[V]^G$ under the group G is finitely generated by the generating set of homogeneous invariant polynomials $(p_1, \cdots, p_r)$ which is a subset of $\mathbb{R}[V]^G$ (*Hilbert's finiteness theorem*) [62], i. e.,

$$\mathbb{R}[V]^G = \mathbb{R}[p_1, \cdots, p_r]. \tag{2.42}$$

The *generating* set of polynomials refer to a set polynomials that generates all the other members of the invariant ring. Another important theorem of classical invariant theory states that the generating set of invariants has an *a priori* upper bound of their degree which is given by the order of the group, $|G|$ (*Noether degree bound*) [63]. However, for many of the groups, which are relevant in Physics and Chemistry, the degree-bound is considerably lower than $|G|$. There exist several computer algebra systems which are specialized for the computation of the generating set of invariants. The `Singular` software-suite have been employed throughout this work [64, 65].

The linearly independent elements of $\mathbb{K}[p_1, \cdots, p_r]$ form a vector space and the adiabatic PE surface can be approximated by restricting the expansion up to a certain order [66]. In the case of a single PE surface, defined by $\langle \Phi | \mathcal{H}_{el} | \Phi \rangle$, where $|\Phi\rangle$ is an adiabatic electronic state, the Hamiltonian $\mathcal{H}_{el}$ is a totally symmetric function of nuclear coordinates and the electronic potential energy is invariant under symmetry operations. For a single (non-degenerate) PE surface, the adiabatic electronic energy can be represented

in terms of invariant polynomials of nuclear coordinates. Multi-sheeted intersecting adiabatic PE surfaces, on the other hand, cannot be approximated by polynomial expansions due to the presence of cusps at CIs. Therefore, a representation of the multi-sheeted PE surface in a diabatic basis must be found to express the elements of the diabatic PE matrix as smooth functions of the nuclear coordinates.

The adiabatic electronic wave functions of a manifold of m intersecting electronic PE surfaces can be represented as superpositions in an m-dimensional diabatic basis, which forms an electronic Hilbert sub-space. Assuming that all other electronic states are sufficiently far apart in energy, the wave function is written as

$$|\Phi\rangle = \sum_{i=1}^{m} c_i |\tilde{\Phi}_i\rangle \tag{2.43}$$

where the $|\tilde{\Phi}_i\rangle$ are diabatic electronic states. The expectation value of the electronic Hamiltonian in the adiabatic representation, which must be invariant under the group G, can be expressed as a function of nuclear coordinates and coefficients in terms of the diabatic electronic basis as

$$\begin{aligned} \langle \mathcal{H}_{el} \rangle &= \langle \Phi | \mathcal{H}_{el} | \Phi \rangle \\ &= \sum_{i,j} c_i \langle \tilde{\Phi}_i | \mathcal{H}_{el} | \tilde{\Phi}_j \rangle c_j \\ &= \sum_{i,j} c_i (\mathcal{H}_{el})_{ij} c_j. \end{aligned} \tag{2.44}$$

Thus the energy expectation value is quadratic in the electronic coefficients and $(\mathcal{H}_{el})_{ij}$, which are the matrix elements of the electronic Hamiltonian in the diabatic electronic basis and thus smooth functions of nuclear coordinates, can be expanded in terms of polynomials in symmetry-adapted nuclear coordinates. To compute the symmetry-adapted matrices for the expansion of the electronic Hamiltonian, one has to find the invariant polynomials of the group representation in the combined vector space of the electronic coefficients and the nuclear coordinates ($V^{el} \oplus V^{nu}$). In other words, the problem reduces to finding the second-order invariants in the vector space V^{el} and the invariant polynomials of arbitrary order in the vector space V^{nu} of the symmetry-adapted nuclear coordinates. Once the generators of the invariant ring $(\mathbb{R}[V^{el} \oplus V^{nu}]^{\Gamma^{el} \oplus \Gamma^{nu}})$ are known, it is straightforward to obtain all invariant polynomials of degree two in the electronic space and determining the corresponding matrix elements. The PE matrices of arbitrarily high orders can then be conveniently obtained by multiplying these second order matrices with an element of $\mathbb{R}[V^{nu}]^{\Gamma^{nu}}$ which is of appropriate order.

The most transparent case arises when the nuclear and electronic basis functions transform according to the same irreducible representation, such as in the $E \times e$ and $T_2 \times t_2$ JT effects. In this case, the nuclear coordinates and electronic states form identical vector spaces and their matrix group representations are also identical in both coordinate spaces ($\Gamma^{el} = \Gamma^{nu}$). Weyl's polarization method can then be used to obtain the generating polynomials from the generators of the invariant ring of a single copy of these [58, 59, 67]. As Weyl's polarization operator is a linear differential operator, it can be easily shown that the formulation JT vibronic matrices reduces to the computation of the Hessian (with respect to the electronic degrees of freedom) of the invariant polynomials [24, 25]. This feature is further elucidated in Appendix 1.

2.4 Non-adiabatic quantum dynamics and simulation of photoelectron spectra

2.4.1 Photoelectron spectra, autocorrelation function and electronic population probabilities

The quantal motion of the nuclei in a molecule can most conveniently be described by solving the time-dependent Schrödinger equation (TDSE) [68]. However, it must be kept in mind that for a time-independent Hamiltonian, the knowledge of the wave-packet at all times and the knowledge of all the eigenstates of the Hamiltonian are completely equivalent. The preference of the time-dependent method over the time-independent one or the opposite depends on the particular problem being solved. The JT PE surfaces employed in the dynamical calculations carried out in the present work typically involve multiple intersecting electronic PE surfaces and high-order expansions of the PE function with respect to the vibrational modes, which makes the solution of the time-independent Schrödinger equation (TISE) extremely computationally demanding and time-dependent methods appear to be the obvious choice. Moreover, if one is interested in the observables which depend on the short time dynamics of the system, as is the case for the low-resolution photoelectron spectra, time-dependent approach is certainly preferable. Throughout, we have relied on the so-called *pseudospectral* representation where the PE matrix is diagonal and is evaluated only on a finite set of discrete grid points making the representation of the Hamiltonian particularly simple for JT systems.

In the time-dependent formalism of molecular spectroscopy, the spectral

intensity distribution function is defined as the Fourier transform of the *autocorrelation function* [68, 69]

$$P(\omega) = \frac{1}{2\pi}\int_{-\infty}^{\infty} C(t)e^{i\omega t}dt, \tag{2.45}$$

where the autocorrelation function $C(t)$ is given by

$$C(t) = \langle\Psi(x,0)|\Psi(x,t)\rangle. \tag{2.46}$$

In Eq. 2.46, $|\Psi(0)\rangle$ is the initial wave packet and $|\Psi(t)\rangle$ is obtained by solving the TDSE

$$i\hbar\frac{\partial}{\partial t}|\Psi(x,t)\rangle = \hat{H}|\Psi(x,t)\rangle. \tag{2.47}$$

Since last three decades a number of methods have been proposed to obtain the $|\Psi(x,t)\rangle$ by efficiently solving the TDSE and thus to calculate the autocorrelation function. Two of them, which have been employed in the present work, are discussed below.

Considering the fact that the property of interest in this work is the photoelectron spectrum, the efficiency of the calculation can be improved considerably if the initial wave packet is real and the Hamiltonian is symmetric, as then

$$\begin{aligned} C(t) &= \langle\Psi(\boldsymbol{S},0)|\Psi(\boldsymbol{S},t)\rangle \\ &= \langle\Psi^*(\boldsymbol{S},t/2)|\Psi(\boldsymbol{S},t/2)\rangle. \end{aligned} \tag{2.48}$$

This means that the autocorrelation function is obtained over twice the time of propagation which in turn increases the resolution of the spectrum by a factor of two without any additional computational expanse. This has also indirect effects, as shorter propagations reach convergence easily and the initial wave packet does not need to be stored. However, finite propagation time introduces spurious oscillations in the Fourier spectrum. To remove this, a time-dependent damping function $g(t)$ must be multiplied to the autocorrelation function which ensures that the integrand goes smoothly to zero at the end of propagation. We choose the time-dependent damping function

$$g(t) = \cos\left(\frac{\pi t}{2T}\right)\Theta\left(1-\frac{|t|}{T}\right); \tag{2.49}$$

where T is the total propagation time and Θ is the Heaviside step function. In order to compare the simulated spectrum with the experimental one, it may also be necessary to multiply the autocorrelation function with an additional exponential damping factor

$$f(t) = \exp(-t/\tau) \tag{2.50}$$

where τ is a time constant describing a phenomenological broadening of the spectrum due to finite experimental resolution which is equivalent to convoluting the spectrum with a Lorentzian function of full width at half-maximum (FWHM) of Γ[eV] $\sim 1.31/\tau$[fs]. Hence, using the Hermitian property of $C(t)$, in practice, one solves the integral

$$P(\omega) \propto \mathrm{Re} \int_0^T g(t)f(t)C(t)e^{i\omega t}dt. \tag{2.51}$$

The other quantities of interest are the time-dependent populations of the electronic states [70]. As the wave packet propagation is performed in diabatic representation, it is quite straightforward to calculate the diabatic populations. The population of the diabatic electronic state $|\alpha\rangle$ at time t, denotes as $P_\alpha^{(d)}(t)$, is given by

$$P_\alpha^{(d)}(t) = \langle \Psi(\boldsymbol{Q},t)||\alpha\rangle\langle\alpha||\Psi(\boldsymbol{Q},t)\rangle. \tag{2.52}$$

The time-dependent population of the ith adiabatic state, $|i\rangle$, is given by

$$P_i^{(a)}(t) = \langle \Psi(\boldsymbol{Q},t)||i\rangle\langle i||\Psi(\boldsymbol{Q},t). \tag{2.53}$$

The calculation of adiabatic populations is computationally demanding as they need either the transformation of the electronic wave function (diabatic to adiabatic) for every grid point and for each time step or a matrix representation of the projection operator in the adiabatic basis [71]. The form of the projection operator for the adiabatic state $|\alpha\rangle$ is [72]

$$\hat{P}_\alpha^{(a)} = \sum_{\beta,\gamma} |\beta\rangle \mathcal{U}^\dagger_{\beta\alpha}\mathcal{U}_{\alpha\gamma}\langle\gamma|, \tag{2.54}$$

where, $\mathcal{U}_{\alpha\gamma}$ is an elements of the coordinate-dependent adiabatic-to-diabatic transformation matrix.

2.4.2 Non-adiabatic dynamics with the Chebyshev wave-packet propagation method

For a time-independent Hamiltonian, the analytic solution of TDSE reads

$$|\Psi(x,t)\rangle = e^{-iHt/\hbar}|\Psi(x,0)\rangle = \mathcal{U}(0,t)|\Psi(x,0)\rangle. \tag{2.55}$$

In Eq. (2.55) $\mathcal{U}(t)$ is the unitary time-evolution operator.

Historically, $\mathcal{U}(t)$ used to be expanded in a Taylor series, which had serious drawbacks of numerical instability due to lack of conservation of unitarity. The well-known second-order differentiating (SOD) approximation

[73] and fourth-order differentiating (FOD) scheme of Manthe and Köppel [74] overcame this difficulty and conserved the norm and the energy, however, SOD suffered from lack of accuracy for long-time propagations due to the error accumulation in the phase. Tal-Ezer and Kosloff have shown that these problems could be solved by expanding the time-evolution operator in Chebyshev polynomials [75]

$$e^{-iHt/\hbar} \approx \sum_{n=0}^{N} a_n Q_n(-iHt/\hbar) \tag{2.56}$$

where a_n are the expansion coefficients and Q_n are the complex Chebyshev polynomials. The exponential time-evolution, when expressed as a Chebyshev series expansion, takes the form

$$e^{-iHt/\hbar} = e^{-i(\Delta E/2+V_{min})t/\hbar} \sum_{n=0}^{N} (2-\delta_{n0}) J_n \left(\frac{\Delta E t}{2\hbar}\right) Q_n(-iH_s) \tag{2.57}$$

where J_n is the nth order Bessel function of the first kind, Q_n obey recursion relation

$$Q_{n+1} = -2iH_s Q_n + Q_{n+1} \tag{2.58}$$

and H_s is the shifted and scaled Hamiltonian

$$H_s = \frac{H - (\frac{\Delta E}{2} + V_{min})}{\frac{\Delta E}{2}}. \tag{2.59}$$

In the definition of H_s, $V_{min} \leq E_{min}$ (the lowest eigenvalue of $\mathcal{H}$) and $\Delta E = E_{max} - E_{min}$, E_{max} being the largest eigenvalue of $\mathcal{H}$. The shifting is required to make the mapping single valued and the eigenvalues to be monotonically increasing [76]. The scaling makes the eigenvalues of H_s to lie in the interval [-1,+1] which is a necessary requirement for the argument of the Chebyshev polynomials.

One particular simplification for the time-propagation of the wave packet has been achieved by the real wave packet method of Gray *et al* [77, 78]. Consideration of a simultaneous forward and backward propagation in time leads to an iterative equation which is completely equivalent to the TDSE :

$$|\Psi(x,t)\rangle = 2\cos(Ht/\hbar)|\Psi(x,0)\rangle - |\Psi(x,-t)\rangle. \tag{2.60}$$

The above relation makes it possible, for a real and symmetric Hamiltonian and for a real initial wave packet, to perform the entire propagation in the real number space which leads to a saving of computation time and memory.

However, the operation of the cosine of $\mathcal{H}$ on the wave packet is still difficult to perform. A suitable modification of the time-dependent Schrödinger equation by a proper functional mapping simplifies the equation of propagation. In particular, a $\cos^{-1}$ functional mapping, originally introduced by Chen and Guo [79], has been adapted here

$$H_s \mapsto -\frac{\hbar}{\tau}\cos^{-1}(H_s). \tag{2.61}$$

The use of this mapping leads to a modified TDSE

$$i\hbar\frac{\partial}{\partial t}|\Psi_f(x,t)\rangle = f(H_s)|\Psi_f(x,t)\rangle \tag{2.62}$$

However, the time-independent properties remain intact as H and $f(H)$ share the same set of eigenstates under the mapping f which is reflected in the corresponding mapped TISE

$$f(H_s)|\psi_i(x)\rangle = f(E_i^s)|\psi_i(x)\rangle, \tag{2.63}$$

where the eigenvalues $f(E_i^s)$ are related to the eigenvalues of H_s through the relation

$$f(E_i^s) = -\frac{\hbar}{\tau}\cos^{-1}(E_i^s). \tag{2.64}$$

As f is a one-to-one mapping, it is straight forward to retrieve the eigenvalues of the original Hamiltonian whenever required.

Under this mapping, after proper discretization of time $t = n\tau$, the time-evolution (cosine) operator is equivalent to the definition of the series of Chebyshev polynomials

$$\cos\left(\frac{H_s t}{\hbar}\right) \mapsto \cos(n\cos^{-1}(H_s)) = T_n(H_s). \tag{2.65}$$

By the virtue of the above results, time evolution of the wave packet reduces to

$$\Psi_n = T_n(H_s)|\Psi_0\rangle. \tag{2.66}$$

The wave packet can now be propagated by using the recursion relation of the Chebyshev polynomials, which reads

$$\Psi_n = 2H_s\Psi_{n-1} - \Psi_{n-2}, \qquad n \in \mathbb{N}|n > 1. \tag{2.67}$$

Therefore, the iterative propagation of the wave packet involves only matrix-vector multiplications of the Hamiltonian matrix $\boldsymbol{H_s}$ with the vector $\boldsymbol{\Psi_n}$.

In every iteration, the autocorrelation function was calculated using the relations

$$\begin{aligned} C_{2n} &= \langle \Psi(0)|T_{2n}(\boldsymbol{H_s})|\Psi(0)\rangle = \langle \Psi_n|\Psi_n\rangle - C_0 \\ C_{2n+1} &= 2\langle \Psi_{n+1}|\Psi_n\rangle - C_1. \end{aligned} \tag{2.68}$$

Performing n iterations thus yields $2n$ points of the Chebyshev autocorrelation function.

The time-dependent autocorrelation function can be calculated from C_n by

$$C(t) = e^{-i\frac{\bar{H}}{2}t} \sum_{n=1}^{N} (2-\delta_{no})(-i)^n J_n\left(\frac{\bar{H}t}{2}\right) C_n, \tag{2.69}$$

where $\bar{H} = (E_{min} + E_{max})/2$. While it is possible, in principle, to obtain the spectrum from the Fourier transform of the autocorrelation function $C(t)$, a numerical conversion has been used for practical purposes which directly gives the spectral distribution from the Chebyshev autocorrelation function

$$\sigma(E) \propto \sum_{n=1}^{N} (2-\delta_{n0}) \frac{\cos(n\phi)}{\sin(\phi)} C_n, \tag{2.70}$$

where

$$\phi = \arccos\left(\frac{E-\bar{H}}{\Delta E/2}\right). \tag{2.71}$$

2.4.3 The Multiconfiguration time-dependent Hartree method

Despite the high numerical accuracy and simplicity for the implementation, the straightforward numerical solution of the TDSE, which may be called the *standard method*, suffers from an exponential scaling of the computational effort with the number of degrees of freedoms (DOFs). An alternative to the standard method is the *time-dependent Hartree* (TDH) method which expresses the wave function as a Hartree product of time-dependent *single-particle-functions* (SPFs) or orbitals and the time-dependent expansion coefficients are determined by variationally solving the TDSE using the *Dirac-Frenkel variational principle* [80, 81]

$$\langle \delta\Psi | H - i\frac{\partial}{\partial t} | \Psi \rangle = 0. \tag{2.72}$$

Being a single-reference method, TDH often performs rather poorly and misses a large part of the correlation between different DOFs [82]. The

Multiconfiguration time-dependent Hartree (MCTDH) method has been developed as a trade-off between the accuracy of the numerically exact method and the efficiency of the TDH method [83–85]. The flexibility in the number of DOFs and in choosing the number of SPFs allows MCTDH to cover a full range of approximations between TDH (single reference) to numerically exact (analogous to the full CI treatment in electronic structure theory). Importantly, due the variational character, small sets of SPFs are usually sufficient in many cases to yield good results which makes the MCTDH method appealing especially when the number of DOFs is large.

The MCTDH wave function is defined by the following *ansatz* [83–85]

$$\Psi(\boldsymbol{Q},t) = \sum_{j_1=1}^{n_1} \cdots \sum_{j_f=1}^{n_f} A_{j_1 \cdots j_f}(t) \prod_{k=1}^{f} \varphi_{j_k}^{(k)}(Q_k,t) \tag{2.73}$$

$$= \sum_{J} A_J \Phi_J \tag{2.74}$$

where f denotes the number of degrees of freedom, $\boldsymbol{Q}$ is the vector containing the set of nuclear coordinates, the $A_{j_1 \cdots j_f}$ denote the MCTDH expansion coefficients, and the $\varphi_{j_k}^{(k)}$ are the n_k time-dependent expansion functions (SPFs) for each DOF k. Φ_J is the f-dimensional Hartree product of the SPFs represented by the composite index $J = (j_1, \cdots, j_f)$. For practical purposes, the SPFs have to be represented in terms of an underlying time-independent primitive basis set

$$\varphi_{j_k}^{(k)}(Q_k,t) = \sum_{l=1}^{N_k} c_{l j_k}^{(k)}(t) \chi_l^{(k)}(Q_k). \tag{2.75}$$

The primitive basis functions are often replaced by a *discrete variable representation* (DVR) grid. MCTDH is of advantage in comparison to the numerically exact method only if $n_k < N_k (k = 1, \cdots, f)$. The MCTDH equations of motion (EOM) can be derived by applying Dirac-Frenkel variational principle to Eq. (2.73). After some algebra, one obtains two coupled differential equations for the SPFs and the expansion coefficients

$$i\dot{A}_J = \sum_L \langle \Phi_J | H | \Phi_L \rangle A_L, \tag{2.76}$$

$$i\dot{\varphi}_j^{(k)} = \sum_{l,m} \left(1 - P^{(k)}\right) \left(\rho^{(k)^{-1}}\right)_{jl} \langle \boldsymbol{H} \rangle_{lm}^{(k)} \varphi_m^{(k)} \tag{2.77}$$

where

$$P^{(k)} = \sum_{j=1}^{n_k} |\varphi_j^{(k)}\rangle\langle\varphi_j^{(k)}| \tag{2.78}$$

denotes the projection operator on the space spanned by the SPFs for the kth DOF, and

$$\rho_{jl}^{(k)} = \langle \Phi_j^{(k)} | \Psi_l^{(k)} \rangle \tag{2.79}$$

denotes a density matrix and

$$\langle \boldsymbol{H} \rangle_{jl}^{(k)} = \langle \Phi_j^{(k)} | H | \Psi_l^{(k)} \rangle \tag{2.80}$$

is a matrix of mean-fields. Here

$$\Psi_l^{(k)} = \langle \varphi_l^{(k)} | \Psi \rangle_k \tag{2.81}$$

represents a so-called *single-hole function*.

To solve the MCTDH EOM, one requires the evaluations of the Hamiltonian matrix $\langle \Phi_J | H | \Phi_L \rangle$ and the mean-fields $\langle \boldsymbol{H} \rangle$ at each time step. If these integrals are done by multi-dimensional quadrature over the primitive grid, then the performance of the MCTDH method would not be significantly better than the standard one. This problem of multi-dimensional integrals can be circumvented if the Hamiltonian can be written as a sum of products of single particle operators [72]

$$H = \sum_{r=1}^{s} c_r \prod_{k=1}^{f} h_r^{(k)}. \tag{2.82}$$

The sum-of-products structure of the Hamiltonian, which is also known as the "MCTDH form", enables one to evaluate the Hamiltonian matrix elements and the mean-fields only by the one-dimensional integrals. While PE operators are generally not of this special form, fortunately, vibronic coupling models fall within the exceptions and this makes MCTDH well adapeted for solving vibronic dynamics. Despite the above simplifications, the evaluation of the mean fields is still the most computationally expensive part of MCTDH. To reduce the effort, the mean fields are kept constant for some time during the calculation, that is they are not evaluated at every time step of the integrator but at larger so-called *update* time steps. The use of this *constant mean field* (CMF) integration scheme has been shown to speed up the calculation typically by a factor of 10. In comparison with the N^f numbers required to describe the standard wave packet, the memory requirement of the MCTDH wave function becomes

$$\text{memory} \sim n^f + fnN, \tag{2.83}$$

which leads to huge saving in memory when the dimensionality of the problem is high [72].

Vibronic coupling systems are characterized by the motion of the nuclei on multiple coupled PE surfaces and the MCTDH *ansatz* needs to be extended to deal with more than one electronic states. A particularly convenient way is to use the so-called *multi-set* formulation which employs different sets of SPFs for different electronic states. The multi-set formulation is almost always the method of choice for the vibronically coupled systems as the motion of the nuclei on the different electronic states can be very different. In this formulation, the wave function of the system is expanded in the set $\{|\alpha\rangle\}$ of diabatic electronic states [86]

$$\Psi(\boldsymbol{Q},t) = \sum_{\alpha=1}^{\sigma} \Psi^{(\alpha)}(\boldsymbol{Q},t)|\alpha\rangle, \tag{2.84}$$

where the component $\Psi^{(\alpha)}$ is the nuclear wave packet for the electronic state $|\alpha\rangle$ and is represented in the usual MCTDH form as in Eq. (2.73).

In the multi-set formalism, the diabatic population (see Eq. (2.52)) of the state $|\alpha\rangle$ is simply given by the norm of the component of the wave function for state $|\alpha\rangle$

$$P_{\alpha}^{(d)} = ||\Psi^{(\alpha)}||^2. \tag{2.85}$$

Chapter 3

Construction of high-order Jahn-Teller Hamiltonians

In the "standard model" of JT theory, which is described in numerous reviews, monographs and edited volumes on the JT effect [11–18], the Hamiltonian is expanded up to second order in normal-mode displacements. While situations had long been encountered, mainly through extensive *ab initio* calculations, where the JT/PJT coupling strengths were too strong to be described by the quadratic coupling model, extensions of the JT Hamiltonian beyond the standard model were considered only occasionally and for specific systems. For example, the third-order and fourth-order terms in the $E \times e$ Hamiltonian for trigonal systems have been included in some investigations of static and dynamic JT effects in clusters and solids [87–90]. The systematic expansion of the $E \times e$ JT Hamiltonian for trigonal systems up to sixth order has first been given by Viel and Eisfeld [22]. It was discovered by *ab initio* calculations that "intramolecular collisions" of the ligand atoms at large amplitudes of the JT-active bending mode result in a pronounced positive anharmonicity of the *ab initio* bending potentials, which requires a JT expansion up to at least sixth-order in the bending mode [91, 92]. Opalka and Domcke have shown recently that with the help of invariant theory of homogeneous polynomials, it is straightforward to obtain the arbitrarily high-order expansions of JT Hamiltonians [24, 25]. Three generic problems, $E \times e$, $T_2 \times t_2$ and $(A + E) \times (a + e)$ JT/PJT effects, are discussed below.

3.1 The $E \times e$ Jahn-Teller effect

Molecules of C_{3v} symmetry possess degenerate electronic states of E symmetry and degenerate vibrational modes of e symmetry, which transform like

x, y in the C_{3v} point group. The polynomial invariants of the E representation in C_{3v} form a ring and are finitely generated by two polynomials of degree 2 and 3 respectively, which form the so-called generating set of the invariant ring. These are [58, 59]

$$\begin{aligned} f_1 &= x^2 + y^2 \\ f_2 &= x^3 - 3xy^2. \end{aligned} \tag{3.1}$$

All the elements of the ring $\mathbb{R}[x, y]^{C_{3v}}$ can be constructed in terms of these generators

$$\mathbb{R}[x, y]^{C_{3v}} = \mathbb{R}[f_1, f_2]. \tag{3.2}$$

The ring of the C_{3v}-invariant polynomials in the direct sum of two vector spaces of E symmetry (electrons) and e symmetry (nuclei), $\mathbb{R}[V^E \oplus V^e]^{C_{3v}}$ can be computed from $\mathbb{R}[V^e]^{C_{3v}} = \mathbb{R}[f_1, f_2]$ by Weyl's polarization method [67]. After eliminating the redundant terms, it is straightforward to represent the $E \times e$ JT expansion of any order as a sum of the trace and a traceless matrix [22]

$$\mathcal{H}_{es}^{(n)}[E \times e] = \begin{pmatrix} \mathcal{V}^{(n)} & 0 \\ 0 & \mathcal{V}^{(n)} \end{pmatrix} + \begin{pmatrix} \mathcal{W}^{(n)} & \mathcal{Z}^{(n)} \\ \mathcal{Z}^{(n)} & -\mathcal{W}^{(n)} \end{pmatrix}. \tag{3.3}$$

The well-known first-order and second-order JT Hamiltonians are the Hessians of f_2 and f_1^2 respectively.

The expansion of the $E \times e$ JT Hamiltonian up to sixth order is given by

$$\begin{aligned} \mathcal{V}^{(1)} &= 0 \\ \mathcal{V}^{(2)} &= a_1^{(2)}(x^2 + y^2) \\ \mathcal{V}^{(3)} &= a_1^{(3)}(x^3 - 3xy^2) \\ \mathcal{V}^{(4)} &= a_1^{(4)}(x^4 + 2x^2y^2 + y^4) \\ \mathcal{V}^{(5)} &= a_1^{(5)}(x^5 - 2x^3y^2 - 3xy^4) \\ \mathcal{V}^{(6)} &= a_1^{(6)}(x^6 + 3x^4y^2 + 3x^2y^4 + y^6) + a_2^{(6)}(x^6 - 6x^4y^2 + 9x^2y^4) \end{aligned} \tag{3.4}$$

$$\begin{aligned} \mathcal{W}^{(1)} &= \lambda_1^{(1)}x \\ \mathcal{W}^{(2)} &= \lambda_1^{(2)}(x^2 - y^2) \\ \mathcal{W}^{(3)} &= \lambda_1^{(3)}(x^3 + xy^2) \\ \mathcal{W}^{(4)} &= \lambda_1^{(4)}(x^4 - y^4) + \lambda_2^{(4)}(x^4 - 6x^2y^2 + y^4) \\ \mathcal{W}^{(5)} &= \lambda_1^{(5)}(x^5 + 2x^3y^2 + xy^4) + \lambda_2^{(5)}(x^5 - 4x^3y^2 + 3xy^4) \\ \mathcal{W}^{(6)} &= \lambda_1^{(6)}(x^6 + x^4y^2 - x^2y^4 - y^6) + \lambda_2^{(6)}(x^6 - 5x^4y^2 - 5x^2y^4 + y^6) \end{aligned} \tag{3.5}$$

$$
\begin{aligned}
\mathcal{Z}^{(1)} &= \lambda_1^{(1)} y \\
\mathcal{Z}^{(2)} &= \lambda_1^{(2)} (-2xy) \\
\mathcal{Z}^{(3)} &= \lambda_1^{(3)} (x^2 y + y^3) \\
\mathcal{Z}^{(4)} &= \lambda_1^{(4)} (-2x^3 y - 2xy^3) + \lambda_2^{(4)} (4x^3 y - 4xy^3) \\
\mathcal{Z}^{(5)} &= \lambda_1^{(5)} (x^4 y + 2x^2 y^3 + y^5) + \lambda_2^{(5)} (-2x^4 y + 6x^2 y^3) \\
\mathcal{Z}^{(6)} &= \lambda_1^{(6)} (-2x^5 y - 4x^3 y^3 - 2xy^5) + \lambda_2^{(6)} (4x^5 y - 4xy^5)
\end{aligned}
\tag{3.6}
$$

where $\mathcal{V}^{(n)}$ is the nth order of the trace and $\mathcal{W}^{(n)}$ and $\mathcal{Z}^{(n)}$ are the nth order diagonal and off-diagonal elements, respectively, of the traceless JT Hamiltonian. It should be emphasized here that, though this expansion is achieved with the consideration of C_{3v} reference geometry, this is the most general expansion of the $E \times e$ JT effect in trigonal, tetrahedral and cubic symmetries and can be applied to any system in these symmetries without any alteration. This result is a consequence of the presence of redundancies in the irreducible representations of molecular point groups. The polynomial expansions presented here differ, at the first look, from those of Viel and Eisfeld [22]. However, they are inter-convertible by taking linear combinations.

As an illustration, the number of free parameters to be optimized for an 8th order expansion is given in tabular form in Table 3.1. Note that the number of independent optimization parameters grows very slowly with the order of the expansion, which reflects the high inherent symmetry of the $E \times e$ JT Hamiltonian. As an example, the sixth order $E \times e$ JT Hamiltonian

order	1	2	3	4	5	6	7	8
parameters $\mathcal{W}, \mathcal{Z}$	1	1	1	2	2	2	3	3
parameters $\mathcal{V}$	0	1	1	1	1	2	1	2
total	1	2	2	3	3	4	4	5

Table 3.1: Number of parameters in the trace and the diagonal and off-diagonal terms in the $E \times e$ JT expansion in each order.

matrix is given explicitly in Eq. (3.7). It can be seen that the sixth-order JT

Hamiltonian contains only 4 independent optimization parameters.

$$\mathcal{H}^{(6)} = [a_1^{(6)}(x^6 + 3x^4y^2 + 3x^2y^4 + y^6) + a_2^{(6)}(x^6 - 6x^4y^2 + 9x^2y^4)]\,\mathbf{1}$$

$$+ \begin{pmatrix} \lambda_1^{(6)}(x^6 + x^4y^2 - x^2y^4 - y^6) & \lambda_1^{(6)}(-2x^5y - 4x^3y^3 - 2xy^5) \\ +\lambda_2^{(6)}(x^6 - 5x^4y^2 - 5x^2y^4 + y^6) & +\lambda_2^{(6)}(4x^5y - 4xy^5) \\ \\ \lambda_1^{(6)}(-2x^5y - 4x^3y^3 - 2xy^5) & -\lambda_1^{(6)}(x^6 + x^4y^2 - x^2y^4 - y^6) \\ +\lambda_2^{(6)}(4x^5y - 4xy^5) & -\lambda_2^{(6)}(x^6 - 5x^4y^2 - 5x^2y^4 + y^6) \end{pmatrix}. \tag{3.7}$$

3.2 The $T_2 \times t_2$ Jahn-Teller Effect

A general symmetry-adapted polynomial expansion of electrostatic $T \times t$ and $T \times e$ JT Hamiltonians in tetrahedral systems has been developed by Opalka and Domcke [24, 25]. Combining JT theory with the theory of invariant polynomials [61], symmetry-adapted polynomials up to high orders were obtained and a combinatorial scheme was developed to express terms of arbitrary order as products of a small number of invariant polynomials.

The three-sheeted $T_2 \times t_2$ PE surface is represented by three diabatic electronic states of T_2 symmetry, denoted conveniently as x, y, z. The nuclear coordinates of t_2 symmetry are also denoted by x, y, z to reveal the high inherent symmetry of the $T_2 \times t_2$ JT Hamiltonian. The ring of invariant polynomials of the t_2 representation in T_d is finitely generated by a set of three polynomials of degree 2, 3 and 4 in the coordinates x, y, z [24, 59]

$$\begin{aligned} f_1 &= x^2 + y^2 + z^2 \\ f_2 &= xyz \\ f_3 &= x^4 + y^4 + z^4. \end{aligned} \tag{3.8}$$

Any member of the ring $\mathbb{R}[x, y, z]^{T_d}$ can be represented in terms of these generating polynomials, that is

$$\mathbb{R}[x, y, z]^{T_d} = \mathbb{R}[f_1, f_2, f_3]. \tag{3.9}$$

The JT vibronic matrix is given by the doubly polarized invariant polynomials in the combined vector spaces of the electronic coefficients and the nuclear coordinates, which transform identically under the group $T_d \simeq S_4$. Any term of the Hamiltonian matrix expansion is just the Hessian of an invariant polynomial of the ring $\mathbb{R}[x, y, z]^{T_d}$ up to multiplication with a constant factor.

An elegant combinatorial scheme has been developed to represent the $T_2 \times t_2$ JT PE matrix in terms of the generating polynomials in Ref. [24]. The JT vibronic matrix has the highly symmetric structure

$$\mathcal{H}_{el} = \begin{pmatrix} \mathcal{W}(x,y,z) & \mathcal{Z}(z,x,y) & \mathcal{Z}(y,x,z) \\ \mathcal{Z}(z,x,y) & \mathcal{W}(y,x,z) & \mathcal{Z}(x,y,z) \\ \mathcal{Z}(y,x,z) & \mathcal{Z}(x,y,z) & \mathcal{W}(z,x,y) \end{pmatrix} \tag{3.10}$$

where $\mathcal{W}$ and $\mathcal{Z}$ are the diagonal and off-diagonal elements of the JT matrix, respectively. Their expansion up to sixth order reads

$$\begin{aligned}
\mathcal{W}^{(1)}(x,y,z) &= 0 \\
\mathcal{W}^{(2)}(x,y,z) &= a_1^{(2)}x^2 + a_2^{(2)}(y^2+z^2) \\
\mathcal{W}^{(3)}(x,y,z) &= a_1^{(3)}xyz \\
\mathcal{W}^{(4)}(x,y,z) &= a_1^{(4)}x^4 + a_2^{(4)}(y^4+z^4) \\
&\quad + a_3^{(4)}(x^2y^2+x^2z^2+y^2z^2) \\
\mathcal{W}^{(5)}(x,y,z) &= a_1^{(5)}x^3yz + a_2^{(5)}(xy^3z+xyz^3) \\
\mathcal{W}^{(6)}(x,y,z) &= a_1^{(6)}(y^6+z^6) + a_2^{(6)}x^6 + a_3^{(6)}(x^4y^2+x^4z^2) \\
&\quad + a_4^{(6)}(x^2y^4+x^2z^4) + a_5^{(6)}(y^4z^2+y^2z^4) + a_6^{(6)}x^2y^2z^2 \\
\mathcal{Z}^{(1)}(x,y,z) &= b_1^{(1)}x \\
\mathcal{Z}^{(2)}(x,y,z) &= b_1^{(2)}yz \\
\mathcal{Z}^{(3)}(x,y,z) &= b_1^{(3)}x^3 + b_2^{(3)}(xy^2+xz^2) \\
\mathcal{Z}^{(4)}(x,y,z) &= b_1^{(4)}x^2yz + b_2^{(4)}(y^3z+yz^3) \\
\mathcal{Z}^{(5)}(x,y,z) &= b_1^{(5)}x^5 + b_2^{(5)}(x^3y^2+x^3z^2) \\
&\quad + b_3^{(5)}(xy^4+xz^4) + b_4^{(5)}(xy^2z^2) \\
\mathcal{Z}^{(6)}(x,y,z) &= b_1^{(6)}y^3z^3 + b_2^{(6)}(y^4z^2+y^2z^4) \\
&\quad + b_3^{(6)}x^4yz + b_4^{(6)}(x^2y^3z+x^2yz^3).
\end{aligned} \tag{3.11}$$

The expansion terms up to 12th order can be found in Ref. [24]. The beauty of this representation is that the elements of the 3×3 JT matrix consist of just two functions, whose position in the matrix is determined by the first argument. There are only two kinds of parameters, $a_i^{(n)}$ and $b_i^{(n)}$ which are to be determined by a least-squares fitting of *ab initio* data. The number of parameters to be optimized for an 8th-order expansion of the $T_2 \times t_2$ PE matrix is summarized in Table 3.2. The 8th order PE matrix, for example, contains 53 parameters.

order	1	2	3	4	5	6	7	8	
parameters $\mathcal{W}$	0	2	1	3	2	6	4	9	
parameters $\mathcal{Z}$	1	1	2	2	4	4	6	6	
total	1	3	3	5	6	10	10	15	=53

Table 3.2: Number of parameters in the diagonal and off-diagonal terms in the $T_2 \times t_2$ JT matrix in each order.

3.3 The $(E+A)\times(e+a)$ Jahn-Teller/pseudo-Jahn-Teller effect in trigonal systems

In trigonal systems, the degenerate electronic state typically arises from configurations with an electron or a hole in $2p_x$, $2p_y$ (or $3p_x$, $3p_y$) orbitals. The corresponding $2p_z$ (or $3p_z$) orbital transforms according to the A representation. The ^2E and ^2A states arising from an electron or a hole in the p-shell of a trigonally coordinated atom are often close in energy and can interact in first order via normal modes of e symmetry, which gives rise to the $(^2E+^2A)\times e$ PJT effect. Although many trigonal systems are of C_{3v} symmetry, the description in the D_{3h} point group becomes essential whenever the inversion of pyramidal structures is possible upon excitation or ionization. In the D_{3h} group, the $(E + A) \times (e + a)$ vibronic-coupling problem becomes the $(E' + A_2'') \times (e' + a_2'')$ vibronic-coupling problem.

The JT and PJT effects arising from a partially occupied p-shell are mechanistically not independent. It is therefore generally preferable to consider the vibronic coupling effects within the $^2E'+^2A_2''$ three-state manifold, rather than the vibronic coupling within the isolated ^2E state. Along with the strong JT activity of the e'-type bending vibrational mode, so-called umbrella mode of a_2'' symmetry is usually strongly coupled to electronic transitions in trigonal systems, CH_3O, NH_3^+ and CH_3F^+ being prominent examples [93–95]. The bending mode of e' symmetry and the umbrella mode of a_2'' symmetry therefore form a triplet of strongly vibronically active normal modes. These observations suggest that the $(E' + A_2'') \times (e' + a_2'')$ three-state three-mode vibronic-coupling problem should be considered as the generic JT/PJT problem in trigonal systems.

In tetrahedral and octahedral systems, an electron (or a hole) in a p-shell gives rise to $T_2 \times t_2$ JT effect which has been discussed in the previous section in some details. Again the triply degenerate t_2 bending mode is strongly JT-active. When the symmetry is reduced from tetrahedral or octahedral to trigonal, the T_2 state splits into $E + A$ states and the t_2 normal mode splits into $e + a$ normal modes. The $(E + A) \times (e + a)$ JT/PJT effect in trigonal

systems thus is a reduced-symmetry exemplar of the $T_2 \times t_2$ JT effect in tetrahedral systems. This is another argument why the $(E + A) \times (e + a)$ JT/PJT effect should be considered as the generic vibronic-coupling problem in trigonal systems.

Eisfeld and Viel derived the expansion of the $(E + A) \times e$ PJT Hamiltonian up to sixth order in the JT-active bending mode [23]. Considering the umbrella mode up to second order, this model was applied to construct the PE surfaces of the $(E + A) \times (e + a)$ PJT effect in NH_3^+ [41]. In the present work, we extend the existing description of $(E+A)\times(e+a)$ vibronic coupling by treating the umbrella mode consistently with the JT-active bending mode to all orders, making use of polynomial invariant theory [61].

Let us consider trigonal open-shell four-atomic systems (e.g. CH_3, NH_3^+). The hole in the p-shell of the central atom gives rise to a degenerate electronic state of E' symmetry with wave functions ψ_x, ψ_y and a nondegenerate electronic state ψ_z of A_2'' symmetry in D_{3h}. The ψ_x, ψ_y, ψ_z form a diabatic electronic basis for the $(E' + A_2'') \times (e' + a_2'')$ JT/PJT Hamiltonian. Since large-amplitude motion in the umbrella coordinate may lead to inversion, it is natural to choose the planar conformation (D_{3h} symmetry) as the reference geometry. The umbrella coordinate changes sign at the planar configuration and thus is antisymmetric with respect to the molecular plane of the D_{3h} configuration.

Denoting the symmetry-adapted nuclear coordinates as x, y (e' symmetry) and z (a_2'' symmetry), the JT/PJT matrix in the electronic basis ψ_x, ψ_y, ψ_z is written as

$$\mathcal{H}_{es}(x,y,z) = \begin{pmatrix} \mathcal{H}_{xx}(x,y,z) & \mathcal{H}_{xy}(x,y,z) & \mathcal{H}_{xz}(x,y,z) \\ \mathcal{H}_{yx}(x,y,z) & \mathcal{H}_{yy}(x,y,z) & \mathcal{H}_{yz}(x,y,z) \\ \mathcal{H}_{zx}(x,y,z) & \mathcal{H}_{zy}(x,y,z) & \mathcal{H}_{zz}(x,y,z) \end{pmatrix} \tag{3.12}$$

The eigenvalues of the matrix $\mathcal{H}_{es}(x,y,z)$ are the adiabatic PE surfaces, which we denote as $V_1(x,y,z)$, $V_2(x,y,z)$, $V_3(x,y,z)$.

Following the strategy described in the previous section for the $T_2 \times t_2$ JT Hamiltonian, we expand the matrix elements $\mathcal{H}_{kl}(x,y,z)$, $(k,l = x,y,z)$, in polynomials of the symmetry-adapted nuclear displacement coordinates. The three electronic basis functions as well as the three nuclear coordinates form the basis of the $E \oplus A$ representation of the C_{3v} point group. The invariant polynomials of the $E \oplus A$ representation are generated by [24, 59, 96]

$$f_1 = z^2 \tag{3.13a}$$
$$f_2 = x^2 + y^2 \tag{3.13b}$$
$$f_3 = x^3 - 3xy^2. \tag{3.13c}$$

The polynomials of the invariant ring $\mathbb{R}[x,y,z]^{E\oplus A}$ can be expressed in terms of these generators. Importantly, theorems of Hilbert and Noether provide the proof that the generators of Eq. (3.13) are complete [61]. All symmetry-adapted homogeneous polynomials up to arbitrary order can thus be expressed as linear combinations of products of the three invariants of Eq. (3.13).

The most convenient approach to obtain the expansion of the matrix elements $\mathcal{H}_{kl}(x,y,z)$ in x, y, z is to make use of Weyl's polarization method [67]. The $\mathcal{H}_{kl}(x,y,z)$ can be viewed as polynomials in the electronic variables x, y, z up to second order and as polynomials in the nuclear coordinates x, y, z up to a certain arbitrary order. Weyl's polarization method generates the invariant polynomials in the joint vector spaces of electronic and nuclear variables from the generators given in Eq. (3.13). The expansion of the vibronic matrix (3.12) up to any order n in the nuclear coordinates in found by computing the Hessian (with respect to the electronic variables) of all possible products of the generators of order $(n+2)$. After the elimination of the linearly dependent terms, the $\mathcal{H}_{kl}(x,y,z)$ are obtained as polynomial expansions up to order n [24].

Up to second order, we obtain the well-known $(E+A)\times(e+a)$ JT/PJT Hamiltonian [11, 12, 14, 16–18, 97, 98]

$$\begin{aligned}\mathcal{H}_{es}^{(0-2)}(x,y,z) =& \mathcal{H}_0^{(2)}(x,y,z)\\ &+\begin{pmatrix} E_E + a_1^{(1)}x + a_2^{(2)}(x^2-y^2) & -a_1^{(1)}y + 2a_2^{(2)}xy & c_1^{(2)}xz \\ -a_1^{(1)}y + 2a_2^{(2)}xy & E_E - a_1^{(1)}x - a_2^{(2)}(x^2-y^2) & c_1^{(2)}yz \\ c_1^{(2)}xz & c_1^{(2)}yz & E_A \end{pmatrix}\end{aligned} \tag{3.14a}$$

where

$$\mathcal{H}_0^{(2)}(x,y,z) = \begin{pmatrix} a_1^{(2)}(x^2+y^2) + a_3^{(2)}z^2 & 0 & 0 \\ 0 & a_1^{(2)}(x^2+y^2) + a_3^{(2)}z^2 & 0 \\ 0 & 0 & b_1^{(2)}(x^2+y^2) + b_2^{(2)}z^2 \end{pmatrix} \tag{3.14b}$$

represents the unperturbed part of the PE surface up to second order. The Hamiltonian (3.14) reduces to the standard linear-plus-quadratic $E\times e$ JT Hamiltonian if the electronic state ψ_z and the umbrella coordinate z are ignored. $a_1^{(1)}$ and $a_2^{(2)}$ are the linear and quadratic JT coupling constants, respectively. Note that the $E-A$ PJT coupling, given by the parameter $c_1^{(2)}$, vanishes for $z=0$ (D_{3h} symmetry). The $E-A$ PJT coupling is thus a bilinear coupling term when the D_{3h} reference geometry is chosen. For a C_{3v}

reference geometry, where $z = z_0 \neq 0$, the $E - A$ PJT coupling is linear in the coordinates x, y of e symmetry.

The expansion of $\mathcal{H}_{kl}(x, y, z)$ up to arbitrary order can be readily generated. The matrix elements $\mathcal{H}_{kl}^{(n)}(x, y, z)$ for $n = 3-8$ are given in Appendix 2. It can be seen the PJT coupling elements $\mathcal{H}_{xz}(x, y, z)$ and $\mathcal{H}_{yz}(x, y, z)$ vanish for $z = 0$ in all orders. The expansion of $\mathcal{H}_{kl}(x, y, z)$ up to n-th order in all three coordinates x, y, z generalizes the JT/PJT Hamiltonian of Eisfeld and Viel [23], in which the umbrella mode was consistently included up to second order only.

The number of independent parameters $a_i^{(n)}$, $b_i^{(n)}$, $c_i^{(n)}$ of the $(E + A) \times (e + a)$ vibronic matrix in each order n, which are fitting parameters to be determined by a least-squares fit of the eigenvalues of the vibronic matrix to *ab initio* adiabatic PE data, is given in Table 3.3 up to 8th order and it is instructive to compare it with the corresponding number of independent parameters for the $T_2 \times t_2$ vibronic matrix in T_d symmetry given in the previous section (see Table 3.2). While the $(E + A) \times (e + a)$ Hamiltonian has more independent parameters than the $T_2 \times t_2$ JT Hamiltonian due to the reduced symmetry, the number of parameters is much lower than for a Taylor expansion of the corresponding order.

order	0	1	2	3	4	5	6	7	8	
Parameters $\mathcal{H}_{11}$, $\mathcal{H}_{22}$, $\mathcal{H}_{12}$	1	1	3	3	6	6	11	10	17	
Parameters $\mathcal{H}_{33}$, $\mathcal{H}_{13}$, $\mathcal{H}_{23}$	1	0	3	2	5	5	9	6	14	
Total	2	1	6	5	11	11	20	16	31	=103

Table 3.3: Number of parameters in the diagonal and off-diagonal elements in the $(A_2'' + E') \times (a_2'' + e')$ PE matrix in each order.

Chapter 4

Application to P_4^+

The $E \times e$ JT effect is the most well-studied JT problem and a wide range of the literature has documented the exploration of different aspects of it [12, 14, 16–18]. While the JT Hamiltonian matrix is expanded up to second order in normal-mode displacements in the standard model of the JT effect [12, 14, 16–18], the inclusion of JT coupling terms beyond second order has been suggested only in recent years [22, 87–89] and a few applications to a series of JT-active systems have been reported [41, 91, 92, 99, 100]. The particularly strong $E \times e$ JT effect in the electronic ground state of the P_4^+ cation is the subject of study of the present work. Our goal is to explore the relevance of JT coupling terms beyond second order for the dynamical $E \times e$ JT effect in P_4^+.

The ground electronic state of the tetrahedral P_4 cluster is of $^1A_1$ symmetry. The ejection of an electron from the highest-occupied $1e$ molecular orbital (MO) of P_4 creates the doubly degenerate (^2E) ground state in the P_4^+ cation. Due to the JT effect, the P_4^+ cation is unstable with respect to distortions along the doubly degenerate vibrational mode of e symmetry. The large value of the dimensionless linear $^2E \times e$ JT coupling parameter of P_4^+ reported by several theoretical and experimental studies (> 5.0) indicates the existence of one of the strongest JT couplings in nature [101–103].

Several recordings of the photoelectron spectrum of P_4 have been reported [101, 104–106]. The photoelectron spectrum recorded by Wang *et al.* exhibits the highest resolution [101]. The clear double-hump structure of the first band of the photoelectron spectrum indicates the presence of a very strong $^2E \times e$ JT coupling within the ^2E state. The overlap of the first two bands in the experimental spectrum indicates, in addition, the possibility of pseudo-JT (PJT) coupling of the ^2E ground state and the $^2T_2$ first excited state through the vibrational mode of t_2 symmetry. Meiswinkel and Köppel investigated the $(E + T_2) \times (e + t_2)$ JT/PJT effect in P_4^+ employing

the linear vibronic coupling model and demonstrated the effect of the PJT coupling on the vibronic structure of the $^2T_2$ band [102]. While the ^2E–$^2T_2$ PJT coupling may affect the vibronic spectrum of the ^2E state, its effects are weak compared with the very strong $E \times e$ JT coupling in the ^2E state. The objective of the present work is to construct an *ab initio* two-sheeted two-dimensional $^2E \times e$ JT potential-energy (PE) surface for P_4^+ which accounts for the strong anharmonicity at large displacements of the JT-active e mode. As is well-known, spin-orbit (SO) coupling is quenched in ^2E states in tetrahedral systems [12] and therefore does not need to be considered here.

4.1 Symmetry-adapted coordinates

The six internuclear distances of a tetrahedral X_4 system form a basis of a six-dimensional reducible representation (Γ) of the group T_d, which reduces to three irreducible representations

$$\Gamma = A_1 \oplus E \oplus T_2. \tag{4.1}$$

The symmetry-adapted linear combinations (SALCs) of atom-atom distances which transform according to the E representation are well-known and are

$$\begin{aligned} s_a &= \frac{1}{2\sqrt{3}}(2\Delta r_{12} + 2\Delta r_{43} - \Delta r_{13} - \Delta r_{24} - \Delta r_{14} - \Delta r_{23}) \\ s_b &= \frac{1}{2}(\Delta r_{13} + \Delta r_{24} - \Delta r_{14} - \Delta r_{23}) \end{aligned} \tag{4.2}$$

where the Δr_{ij} are displacements of the internuclear distances.

The position vectors of the four nuclei in 3D space are computed from displacements along the internal coordinates of e symmetry through the relation

$$\boldsymbol{r} = \boldsymbol{r}^{(0)} + \boldsymbol{A}\boldsymbol{s}, \tag{4.3}$$

$$\boldsymbol{A} = \begin{pmatrix} \frac{1}{2}(\boldsymbol{r}_{14} - \boldsymbol{r}_{13}) & \frac{1}{2\sqrt{3}}(-2\boldsymbol{r}_{12} + \boldsymbol{r}_{13} + \boldsymbol{r}_{14}) \\ \frac{1}{2}(\boldsymbol{r}_{23} - \boldsymbol{r}_{24}) & \frac{1}{2\sqrt{3}}(2\boldsymbol{r}_{12} + \boldsymbol{r}_{23} + \boldsymbol{r}_{24}) \\ \frac{1}{2}(\boldsymbol{r}_{13} - \boldsymbol{r}_{23}) & \frac{1}{2\sqrt{3}}(-2\boldsymbol{r}_{34} - \boldsymbol{r}_{13} - \boldsymbol{r}_{23}) \\ \frac{1}{2}(\boldsymbol{r}_{24} - \boldsymbol{r}_{14}) & \frac{1}{2\sqrt{3}}(2\boldsymbol{r}_{34} - \boldsymbol{r}_{14} - \boldsymbol{r}_{24}) \end{pmatrix} \tag{4.4a}$$

$$\boldsymbol{s} = \begin{pmatrix} s_a \\ s_b \end{pmatrix} \tag{4.4b}$$

$$\boldsymbol{r}^{(0)\mathrm{T}} = (\boldsymbol{r}_1^{(0)}, \boldsymbol{r}_2^{(0)}, \boldsymbol{r}_3^{(0)}, \boldsymbol{r}_4^{(0)}) \tag{4.4c}$$

$$\boldsymbol{r}^{\mathrm{T}} = (\boldsymbol{r}_1, \boldsymbol{r}_2, \boldsymbol{r}_3, \boldsymbol{r}_4). \tag{4.4d}$$

Here $\boldsymbol{r}^{(0)}$ and $\boldsymbol{r}$ represent the position vectors of the four nuclei at the reference geometry and at the displaced geometry, respectively. The $\boldsymbol{r}_{ij}$ in matrix $\boldsymbol{A}$ are unit vectors in the direction from atom i to atom j, which form the primitive basis of the SALCs. The ith row of matrix $\boldsymbol{A}$ defines the position of nucleus i under unit displacements of the internal coordinates of e symmetry. This formulation of symmetry coordinates is particularly advantageous in the sense that the set of mass-weighted normal modes, which is used in our quantum dynamical calculations, is actually proportional to the symmetry coordinates s_i of corresponding symmetry. From now on, the nuclear coordinates s_a and s_b will be denoted as x and y respectively.

4.2 Electronic-structure calculations and the fitted potential-energy surface

Ab initio electronic structure calculations have been carried out to compute the energies of the ^2E ground electronic state as a function of nuclear displacement coordinates of e symmetry. The state-averaged complete-active-space self-consistent-field (SA-CASSCF) method was employed. The active space consisted of the twelve $3p$ orbitals on the P atoms of P_4^+. The $3s$ and core orbitals were fully optimized, but were constrained to be doubly occupied in all configuration state functions (CSFs). Dunning's correlation-consistent polarised valence double-ζ (cc-pVDZ) basis set has been employed throughout [107]. The five lowest electronic states have been state averaged in the CASSCF optimizations to obtain a balanced description of the wavefunction in the full range of nuclear coordinate space. No symmetry constraints were imposed in the *ab initio* calculations. All electronic-structure calculations were performed with the MOLPRO quantum chemistry package [108].

Energy data points have been calculated at ≈ 1100 geometries which span the two-dimensional nuclear configuration space. The origin of the energy scale is chosen as the energy of the tetrahedral reference geometry of the ^2E ground state of the cation. Data points having energy up to 2.0 eV with respect to the origin have been considered for the fitting procedure. The polynomial expansion coefficients were optimized by fitting the eigenvalues of the diabatic PE matrix to the *ab initio* data. A non-linear least squares optimization scheme based on the Marquardt-Levenberg algorithm has been implemented for this purpose. The fitting procedure has been initialized with the second-order model. A reduced set of data points, $-0.2\,\text{Å} \leq x, y \leq 0.2\,\text{Å}$, has been considered for this purpose. While the second-order fitted surface was in good agreement with the *ab initio* data close to the reference geometry,

it shows large deviations at large-amplitude displacements (see Fig. 4.1).

In order to obtain an accurate PE surface up to 2 eV, the order of the expansion of the JT model potential has been gradually increased with a consistent increase of the range of data points considered in the fitting. The fourth-order fitting has been performed in the interval $-0.5\,\text{Å} \leq x, y \leq 0.5\,\text{Å}$, which reproduced the energy data points quite accurately in the full range of the calculated configuration space. To demonstrate the convergence of the fitting procedure, a sixth-order fitting was finally performed for the same set of *ab initio* data points. While the difference between the fourth-order and the sixth-order surfaces is within drawing accuracy, the inclusion of fifth-order and sixth-order coupling terms improves the agreement with the *ab initio* data for large displacements (e. g. when $x \geq 0.8\,\text{Å}$ in Fig. 1(a)). The rms residuals for the sixth-order fitting are estimated to be ≈ 0.02 eV. The asymmetry in the potential with respect to $x = 0$ in Fig. 1(a) is due to the warping of the lower adiabatic PE surface arising from the contributions of second-order and higher-order coupling terms.

The diagonal elements of the 2nd-order and the 4th-order diabatic PE matrices are compared in figure 4.2. The diabatic off-diagonal elements of the 2nd-order and the 4th-order fitting are compared in figure 4.3. The results of the 6th-order fitting are not shown, as they are marginally different from those of the 4th-order fitting. Figure 2(b) exhibits the pronounced positive anharmonicity of the diagonal elements for large displacements in x and y. Figures 3(a) and 3(b) illustrate the tilting of the diabatic coupling surface, which is a plane in first order, by the higher-order terms.

4.3 Simulation of the ^2E band of the photoelectron spectrum of P_4

The spectral intensity distribution function has been calculated by the Fourier trans form of the time-dependent autocorrelation function. The initial wave packet has been propagated in time under the influence of the time-independent Hamiltonian of the system defined as

$$\mathcal{H} = \mathcal{T} + \mathcal{V}(x, y) = -\frac{1}{2}\left(G_{xx}\frac{\partial^2}{\partial x^2} + G_{yy}\frac{\partial^2}{\partial y^2}\right) + \mathcal{V}(x, y) \qquad (4.5)$$

where $\mathcal{V}(x, y)$ is the diabatic PE matrix defined in Eq. (3.3) and G is the kinematic matrix.

The Hamiltonian and the wave packet have been represented on a direct-product discrete variable representation (DVR) grid [109]. The x coordinate

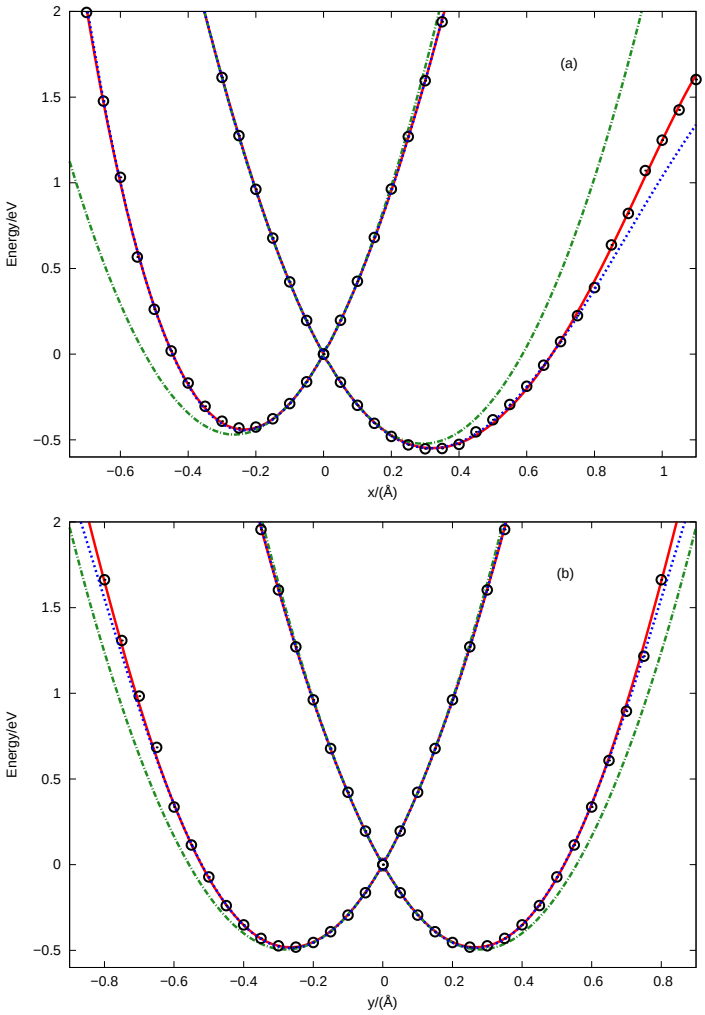

Figure 4.1: (a) Cross sections of the 2nd order (dotted-dashed green line), 4th order (dashed blue line) and the 6th order (full red line) PE surfaces of the ground electronic state of P_4^+ along the nuclear coordinate x, compared with the *ab initio* data (black circles). (b) Cross sections of the 2nd order (dotted-dashed green line), 4th order (dashed blue line) and the 6th order (full red line) PESs of the ground electronic state of P_4^+ along the nuclear coordinate y, compared with the *ab initio* data (black circles).

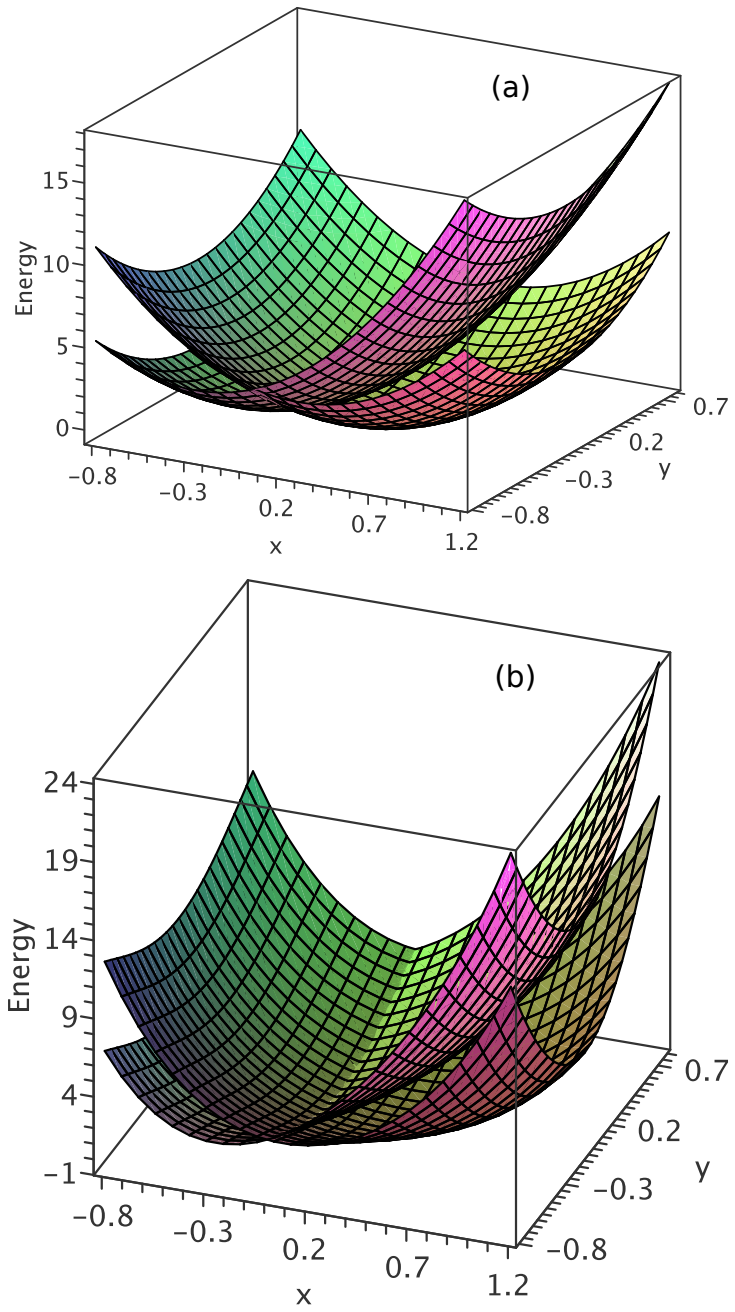

Figure 4.2: Diagonal elements of the diabatic PE matrix of P_4^+ fitted up to 2nd-order (a) and up to 4th-order (b) as functions of x and y. Note the different ordinate scales in (a) and (b).

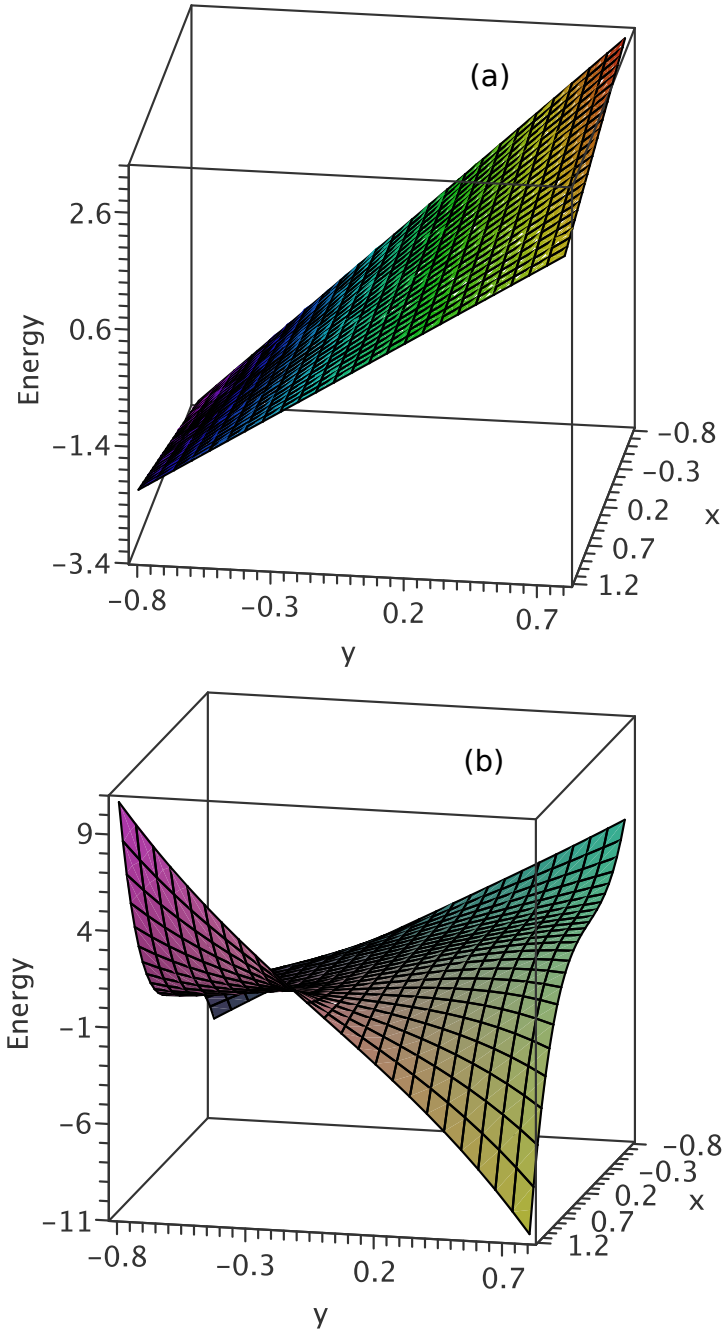

Figure 4.3: Off-diagonal element of the diabatic PE matrix of P_4^+ fitted up to 2nd-order (a) and up to 4th-order (b) as functions of x and y. Note the different ordinate scales in (a) and (b).

has been sampled by 101 equidistant grid points in the range -400.0 au to 500.0 au. The same number of grid points has been employed along the y coordinate in the range -400.0 au to 400.0 au. Whittaker's cardinal (sinc(x)) function has been employed as primitive interpolating basis function. The DVR was constructed in the form of a tensor grid of considered degrees of freedom. In this representation, the kinetic-energy operator has a particularly simple ans sparse structure. The matrix elements of the kinetic-energy operator is given by

$$\mathcal{T}_{j,j+k}^{(i)} = \begin{cases} -\frac{1}{6}\left(\frac{\pi}{\Delta q_i}\right)^2 & k = 0 \\ -\frac{(-1)^k}{(k\Delta q_i)^2} & k \neq 0 \end{cases} \tag{4.6}$$

where q_i is either x or y in this case and Δq_i is the respective grid spacing. A 101×101 matrix is obtained for each degree of freedom. The contraction scheme of Harris, Engerholm and Gwinn (HEG) was used to optimise the equidistant grid along each normal coordinate [110]. Due to the special structure of the matrix $\mathcal{T}$, only the non-zero elements of it are calculated on the fly during the Chebyshev iterations. The PE matrix was constructed as a $(101\times101)\times2(2+1)$ matrix (2 electronic states were taken into account) as the LAPACK packed storage format.

The initial wave packet was prepared in the electronic ground state of P_4, assuming zero vibrational temperature and a harmonic vibrational frequency of 366.1 cm^{-1} (computed from *ab initio* data). The initial wave packet was vertically excited to the ^2E state of the cation and propagated with the Chebyshev method. We computed the vertical ionization energy as 9.55 eV using RCCSD(T) ab initio calculations. The high-resolution spectrum was obtained by convoluting the autocorrelation function with a Gaussian function of 1.17 meV full width at half maximum (FWHM). For the low-resolution spectral envelope, the FWHM has been increased by a factor of 30 (35 meV).

Fig. 4(a) shows the first band of the photoelectron spectrum of P_4 calculated with the quadratic JT model. Compared to the results obtained with the linear JT model, reported by Wang *et al.* [101] and Opalka *et al.* [103], the vibronic line density is increased dramatically and the equidistant structure of the progression in the e mode is lost by the inclusion of the second-order JT coupling terms. This result is in agreement with the calculations of Meiswinkel and Köppel [102]. Wang *et al.* [101] analyzed the influence of increasing dimensionless quadratic JT coupling constant g within the range of 0 to 0.1 along with a fixed dimensionless linear JT coupling constant $k = 5.75$ on the simulated spectra. The spectra presented in this work with *ab initio* calculated $k = 5.1$ and $g = 0.027$ correspond

closely to Fig. 8(f) of Ref. 17, where g was taken to be 0.05. The pronounced double-hump structure of the low-resolution envelope and the narrower second hump, representing a Slonczewski resonance [111], are the signatures of a very strong $E \times e$ JT effect.

The photoelectron spectrum computed with the 6th-order potential is shown in Fig. 4(b). The low-resolution envelope becomes more irregular in comparison with the 2nd-order spectrum. More conspicuously, the high-resolution spectrum shows a significant decrease in the line density. This reduction in the line density is a consequence of the significant positive anharmonicity of the PE surface. For more detailed insight, the onsets of both the spectral envelopes are plotted on an enlarged scale in the insets in Figs. 4(a) and 4(b). It can be seen that the onset of the 6th-order spectrum is ≈ 0.1 eV lower than that of the 2nd-order spectrum, which is a consequence of the fact that the very large JT stabilization energy in the ^2E state of P_4^+ is not accurately recovered by the 2nd-order model. As a consequence of the steeper increase of the 6th-order PE surface with x and y, the intensity distribution of the 6th-order spectrum terminates at lower energy (≈ 10.4 eV) than the 2nd-order spectrum (≈ 10.6 eV).

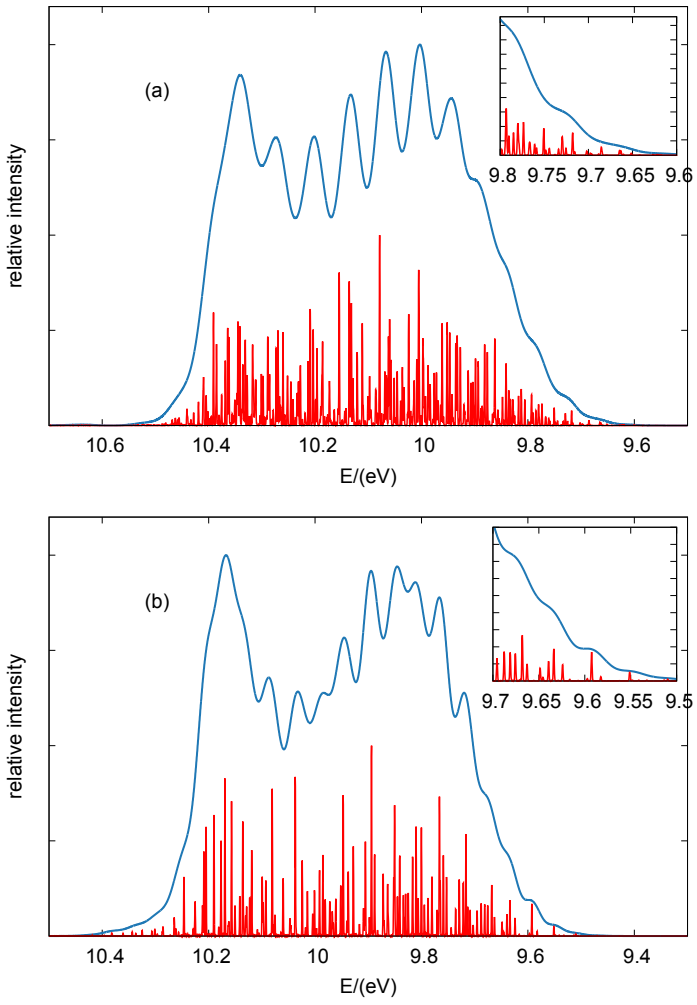

Figure 4.4: $E \times e$ JT spectrum of P_4^+ (red line) obtained with the quadratic JT Hamiltonian (a) and with the 6th-order JT Hamiltonian (b). The blue line represents the corresponding low-resolution spectral envelopes.

Chapter 5

Application to PH_3^+

A unified theoretical description of the potential-energy (PE) surfaces of the ground and the excited electronic states of molecular systems undergoing large distortions upon photo-ionization remains a challenging task. Group-V trihydrides are typical exemplars exhibiting large amplitude vibrational motions owing to the different equilibrium structures in the ground and the excited electronic states of the cation and the molecule. In this work, the complex non-adiabatic dynamics of PH_3^+ has been investigated upon ionization to the ground state and first-excited state of the cation.

The ejection of an electron from the $2e$ molecular orbital (MO) of PH_3 results in the doubly degenerate $^2E'$ excited state of the cation which is subject to strong $^2E' \times e'$ Jahn-Teller (JT) couplings [18] via the two doubly degenerate stretching and bending vibration modes (e'). Moreover, the $^2E'$ excited state interacts with the ground state ($^2A_2''$) state through pseudo-JT (PJT) coupling via the JT-active e' modes. The umbrella mode plays a twofold role: (i) it tunes the energy gap between the $^2E'$ and $^2A_2''$ states and thus induces a CI between them and (ii) it switches on the PJT coupling between the $^2E'$ state and the $^2A_2''$ state in first order in displacements from the planar geometry.

Several recordings of the phototelectron spectrum of PH_3 have been reported in the literature [112–115]. Recently, a rotationally resolved zero-kinetic-energy (ZEKE) photoelectron spectrum of the $^2A_2''$ state has been reported by Mo and coworkers [116]. They have measured, for the first time, the tunneling splittings of the lowest vibrational levels of PH_3^+ in the $\tilde{X}^2A_2''$ state. For this work, we refer to the HeI photoelectron spectrum recorded by Maripuu et. al. [114] as the experimental reference.

5.1 Symmetry-adapted nuclear coordinates and hierarchical expansion of the PE surface

It is well known that proper choice of the nuclear coordinates is as important for the accurate analytic representations of the PE surfaces as it is for the nuclear quantum dynamics. The six vibrational modes of PH_3^+, which comprise of one symmetric stretching mode (a_1'), one symmetric bending mode (a_2'') and two doubly-degenerate stretching and bending modes (e'), have been described by six symmetry-adapted linear combinations (SALCs) of displacements in internal coordinates from the D_{3h} reference geometry as

$$\begin{aligned}
S_1(a_1') &= \frac{1}{\sqrt{3}}(\Delta r_1 + \Delta r_2 + \Delta r_3) \\
S_2(a_2'') &= \Delta\theta \\
S_3(e_x') &= \frac{1}{\sqrt{6}}(2\Delta r_1 - \Delta r_2 - \Delta r_3) \\
S_4(e_y') &= \frac{1}{\sqrt{2}}(\Delta r_2 - \Delta r_3) \\
S_5(e_x') &= \frac{1}{\sqrt{6}}(2\Delta\alpha_1 - \Delta\alpha_2 - \Delta\alpha_3) \\
S_6(e_y') &= \frac{1}{\sqrt{2}}(\Delta\alpha_2 - \Delta\alpha_3).
\end{aligned} \tag{5.1}$$

The Δr_i, $\Delta\alpha_i$ and $\Delta\theta$, in Eq. (5.1), are the displacements in primitive internal coordinates which are illustrated in Fig. 5.1. The hydrogens, in Fig. 5.1 are numbered in an anti-clockwise fashion and their distances from the central P atom is denoted by r_1, r_2 and r_3 respectively. The angles α_1, α_2 and α_3 are defined as the angles between two adjacent P−H bonds projected on a plane parallel to the plane of the molecule at the D_{3h} symmetry and perpendicular to the trisector (black solid vertical line going through P). This definition ensures a correct description of the large amplitude bending motions of PH_3^+. The umbrella coordinate is defined as the displacement in the pyramidalization angle θ with a shift of $\pi/2$. Thus the planar reference geometry ($\theta = \pi/2$) corresponds to a zero displacement in the S_2 coordinate. By construction, all the three P−H bonds make the same angle with the trisector. In this definition, the umbrella coordinate exhibits the correct symmetry property by changing sign with respect to reflection on the molecular plane.

The kinetic-energy and the PE operators are represented in a three dimensional diabatic electronic basis, representing the p_x, p_y and p_z orbitals on the P atom. The elements of the 3×3 PE matrix are expanded in symmetry coordinates as described below.

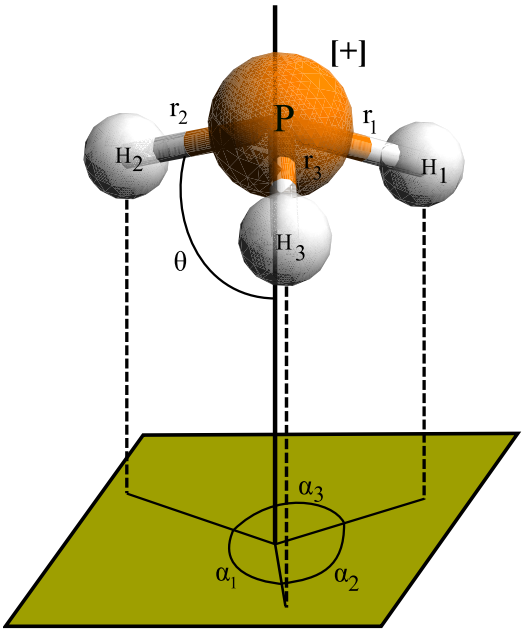

Figure 5.1: Definition of the primitive internal coordinates of PH_3^+ in terms of inter-atomic distances (r_i), projected bond angles (α_i) and the trisector angle θ

The three-state six-mode diabatic PE matrix employed here extends the three-state three-mode $(E+A)\times(e+a)$ JT/PJT PE matrix, developed during this work (see Chapter 2), by the inclusion of the three stretching modes. The six-mode PE matrix is approximated as a hierarchical expansion in terms of lower dimensional potentials as

$$\boldsymbol{V}(\boldsymbol{S}) = \boldsymbol{V}(0) + \boldsymbol{V}(S_1) + \boldsymbol{V}(S_2, S_3, S_4) + \boldsymbol{V}(S_2, S_5, S_6) - \boldsymbol{V}(S_2), \qquad (5.2)$$

where $\boldsymbol{S}$ is the vector containing displacements along the six symmetry coordinates. The matrix $\boldsymbol{V}(0)$ is

$$\boldsymbol{V}(0) = E_A\mathbf{1} + \begin{pmatrix} 0 & 0 & 0 \\ 0 & \Delta & 0 \\ 0 & 0 & \Delta \end{pmatrix}, \qquad (5.3)$$

where E_A is the first vertical ionization energy, Δ is the energy difference between the ground and the excited electronic states of PH_3^+ at the D_{3h} reference geometry and $\mathbf{1}$ is the three-dimensional unit matrix. The PE matrix as a function of the S_1 coordinate ($\boldsymbol{V}(S_1)$) is taken from Ref. and is

written as

$$\boldsymbol{V}(S_1) = \begin{pmatrix} V_A & 0 & 0 \\ 0 & V_E & 0 \\ 0 & 0 & V_E \end{pmatrix}, \tag{5.4}$$

where the matrix elements V_A and V_E are represented as modified Morse functions

$$\begin{aligned} V_j =& D_j^{(2)} \left\{1 - e^{\alpha_j (r_j - S_1)}\right\}^2 \\ &+ D_j^{(3)} \left\{1 - e^{\alpha_j (r_j - S_1)}\right\}^3 \\ &- D_j^{(2)} \left\{1 - e^{\alpha_j r_j}\right\}^2 \\ &- D_j^{(3)} \left\{1 - e^{\alpha_j r_j}\right\}^3 \qquad (j = A, E). \end{aligned} \tag{5.5}$$

$\boldsymbol{V}(S_2, S_3, S_4)$ and $\boldsymbol{V}(S_2, S_5, S_6)$ are the two $({}^2E' + {}^2A_2'') \times (e' + a_2'')$ JT/PJT subproblems involving the umbrella coordinate and the stretching and bending JT-active coordinates, respectively. The influences of the mixed expansion terms involving the breathing mode (S_1) and the umbrella mode (S_2) or the JT-active modes as well as mixed expansion terms involving the JT-active stretching and bending modes are assumed to be negligible.

5.2 *Ab initio* electronic-structure calculations

The PH_3^+ radical cation contains 17 electrons in 12 orbitals. Complete-active-space self-consistent-field (CASSCF) calculations have been performed with a full-valence active space consisting of 7 orbitals (the $3s$ and $3p$ orbitals on P and the $1s$ orbitals on the H atoms). The multireference configuration interaction (MRCI) method has been employed to account for dynamic electron correlation. The three lowest electronic states have been state-averaged in the CASSCF/MRCI calculations. The 5 core orbitals ($1s$, $2s$ and $2p$ orbitals on P) are treated as doubly occupied frozen orbitals in the MRCI calculations. The correlation-consistent polarized valence triple-ζ (cc-pVTZ) basis of Woon and Dunning [107] has been employed throughout. No symmetry constraints were imposed in the electronic-structure calculations. The energy-data have been calculated mainly along one, two and three-dimensional radial cuts. The spin-restricted coupled-cluster singles-doubles with perturbative triples [RCCSD(T)] method has been employed to compute the first vertical ionization potential (E_A) of PH_3 at the D_{3h} geometry. All *ab initio* calculations were performed with the MOLPRO quantum chemistry package [108].

5.3 Construction of the six-dimensional three-sheeted potential-energy surface of PH_3^+

The 3×3 diabatic PE matrix, given by Eqs. (5.2) to (5.5) and expanded up to 8th order in S_2, S_3, S_4 and S_2, S_5, S_6, respectively, contains 208 unknown coefficients. The eigenvalues of the PE matrix are fitted to the *ab initio* data to determine these coefficients. As the eigenvalues depend non-linearly on the parameters, the fitting is a non-linear optimization problem. The Marquardt-Levenberg algorithm has been employed to solve the high-dimensional nonlinear optimization problem. The fitting has been performed in steps to maximize the efficiency and stability of the optimization process. The fitting problem has been divided into three smaller ones as suggested by the chosen hierarchical expansion of the PE surface (Eq. (5.2)). Approximately 6000 data points with energies up to 7.0 eV with respect to the ground-state energy of PH_3^+ at the planar (D_{3h}) reference geometry have been included in the fitting procedure. Details of the fitting procedure and an analysis of the accuracy of the fit are given below.

In accordance with the hierarchical expansion of the PE operator, we started the fitting procedure with the $(E' + A_2'') \times (e' + a_2'')$ JT/PJT subproblem. The fitting procedure has been initiated with a JT/PJT Hamiltonian expanded up to 4th order. The order of expansion has then been increased in steps to achieve improved agreement with the *ab initio* data. It has been observed that an 8th order expansion in the three bending modes was necessary to reproduce the *ab initio* data with reasonable accuracy (see below). 101 unknown parameters have been optimized in this sub-problem. The three-dimensional nuclear coordinate space has been sampled with ≈ 4000 points. The root-mean-square deviation of the resulting fit is 0.04 eV. It is worth mentioning here that a third (excited) electronic state of $^2A_1'$ symmetry comes energetically below the $^2E'$ state close to the planar geometry ($-0.2 \leq S_2 \leq 0.2$) and can interact with the ground state ($^2A_2''$) through the umbrella mode (a_2''). In this interval, the $^2A_1'$ state also interacts strongly with the $^2E'$ state through the e' mode. Therefore, the data points corresponding to the $^2E'$ state are removed from the fitting procedure for the nuclear geometries $-0.2 \leq S_2 \leq 0.2$.

To illustrate the strong coupling between the electronic and the nuclear motions along the bending vibrational modes, we discuss a few representative PE cuts in the three-dimensional space of the bending coordinates. The fitted energies of the three adiabatic electronic states (red, green and blue lines, respectively) of PH_3^+ as functions of S_2 are compared with the *ab initio* data (circles) in Fig. 5.2. The low-energy region of the ground state is depicted in

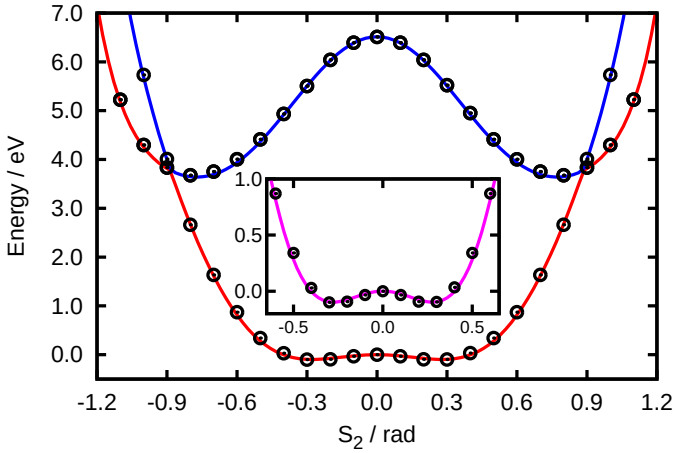

Figure 5.2: The PE functions of the ground state (red line) and the first excited state (blue line) of PH_3^+ expanded up to 8th-order in comparison with the *ab initio* data (circles). The lower energy part of the ground state is shown in the inset on an enlarged scale.

the inset on an enlarged scale. The shallow energy barrier between the two minima in the ground electronic state along S_2 has been estimated to be 0.099 eV, which is somewhat lower than those found in the previous calculations [114, 116–118]. As Fig. 5.2 shows, there exist two symmetry-allowed three-state CIs near $S_2 = \pm 0.9$ radian. These two triple intersection points are connected by a hyperline of two-state CIs when displacements in all three bending modes are considered.

Fig. 5.3 shows three selected cuts of the fitted PE surface as functions of S_5 and S_6 when S_2 is 0.55 rad. This value of S_2 is very close value of S_2 at the equilibrium geometry of neutral PH_3. Fig. 5.3(a) and (b) show two PE surface cuts perpendicular to each other, one along S_5 when $S_6 = 0.0$ rad and the other along S_6 when $S_5 = 0.0$ rad, respectively. In addition to the JT CI at $S_5 = 0.0$ rad, another two-state intersection is seen between the lower component of the $^2E'$ state and the $^2A_2''$ state at $S_5 \approx -1.4$ rad (see Fig. 5.3(a)). On the positive side of the S_5 axis, these two states are seen to have a strongly avoided crossing in the interval $1.0 \leq S_5/\text{rad} \leq 2.0$. As is seen in Fig. 5.3(b), the PE functions are symmetric in S_6. Two strongly avoided crossings among the lowest two adiabatic electronic states appear symmetrically with respect to the $S_6 = 0.0$ line. Fig. 5.3(c) shows the third representative cut of the PE surface as a function of S_6 when S_5 is 0.7 rad and $S_2 = 0.55$ rad. This slice of the PE surface is parallel to the one shown in Fig. 5.3(b), but displaced in S_5. Fig. 5.3(c) exhibits two CIs between

the ground state and the first excited state at $S_6 = \pm 1.2$ rad. These two CIs also appear symmetrically due to the reflection symmetry of the PE surface about the S_5 axis. Hence, in addition to the JT intersection, there are three more two-state CIs in the S_5-S_6 coordinate space at a fixed non-zero umbrella angle, as is seen in Fig. 5.3(a) and (c), due to the tree-fold rotational symmetry of the system.

Fig. 5.4 shows a second set of three cuts of the fitted PE surface as functions of S_5 and S_6 when S_2 is 0.9 rad. This value of S_2 is chosen because it is close to the point of three-state intersection (see Fig. 5.2). Fig. 5.4(a) and (b) show two PE surface cuts orthogonal to each other, one along S_5 when $S_6 = 0.0$ rad and the other along S_6 when $S_5 = 0.0$ rad, respectively. Fig. 5.4(c) shows the energies of the three adiabatic electronic states along the $S_5 = S_6$ line in the JT-active bending coordinate space when $S_2 = 0.9$ rad. As is seen in all three cuts in Fig. 5.4, the $^2A_2''$ state lies energetically above the $^2E'$ state at $S_2 = 0.9$ rad (see Fig. 5.2 as well) and in this region of the configuration space the upper component of the $^2E'$ state interacts with the $^2A_2''$ state. Moreover, as $S_2 = 0.9$ rad is close to the point of triple intersection, the two-state intersections and avoided crossings have come closer to the JT intersection. This demonstrates the strong dependence of the PJT interaction on the umbrella angle. The strong asymmetry of the PE functions in S_5 and the extreme steepness at large-amplitude displacements in any of the three bending coordinates, as are seen in Fig. 1, 2 and 3, explain the necessity of the inclusion of JT/PJT coupling terms up to 8th order.

To demonstrate the necessity to include JT/PJT coupling terms up to 8th order, comparisons between the results of the 8th-order fittings and those of the 6th-order fittings are presented for the two separate 3-state 3-mode JT/PJT subproblems. Fig. 5.6 compares the error of the 6th-order fitting (red points) to that of the 8th-order fitting (green points) as functions of the *ab initio* energies in the 3-dimensional bending-coordinate space. Fig. 5.5 shows the in the 3-dimensional space of the umbrella coordinate and the JT-active stretching coordinates. Fig. 5.6 and Fig. 5.5 clearly demonstrate that the 8th-order fittings are consistently giving a significantly better representation of the *ab initio* data than the 6th-order fittings in both 3-dimensional spaces. A sudden rise of errors is observed in the energy range 2–3 eV in the fitting results of bending coordinates (see Fig. 5.6), which can be explained by the fact that a major part of the seam of CIs falls in this energy range, making the fitting particularly challenging.

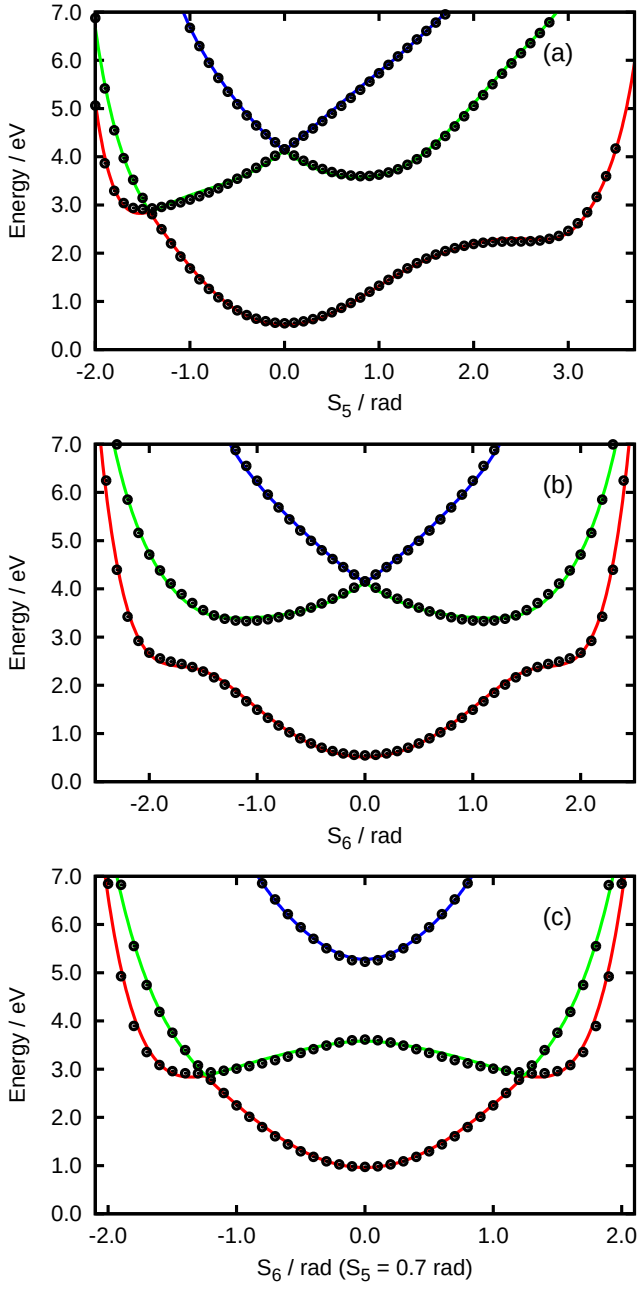

Figure 5.3: Cuts of the PE surfaces of PH_3^+ as functions of S_5 at $S_6 = 0.0$ rad (a), S_6 at $S_5 = 0.0$ rad (b) and S_6 at $S_5 = 0.7$ rad (c). $S_2 = 0.55$ rad in all three figures.

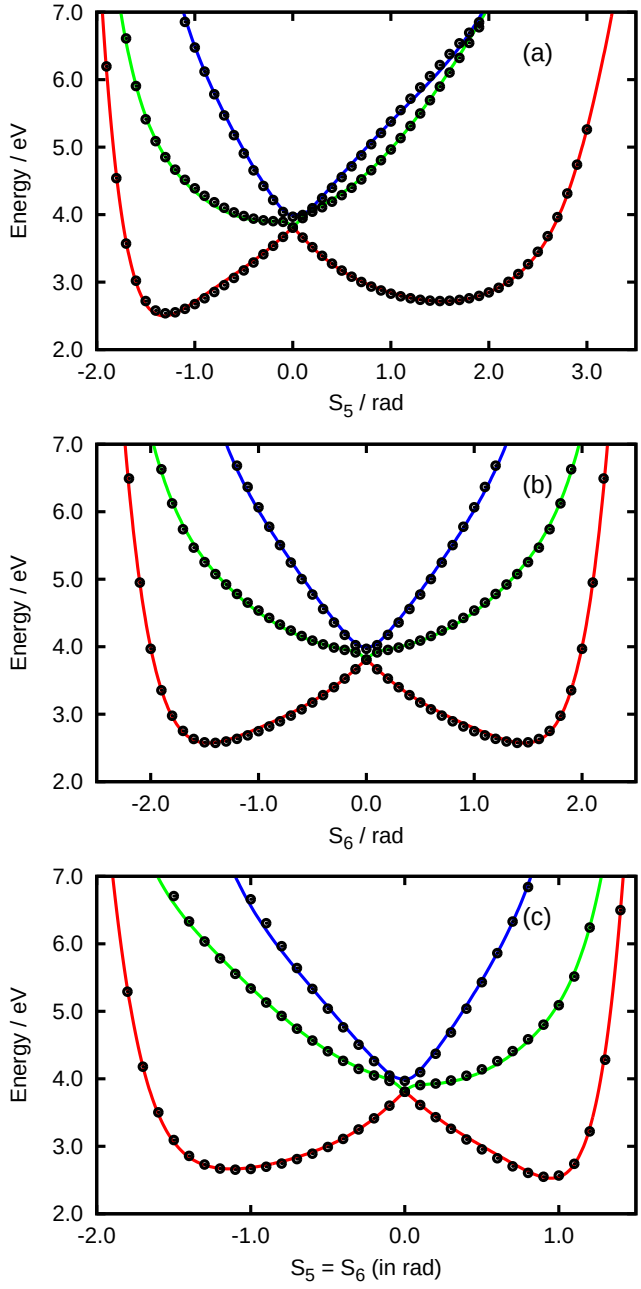

Figure 5.4: Cuts of the PE surfaces of PH_3^+ as functions of S_5 at $S_6 = 0.0$ rad (a), S_6 at $S_5 = 0.0$ rad (b) and $S_5 = S_6$ (c). $S_2 = 0.9$ rad in all three figures.

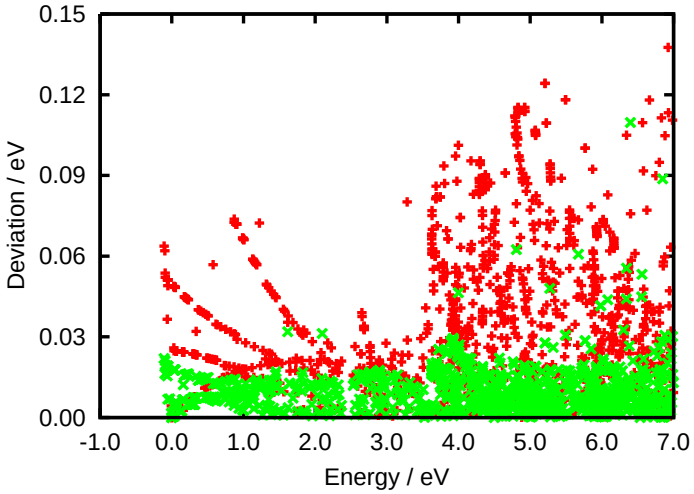

Figure 5.5: Residuals of the fit for the simultaneous fitting as function of S_2, S_3 and S_4. Red symbols represent the 6th-order fitting results and green symbols represent the results of the 8th-order fitting.

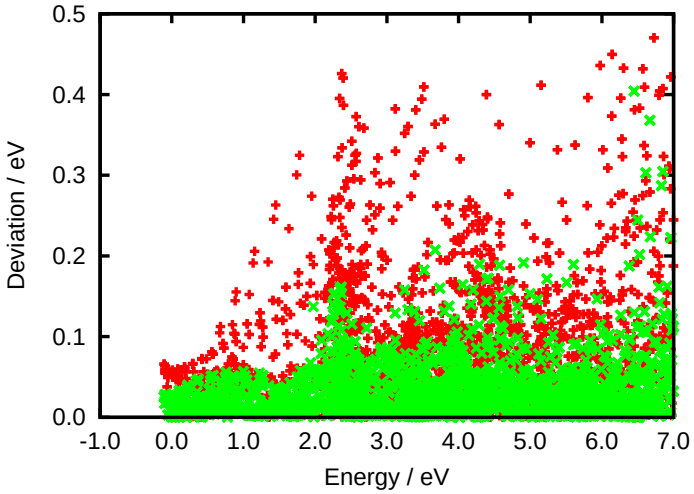

Figure 5.6: Residuals of the fit for the simultaneous fitting as function of S_2, S_5 and S_6. Red symbols represent the 6th-order fitting results and green symbols represent the results of the 8th-order fitting.

5.4 Simulation of the photoelectron spectrum and the ultrafast radiationless decay dynamics of PH_3^+

5.4.1 Nuclear kinetic-energy operator

The photoelectron spectrum and the time-dependent electronic population probabilities have been computed with the time-dependent wave-packet propagation approach. The wave packets have been propagated in time under the action of the Hamiltonian operator

$$\hat{H} = \frac{1}{2}\boldsymbol{P}^T\boldsymbol{G}\boldsymbol{P} + \hat{V}(\boldsymbol{S}) \tag{5.6}$$

where $\boldsymbol{G}$ is Wilson's kinematic matrix [46] and $\boldsymbol{P}$ is the momentum vector conjugated to $\boldsymbol{S}$. The analytic forms of the elements of the $\boldsymbol{G}$ matrix have been taken from Ref. 20. The elements of the $\boldsymbol{G}$ matrix have been approximated by their numerical values at the D_{3h} reference geometry which are given in Table 5.1.

G	$\frac{\partial}{\partial S_1}$	$\frac{\partial}{\partial S_2}$	$\frac{\partial}{\partial S_3}$	$\frac{\partial}{\partial S_4}$	$\frac{\partial}{\partial S_5}$	$\frac{\partial}{\partial S_6}$
$\frac{\partial}{\partial S_1}$	5.443×10^{-4}	0.0	0.0	0.0	0.0	0.0
$\frac{\partial}{\partial S_2}$	0.0	2.928×10^{-5}	0.0	0.0	0.0	0.0
$\frac{\partial}{\partial S_3}$	0.0	0.0	5.532×10^{-4}	0.0	1.764×10^{-5}	0.0
$\frac{\partial}{\partial S_4}$	0.0	0.0	0.0	5.532×10^{-4}	0.0	1.764×10^{-5}
$\frac{\partial}{\partial S_5}$	0.0	0.0	1.764×10^{-5}	0.0	2.518×10^{-4}	0.0
$\frac{\partial}{\partial S_6}$	0.0	0.0	0.0	1.764×10^{-5}	0.0	2.518×10^{-4}

Table 5.1: Numerical values of elements of the $\boldsymbol{G}$ matrix evaluated at D_{3h} reference geometry (in atomic units).

5.4.2 Definition of the DVR grid

To propagate the wave packets, the time-dependent Schrödinger equation has been solved variationally with the multi-configuration time-dependent Hartree (MCTDH) method [72, 86]. The MCTDH equations of motion are solved with a constant mean-field (CMF) integration scheme The PE matrix and the nuclear wave packet have been represented in a direct-product discrete variable representation (DVR) with equidistant grid points. The details of the DVR grids used are given in Table 5.2. All the vibrational modes, except the umbrella mode, have been represented by the harmonic oscillator (HO) DVR. The umbrella mode, being highly anharmonic in nature, can only poorly be approximated by the HO DVR and the employment of the so-called sin DVR may lead to a more accurate description of the dynamics along this mode. The MCTDH calculations were performed with the Heidelberg MCTDH package [119].

DOF	DVR	Range	N	n_A	n_{E_x}	n_{E_y}
S_1	HO	[-1.0 – 1.8]	30	10	5	5
S_2	sin	[-1.2 – 1.2]	75	20	15	15
S_3	HO	[-0.5 – 0.6]	20	8	5	5
S_4	HO	[-0.5 – 0.5]	20	8	5	5
S_5	HO	[-2.1 – 3.9]	65	15	10	10
S_6	HO	[-2.5 – 2.5]	65	15	12	12

Table 5.2: Details of the MCTDH calculations. Type of DVR, range (in au) and number (N) of grid points employed for each degree of freedom. n_A, n_{E_x} and n_{E_y} columns represent the numbers of SPFs used for each degree of freedom.

5.4.3 preparation of the initial wave packet

To generate the initial vibrational wave function in the electronic ground state of PH_3, a six-dimensional PE surface has been constructed for the electronic ground state (X^1A_1) of PH_3. The *ab initio* energies have been computed employing the CCSD(T) method with the correlation consistent triple-ζ basis set. Approximately 2500 data points having energies up to 1.5 eV from the energy of the molecule at D_{3h} reference geometry were taken into consideration in the construction of the PE surface. An 8th order expansion was necessary to accurately represent the energy barrier in the umbrella coordinate (1.44 eV).

Due to the large PE barrier between the two minima along the inversion coordinate, the initial wave packet has been localized in one of the two equivalent potential wells. The initial guess for the wave function was represented in the form of a direct product DVR grid (see Table 5.2) and has been propagated in imaginary time (relaxation method) to generate the localized vibrational ground state of neutral PH_3. A propagation of 20 fs was sufficient to reach convergence with respect to position and energy of the wave function. The wave function thus obtained was chosen as the initial wave packet in the cationic states (Condon approximation).

5.4.4 $\tilde{X}^2A_2''$ band of the photoelectron spectrum

To have similar resolution as in the experimental spectrum, an exponential damping (see Eq. (2.50)) of 70 fs has been applied to the autocorrelation function of the $\tilde{X}^2A_2''$ state. The theoretical spectrum thus obtained is compared with the experimental spectrum [114] in Fig. 5.7. The vibrational structure of both of the theoretical and the experimental spectra consist mainly of an single extended progression which reflects the strong excitation of the umbrella mode upon ionization. The experimental 0-0 transition, which corresponds to the first adiabatic ionization energy, has been reported to be at 9.868 eV [114]. In the theoretical spectrum the 0-0 peak appears at $\approx$ 9.878 eV. We emphasize that no empirical adjustments have been made to match the theoretical spectrum with the experiment spectrum. The excellent agreement of the two reflects (i) the high accuracy of the vertical ionization energy ($\approx$ 8.53 eV) of planar PH_3 computed at the RHF/RCCSD(T)/aug-cc-pVQZ level and (ii) the high accuracy of the PE surface of the $\tilde{X}^2A_2''$ state of PH_3^+. The first few peaks of the band carry indications of tunneling splittings of the vibrational levels of the cation. While the agreement of the intensity distribution pattern of the theoretical spectrum with the experimental spectrum is impressive, the peak-spacings in the higher-energy part of the theoretical spectrum are somewhat too low. This indicates an underestimation of the pronounced positive anharnomicity of the potential in the umbrella mode. Some additional shoulders of the vibrational peaks are observed in the high-energy tail of the theoretical and the experimental spectra, which may represent weak ($n\nu_2 + \nu_1$) combination bands.

5.4.5 $\tilde{A}^2E'$ band of the photoelectron spectrum

Ionization to the ^2E state of the PH_3^+ cation leads to the second ($\tilde{A}^2E'$) band of the photolectron spectrum. The same exponential damping of the autocorrelation function as for the $^2A_2''$ state (70 fs) has been applied to

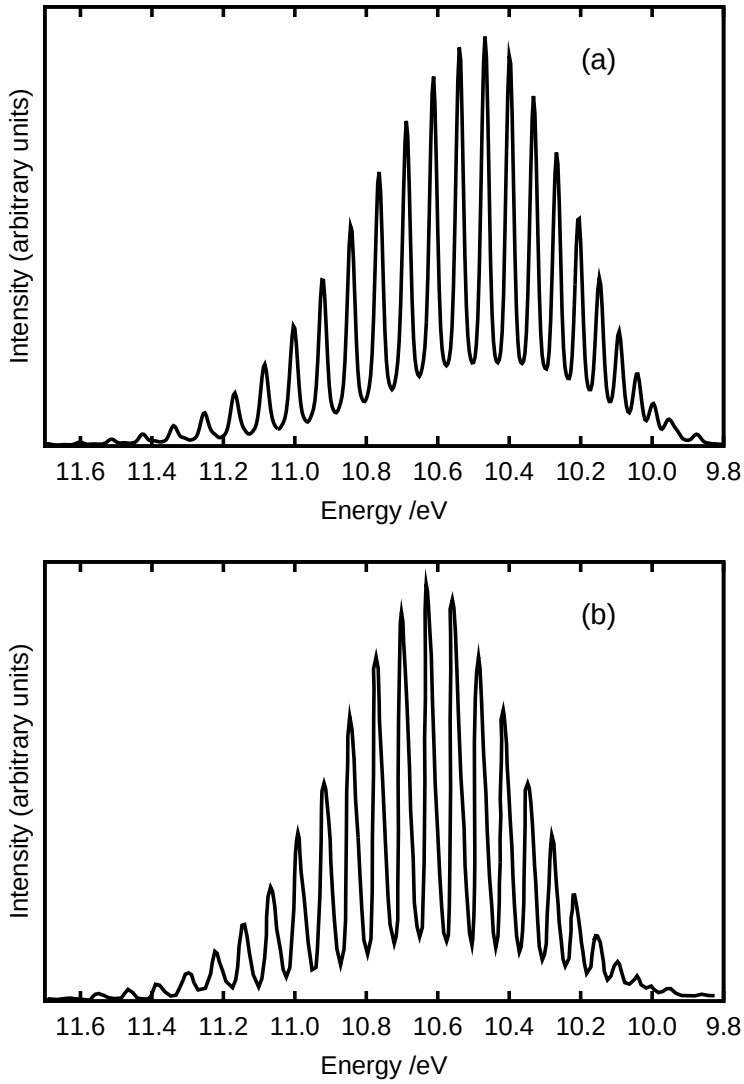

Figure 5.7: Theoretical (a) and experimental (b) $\tilde{X}^2A_2''$ photoelectron band of PH_3.

account for finite experimental resolution [114]. The large overall width of the band and the diffuseness and irregularity of the vibronic structure, both in the theoretical and in the experimental spectrum, are the consequence of strong JT and PJT coupling involving five of the six vibrational modes of PH_3^+. The typical double-hump band shape, expected for a strong Exe JT effect, is suppressed by the strong PJT coupling. The totally symmetric breathing mode is significantly excited in the $\tilde{A}^2E'$ state. It increases the width of the band and blurs the vibronic structures present in the spectra of lower dimensionality (see below). The unusually long tail of the spectrum is caused by an extended vibrational progression in the ν_1 mode due to a considerable increase in the P−H bond length up on ionization to the $\tilde{A}^2E'$ state of the cation. The low-energy flank of the theoretical spectrum exhibits irregular partly resolved vibronic structures which match quite well with the structures of the experimental spectrum.

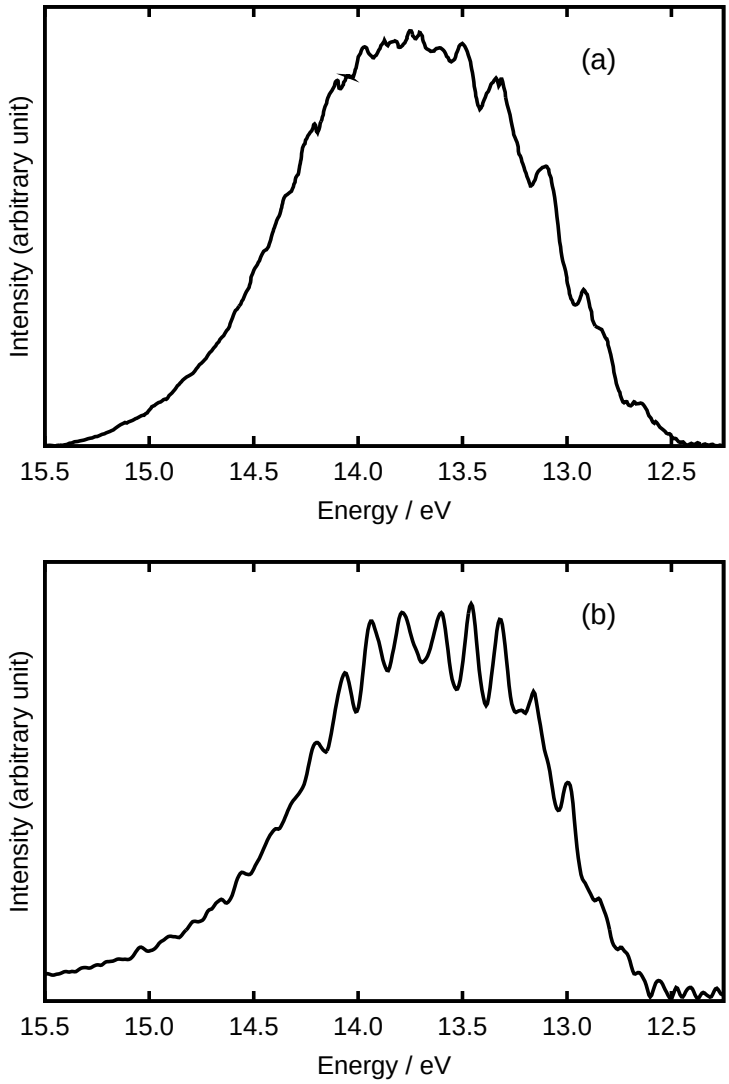

Figure 5.8: Experimental (a) and theoretical (b) $\tilde{A}^2E'$ photoelectrom band of PH_3.

To clarify the contributions of the different vibronic coupling mechanisms to the detailed vibronic structures as well as to the overall band shape, a series of theoretical spectra have been computed employing reduced dimensional Hamiltonians. Fig. 5.9(a) shows a 3-mode spectrum involving the inversion mode (S_2) and the JT-bending modes (S_5 and S_6). Inspite of being a bit narrower than the corresponding experimental band, the theoretical 3-mode spectrum already gives a good representation of the former. This result demonstrates that the three bending modes account to a large extent for the band shape of the $\tilde{A}^2E'$ state.

Inclusion of the JT-active stretching mode (S_3 and S_4) as additional mode does not change the band shape significantly, as can be seen in Fig. 5.9(b). This result reflects the weak JT activity of the degenerate stretching mode. However, the overall band is slightly broader than the 3-mode spectrum and the individual peaks also are slightly broader than in Fig. 5.9(a).

5.4.6 Electronic population dynamics

The time-dependent populations of the adiabatic electronic states up to 100 fs, assuming initial preparation of the $\tilde{A}^2E'$ state, are shown in Fig. 5.10. Starting with equal population (50% each) of the two components of the diabatic $\tilde{A}^2E'$ state, the electronic population is quickly redistributed from the upper to the lower adiabatic surface of the $\tilde{A}^2E'$ state. The lower component of the $^2E'$ state (green line) carries 80% of the total population within 4 fs. The population of the upper component (blue line) has a minimum (1%) at $\approx$ 11.5 fs. The ultrafast population transfer within the components of the $^2E'$ electronic manifold is the signature of very strong JT coupling in the $\tilde{A}^2E'$ state, primarily by the degenerate bending mode. On the other hand, the ground state (red line) becomes populated at $\approx$ 5 fs, which demonstrates the efficiency of the PJT coupling in facilitating the fast internal conversion. From 5 to 10 fs, the dynamics is dominated by a two-step population relaxation, from the highest adiabatic state to the intermediate state and from the intermediate state to the ground state. After 10 fs, the transfer of population occurs mainly between the first excited adiabatic state and the ground state. The nonadiabatic electronic population dynamics is essentially finished within 20 fs, see Fig. 5.10. After 20 fs, the system is in a state of dynamic equilibrium between the three adiabatic states. At 100 fs, the populations of the three adiabatic states are approximately 81%, 14% and 3.5% respectively.

To investigate the impact of the three bending modes on the non-adiabatic dynamics of PH_3^+, the time-dependent populations of the three adiabatic electronic states were calculated as well with the three-dimensional Hamiltonian

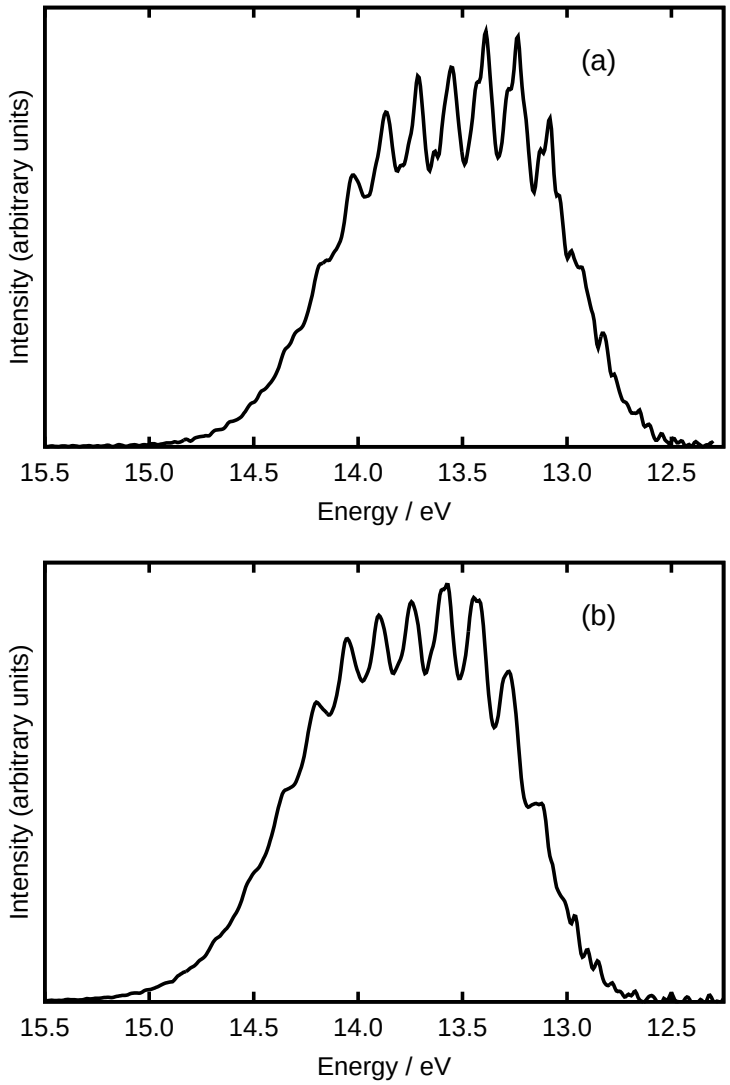

Figure 5.9: Theoretical $\tilde{A}^2E'$ photoelectrom band of PH_3 using the 3-mode Hamiltonian including the bending coordinates only (a) and the 5-mode Hamiltonian including the bending modes and the JT-stretching mode (b).

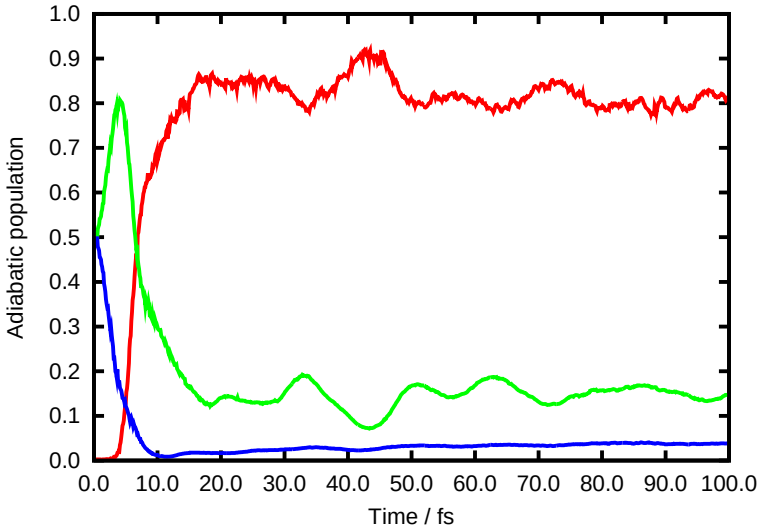

Figure 5.10: Evolution of the populations of the adiabatic ground state (red line), the first excited state (green line), and the second excited state (blue line) of PH_3^+ with time, computed with the full six-mode Hamiltonian.

including the umbrella mode and the JT-active bending modes and are shown in Fig. 5.11. The JT dynamics among the components of the $^2E'$ state occurs within 5 fs. The PJT dynamics is also ultrafast with a timescale of ≈ 10 fs. The ground electronic state gains almost 50% population within 10 fs. After 10 fs the transfer of electronic population slows down slightly and a recurrence to the excited state is observed at 20 fs. The population of the ground electronic state reaches a maximum at 45 fs. After this, the nonadiabatic electronic dynamics reaches a dynamic equilibrium. The final populations of the three adiabatic electronic states, at 100 fs, are approximately 78%, 19% and 4% respectively.

To illustrate the complexities of the non-adiabatic dynamics, time-dependent single-mode densities have also been calculated. Probability densities of the wave packet for single vibrational modes were computed by integrating out the other vibrational modes and summing over the three electronic states. The contours of these probability densities are shown in Figs. 9 and 10. Fig. 9(a) shows the probability density of the wave packet along the breathing mode (S_1). Figs. 9(b) and (c) show the same as functions of the JT-active stretching coordinates (S_3 and S_4) respectively. While the wave packet shows pronounced coherent motion along S_1 for more than 100 fs (Fig. 9(a)), the JT-active stretching modes are weakly excited and their coherence is destroyed within about 50 fs. (Figs. 9(b) and (c)). Fig. 10(a) shows the probability density of the wave packet as a function of the umbrella (S_2) coordinate and

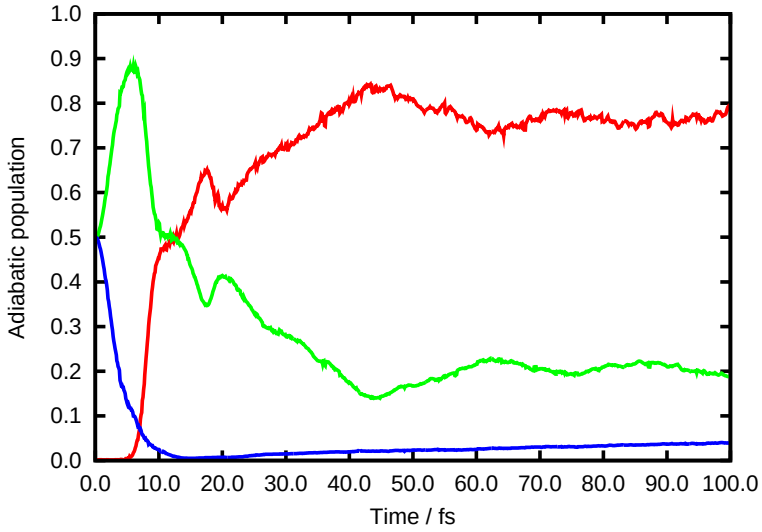

Figure 5.11: Evolution of the populations of the adiabatic ground state (red line), the first excited state (green line), and the second excited state (blue line) of PH_3^+ with time, computed with the three-mode Hamiltonian.

time. The time-dependent probability densities along S_5 and S_6 are shown in Figs. 10(b) and (c). The combined picture of the motion of the wave packet in the bending coordinates (Fig. 5.13) illustrates the complexity of the non-adiabatic dynamics of PH_3^+. The wave packet bifurcates and spreads in S_2 within 10 fs, i. e., before it reaches its classical turning point for the first time (see Fig. 5.13(a)). A look at the wave-packet dynamics in the other two bending coordinates (S_5 and S_6) reveals that the wave packet spreads along S_5 and S_6 within 10 fs (see Fig. 5.13(b) and (c)). This indicates that the wave packet get access to the seam of CIs between the $\tilde{A}^2E'$ state and the $\tilde{X}^2A_2''$ state in the 3-dimensional bending coordinate space within first 10 fs. It can be seen clearly from Fig. 5.13 that the structure of the wave packet is mostly destroyed in all three bending coordinates within 20 fs.

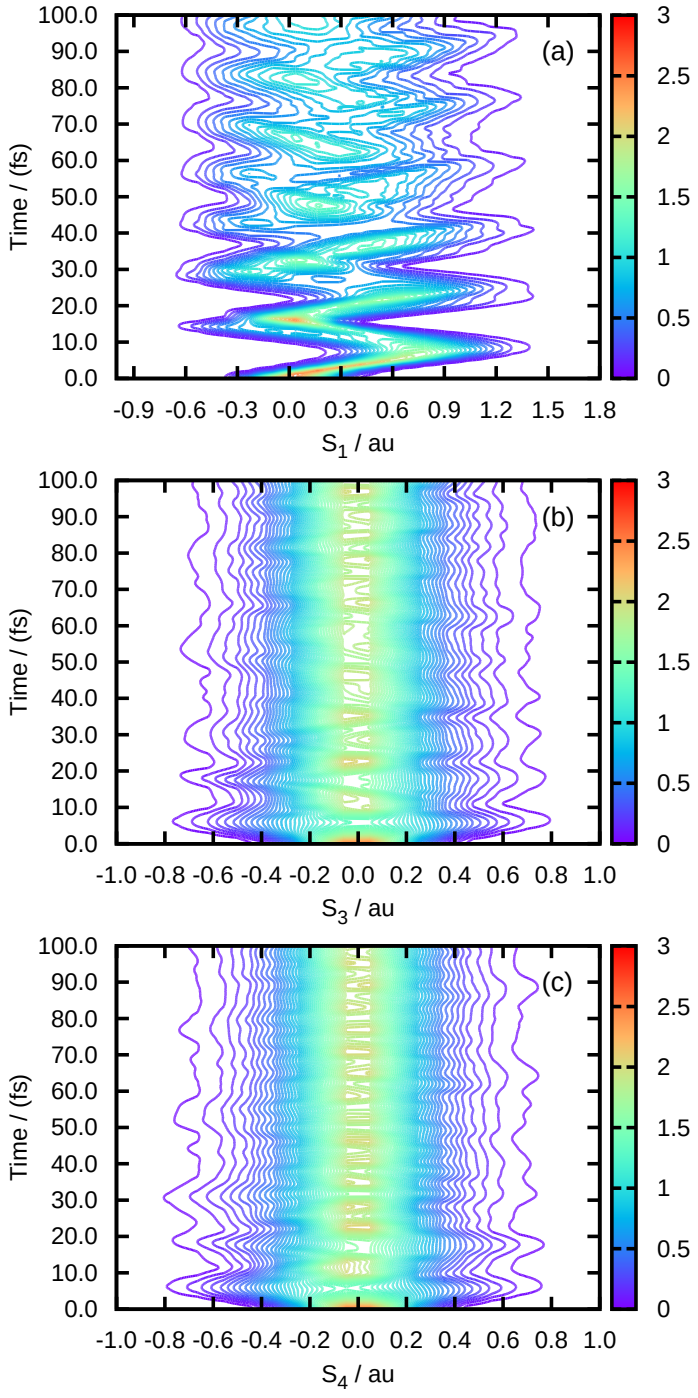

Figure 5.12: Density contour plots of the wave packet as functions of the stretching coordinates and time.

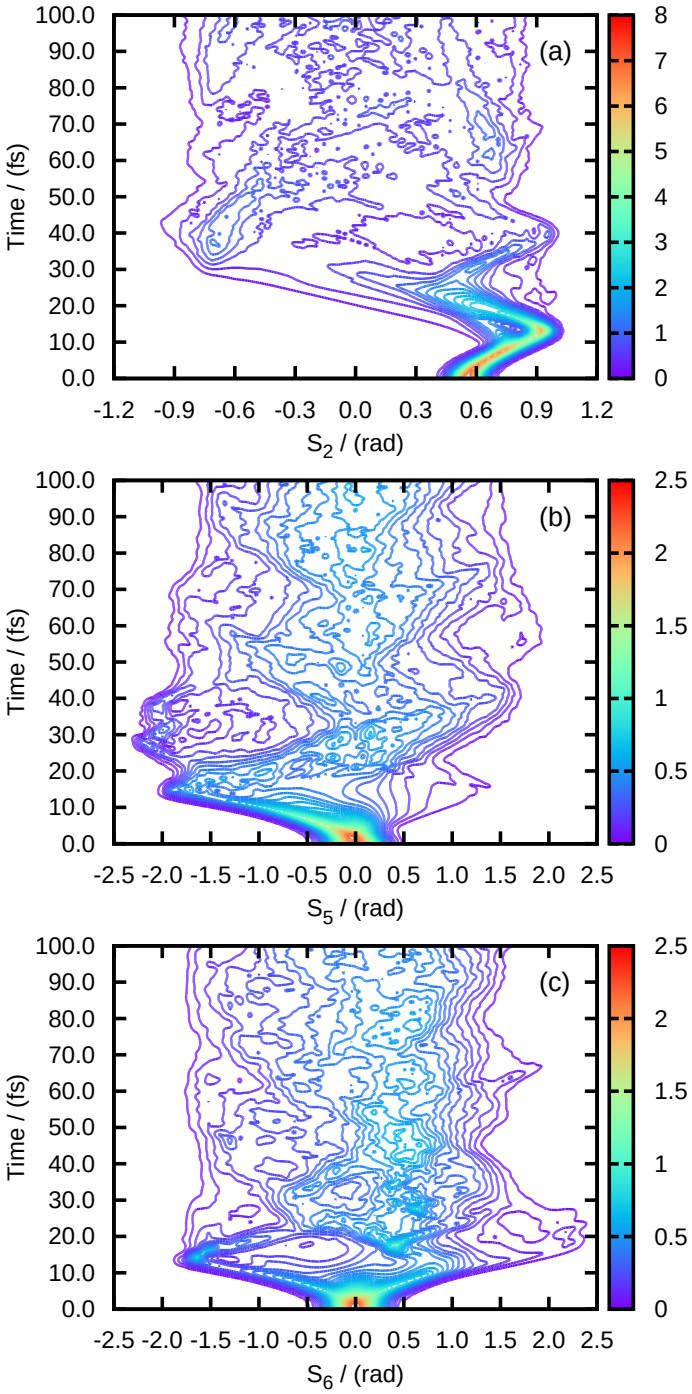

Figure 5.13: Density contour plots of the wave packet as functions of the bending coordinates and time.

Chapter 6

Application to NH_3^+

The photoionization induced excited-state dynamics of NH_3^+ and the photoelectron spectrum of ammonia have been of considerable theoretical and experimental interest over decades. It is well known that the ammonia molecule is pyramidal (C_{3v}) in its ground electronic state ($\tilde{X}^1A_1$) with electronic configuration $(1a_1)^2(2a_1)^2(1e)^4(3a_1)^2$. The outer-valence photoelectron spectrum of ammonia consists of two bands which corresponds to the ionization from the $3a_1$ and the $1e$ MO, respectively. Photoelectron spectra of ammonia have been recorded a number of times with HeI, HeII, X-ray radiation as well as synchroton radiation [113, 120–122].The most recent study by Edvardsson is considered as one with considerably higher energy resolution [123].

The first band ($\tilde{X}^2A_2'\prime$) of the photoelectron spectrum of ammonia consists mainly of a well-resolved long progression which has been assigned unambiguously to the umbrella (ν_2) mode which is significantly excited due to the large change of equilibrium geometries (from pyramidal to planar) upon ionization. However, the assignment of the second weak ν_2 progression, found in the first photoelectron band of ammonia, has been discussed controversially in the literature. While Edvardsson *et al.* have assigned it to $(\nu_4 + n\nu_2)$, the more recent theoretical investigation of Viel *et al.* suggests it to be assigned as ν_1 [41]. Therefore, a complete investigation of the ground state nuclear dynamics in its full dimensionality is required to arrive at a firm conclusion of the origin of this secondary progression form first principles.

The second ($\tilde{A}^2E'$) photoelectron band of ammonia, in contrast to the first band, is broad and exhibits only weak diffuse and irregular vibronic structure [123]. It has been speculated for a long time that the diffuseness of this band is a consequence of strong JT and PJT couplings. Haller *et al.* [124] showed by a two-mode JT calculation that the overall band shape depends strongly on the multi-mode JT activity of the cation in its excited

electronic state. Woywod *et al.* performed a full-dimensional calculation employing the linear vibronic coupling model an showed that the photoelectron spectrum and the electronic population dynamics depend not only on the strong JT effects but also on the PJT coupling of the $^2E'$ state with the $^2A_2''$ state [93]. The most recent theoretical investigation, carried out by Viel and co-workers [41], has achieved several improvements of the understanding of the excited-state dynamics of NH_3^+. One of the challenges in the theoretical investigation of the excited-state dynamics of NH_3^+ is to explain the absence of any detectable signal in the fluorescence spectrum from the $\tilde{A}^2E'$ state [125], which has been conjectured to be quenched due to the presence of an ultrafast radiationless decay channel. While the investigations of Viel *et al.* have confirmed the presence of multiple CIs, they could only show an incomplete transfer of electronic population to the ground state after ionization to the excited state [41]. Therefore, the first-principles descriptions of the ultrafast electronic population dynamics of NH_3^+ still remains a theoretical challenge. A three-sheeted six-dimensional PE surface of the ammonia cation has been constructed in this work. However, we could not yet perform a full dimensional quantum dynamical calculation due to the huge computational expense. While a six-dimensional dynamical investigation is necessary for a complete comparison of the theoretical results with the experimental findings, it is shown below that a three-dimensional calculation including the bending modes is able to reproduce the gross dynamical features of this system.

6.1 *Ab initio* electronic-structure calculations

Ab initio energies of the ground and the excited electronic states of NH_3^+ cation have been computed as functions of the six symmetry coordinates. The definitions of the symmetry coordinates have been taken to be the same as for PH_3^+. Complete-active-space self-consistent-field (CASSCF) calculations have been performed with an active space consisting of 7 orbitals (the $2s$ and $2p$ orbitals on N and the $1s$ orbitals on the H atoms). Six states have been state averaged to obtain a balanced description of the electronic wavefunction over the full range of the configuration space. The multireference configuration interaction (MRCI) method has been employed to account for dynamic electron correlation. The four lowest electronic states have been included in the MRCI calculations. Only the $1s$ orbital on N is considered as the core orbital and remained as doubly occupied frozen orbitals in all the MRCI calculations. The correlation-consistent polarized valence triple-ζ (cc-pVTZ) basis of Woon and Dunning [107] has been employed throughout. No symmetry constraints were imposed in the electronic-structure calcula-

tions. All *ab initio* calculations were performed with the MOLPRO quantum chemistry package [108].

6.2 A six-dimensional three-sheeted potential-energy surface of NH_3^+

6.2.1 Hierarchical expansion of the PE surface

The three-state three-mode $(E + A) \times (e + a)$ JT/PJT Hamiltonian (see Chapter 2), developed in this work is at the core of the three-state six-mode diabatic Hamiltonian of NH_3^+. The latter is approximated as a hierarchical expansion in terms of lower dimensional potentials. The hierarchical expansion employed here reads

$$\begin{aligned} \boldsymbol{V}(\boldsymbol{S}) = \boldsymbol{V}(0) + \boldsymbol{V}(S_1) + \boldsymbol{V}(S_2, S_3, S_4) + \boldsymbol{V}(S_2, S_5, S_6) \\ + \boldsymbol{V}(S_3, S_4, S_5, S_6) - \boldsymbol{V}(S_2), \end{aligned} \tag{6.1}$$

where $\boldsymbol{V}(S_3, S_4, S_5, S_6)$ represents the stretch-bend mixed coupling terms of JT origin which has been expanded in terms of symmetry-adapted polynomials of JT-active nuclear displacement coordinates. All the other terms have the same meaning as in Eq. (5.2). The nth order expansion of the elements $\boldsymbol{V}(S_3, S_4, S_5, S_6)$ can conveniently be expressed as the sum of a diagonal and a traceless matrix as

$$\boldsymbol{V}^{(n)}(S_3, S_4, S_5, S_6) = \begin{pmatrix} \nu_A^{(n)} & 0 & 0 \\ 0 & \nu_E^{(n)} & 0 \\ 0 & 0 & \nu_E^{(n)} \end{pmatrix} + \begin{pmatrix} 0 & 0 & 0 \\ 0 & \mathcal{W}^{(n)} & \mathcal{Z}^{(n)} \\ 0 & \mathcal{Z}^{(n)} & -\mathcal{W}^{(n)} \end{pmatrix}. \tag{6.2}$$

The expansion terms are given below explicitly correlate the JT-active stretching coordinates (S_3, S_4) with the JT-active bending coordinates (S_5, S_6) and are new here. Because the 4th-order terms are rather lengthy, we give these terms up to third order :

$$\begin{aligned} \nu_A^{(1)} &= 0 \\ \nu_A^{(2)} &= \tilde{a}_1^{(2)}(x_1x_2 + y_1y_2) \\ \nu_A^{(3)} &= \tilde{a}_1^{(3)}(x_1^2x_2 - y_1^2x_2 - 2x_1y_1y_2) \\ &\quad + \tilde{a}_2^{(3)}(x_1x_2^2 - x_1y_2^2 - 2y_1x_2y_2) \end{aligned} \tag{6.3}$$

$$\begin{aligned}
\nu_E^{(1)} &= 0 \\
\nu_E^{(2)} &= \tilde{b}_1^{(2)}(x_1x_2 + y_1y_2) \\
\nu_E^{(3)} &= \tilde{b}_1^{(3)}(x_1^2x_2 - y_1^2x_2 - 2x_1y_1y_2) \\
&\quad + \tilde{b}_2^{(3)}(x_1x_2^2 - x_1y_2^2 - 2y_1x_2y_2)
\end{aligned} \tag{6.4}$$

$$\begin{aligned}
\mathcal{W}^{(1)} &= 0 \\
\mathcal{W}^{(2)} &= \tilde{\lambda}_1^{(2)}(x_1x_2 - y_1y_2) \\
\mathcal{W}^{(3)} &= \tilde{\lambda}_1^{(3)}x_2(x_1^2 + y_1^2) + \tilde{\lambda}_2^{(3)}x_1(x_2^2 + y_2^2) \\
&\quad + \tilde{\lambda}_3^{(3)}x_1(x_1x_2 + y_1y_2) + \tilde{\lambda}_4^{(3)}x_2(x_1x_2 + y_1y_2)
\end{aligned} \tag{6.5}$$

$$\begin{aligned}
\mathcal{Z}^{(1)} &= 0 \\
\mathcal{Z}^{(2)} &= \tilde{\lambda}_1^{(2)}(-x_1y_2 - x_2y_1) \\
\mathcal{Z}^{(3)} &= \tilde{\lambda}_1^{(3)}y_2(x_1^2 + y_1^2) + \tilde{\lambda}_2^{(3)}y_1(x_2^2 + y_2^2) \\
&\quad + \tilde{\lambda}_3^{(3)}y_1(x_1x_2 + y_1y_2) + \tilde{\lambda}_4^{(3)}y_2(x_1x_2 + y_1y_2).
\end{aligned} \tag{6.6}$$

The 4-mode terms given above are necessary to improve the accuracy of the PE surface of NH_3^+. All the other members of the hierarchical expansion are functions of at most three coordinates and therefore cannot explain a simultaneous displacements in all the four JT-active coordinates. In other words, none of the expansion terms of $\boldsymbol{V}(S_3, S_4, S_5, S_6)$ can be found in any of the other expansions.

6.2.2 Fitted potential-energy surface

The unknown coefficients of the polynomial expansions are determined by fitting the eigenvalues of the 3×3 diabatic PE matrix to the *ab initio* data. In accordance with the hierarchical expansion of the PE operator (Eq. (6.1)), we started the fitting procedure with the $(E' + A_2'') \times (e' + a_2'')$ JT/PJT sub-problem. The fitting procedure has been initiated with a JT/PJT Hamiltonian expanded up to 4th order. The order of expansion has then been increased in steps to achieve improved agreement with the *ab initio* data. It has been observed that an 8th order expansion in the three bending modes was necessary to reproduce the *ab initio* data with reasonable accuracy (see below). 101 unknown parameters have been optimized in this sub-problem.

To illustrate the strong coupling between the electronic and nuclear motions along the bending vibrational modes, we discuss a few representative PE cuts in the three-dimensional space of the bending coordinates. The fitted energies of the three adiabatic electronic states (red and blue lines, respectively) of PH_3^+ as functions of S_2 are compared with the *ab initio* data (circles) in Fig. 6.1. Unlike PH_3^+, the equilibrium geometry of NH_3^+ is planar in its ground electronic state. As Fig. 5.2 shows, there exist two symmetry-allowed three-state crossings near $S_2 = \pm 1.0$ radian. These two triple intersection points are connected by a hyperline of two-state CIs when displacements in all three bending modes are considered.

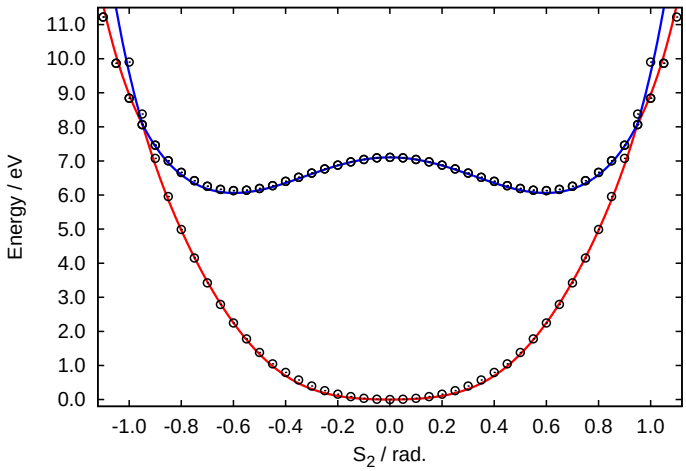

Figure 6.1: The PE functions of the ground state (red line) and the first excited state (blue line) of NH_3^+ expanded up to 8th-order in comparison with the *ab initio* data (circles).

Fig. 6.2 shows two selected cuts of the fitted PE surface as functions of S_5 and S_6 when S_2 is zero. This value of S_2 corresponds to the planar configuration and PJT coupling is completely switched off there. Fig. 6.2 show two PE surface cuts perpendicular to each other, one along S_5 when S_6 is zero and the other along S_6 when S_5 is zero, respectively. As is seen in Fig. 6.2, the PE functions are asymmetric in S_5, which is a consequence of large quadratic and higher-order JT couplings.

Fig. 6.3 shows a second set of two cuts of the fitted PE surface as functions of S_5 and S_6 when S_2 is 0.6 rad. This value of S_2 corresponds to the minimum of energy of the $^2E'$ state as a function of S_2. Fig. 6.3 shows two PE surface cuts perpendicular to each other, one along S_5 when S_6 is zero and the other along S_6 when S_5 is zero, respectively. In addition to the JT CI at $S_5 = 0$,

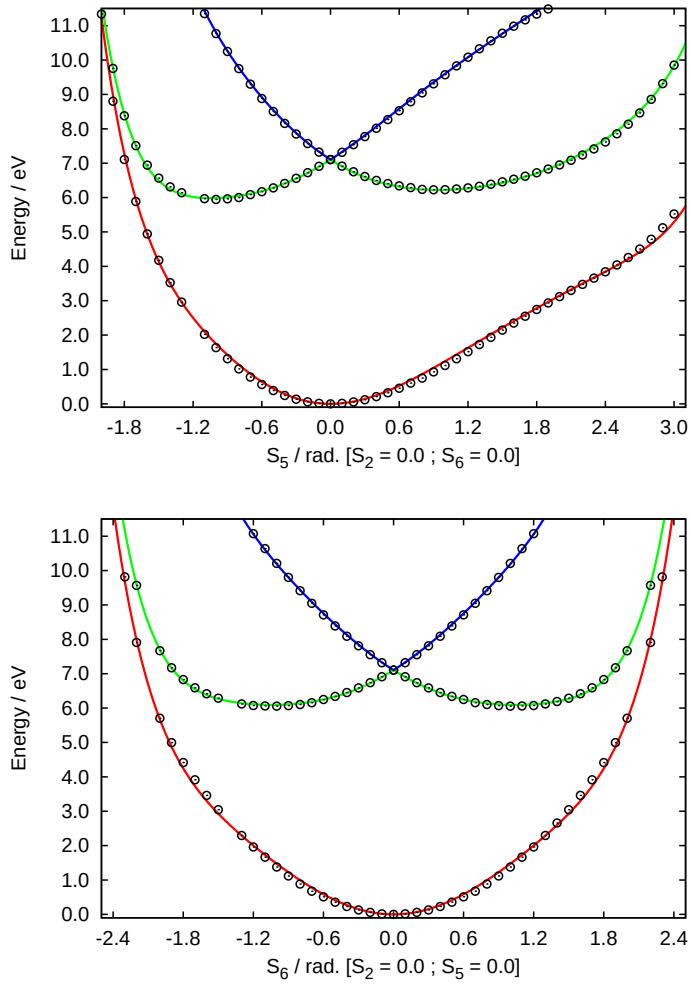

Figure 6.2: Cuts of the PE surfaces of NH_3^+ as functions of S_5 at $S_6 = 0.0$ rad (upper panel), S_6 at $S_5 = 0.0$ rad (lower panel). $S_2 = 0.0$ rad in both figures.

another two-state intersection is seen between the lower component of the $^2E'$ state and the $^2A_2''$ state at $S_5 \approx -1.4$ rad. On the positive side of the S_5 axis, these two states are seen to have a strongly avoided crossing in the interval $0.6 \leq S_5/\text{rad} \leq 2.0$. As is seen in Fig. 6.3 (lower panel), the PE functions are symmetric in S_6.

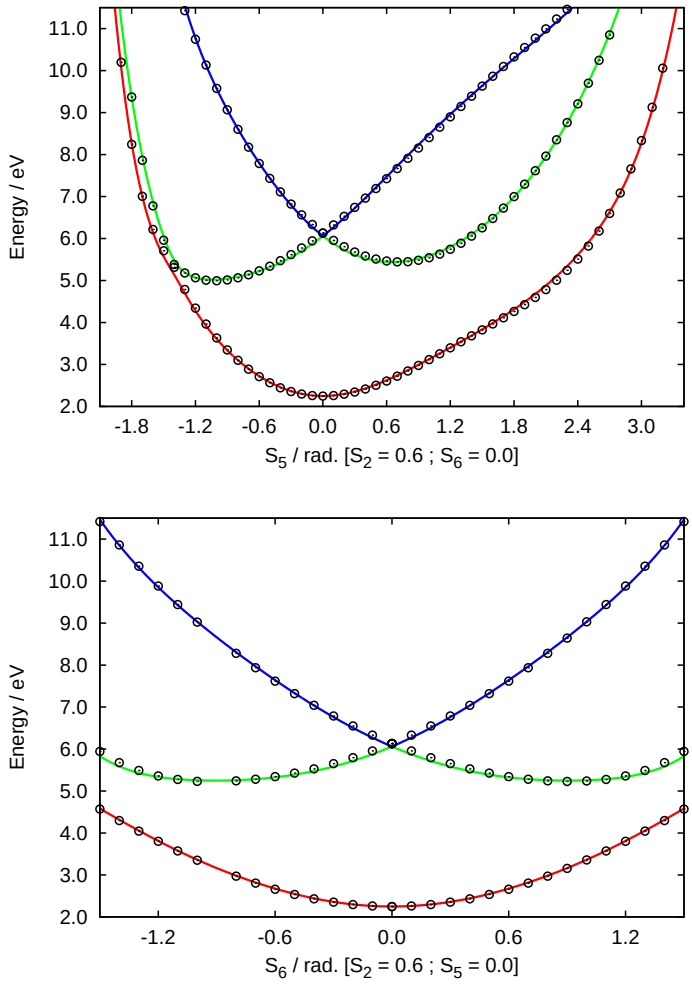

Figure 6.3: Cuts of the PE surfaces of NH_3^+ as functions of S_5 at $S_6 = 0.0$ rad (upper panel), S_6 at $S_5 = 0.0$ rad (lower panel). $S_2 = 0.6$ rad in both figures.

The difference between the hierarchical expansion used for PH_3^+ and that used here is the inclusion of mixed stretch-bend JT coupling terms. *Ab initio* data, computed as functions simultaneous displacements of the JT-active stretching and bending coordinates, have been employed to determine

these coupling terms. We present here the results for the PE surfaces fitted with the JT Hamiltonian with stretch-bend coupling terms included up to third order. Fig. 6.4 represents two diagonal cuts, one along $S_3 = S_5$ and the other along $S_3 = -S_5$. It is worthwhile to note the pronounced difference of the JT stabilization energies of these two cuts, which cannot be reproduced without the inclusion of the explicit 4-mode JT coupling terms.

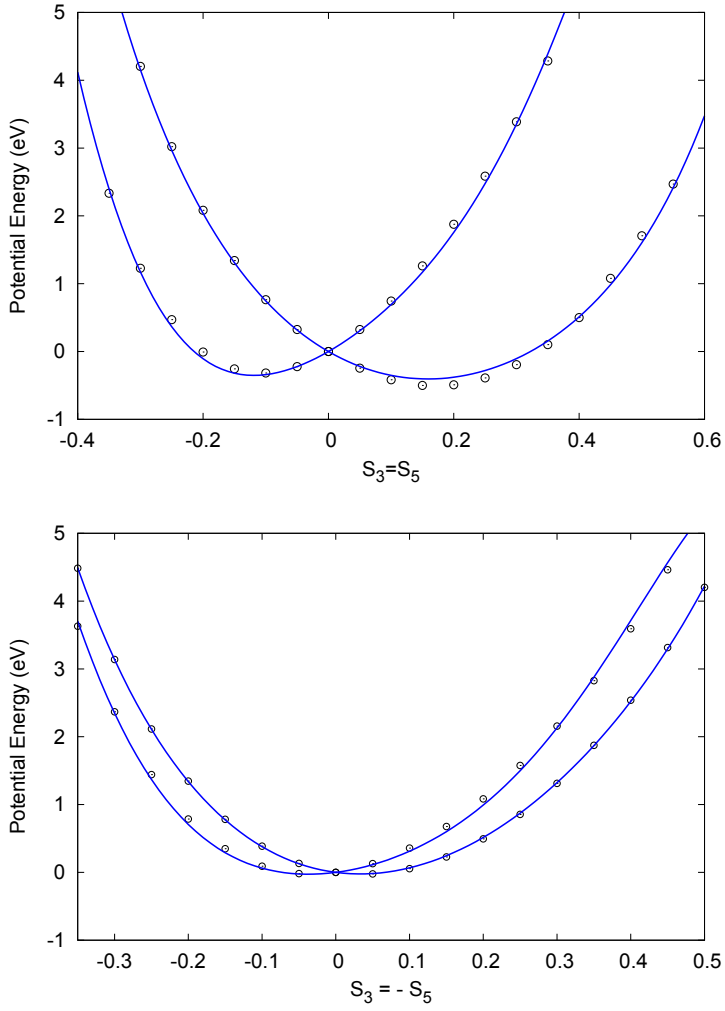

Figure 6.4: Two diagonal cuts of the PE surfaces of NH_3^+ along $S_3 = S_5$ (upper panel), and $S_3 = -S_5$ (lower panel). All the other coodinates are zero in both figures.

6.3 Simulation of the photoelectron spectrum and the ultrafast radiationless decay dynamics of NH_3^+

6.3.1 Nuclear kinetic-energy operator

The photoelectron spectrum and the time-dependent electronic population probabilities have been calculated by propagating time-dependent wave-packets under the action of the 3-dimensional Hamiltonian operator including the bending modes of vibration

$$\hat{H} = \frac{1}{2}\boldsymbol{P}^T\boldsymbol{G}\boldsymbol{P} + \hat{V}(\boldsymbol{S}) \tag{6.7}$$

where $\boldsymbol{G}$ is Wilson's kinematic matrix [46], $\boldsymbol{S} = (S_2, S_5, S_6)^T$ and $\boldsymbol{P}$ is the momentum vector conjugated to $\boldsymbol{S}$. The elements of the $\boldsymbol{G}$ matrix have been approximated by their numerical values at the D_{3h} reference geometry which are given in Table 6.1.

G	$\frac{\partial}{\partial S_2}$	$\frac{\partial}{\partial S_5}$	$\frac{\partial}{\partial S_6}$
$\frac{\partial}{\partial S_2}$	5.904×10^{-5}	0.0	0.0
$\frac{\partial}{\partial S_5}$	0.0	4.841×10^{-4}	0.0
$\frac{\partial}{\partial S_6}$	0.0	0.0	4.841×10^{-4}

Table 6.1: Numerical values of elements of the $\boldsymbol{G}$ matrix evaluated at D_{3h} reference geometry (in atomic units).

6.3.2 Preparation of the initial wave packet

The initial wave packet has been prepared in the electronic ground state of NH_3. For this reason, a three-dimensional PE surface has been constructed for the electronic ground state (X^1A_1) of NH_3. The *ab initio* energies have been computed employing the CCSD(T) method with the correlation consistent triple-ζ basis set. Approximately 800 data points having energies up to 1.5 eV from the energy of the molecule at D_{3h} reference geometry were taken into consideration in the construction of the PE surface.

Due to the large PE barrier between the two minima along the inversion coordinate, the initial wave packet has been localized in one of the two equivalent potential wells. The initial guess for the wave function was represented

in the form of a direct product DVR grid (see Table 6.2) and has been propagated in imaginary time (also known as relaxation method) to generate the localized vibrational ground state of neutral NH_3. A propagation of 25 fs was sufficient to reach convergence. The wave function thus obtained was chosen as the initial wave packet in the cationic states (Condon approximation).

DOF	DVR	Range	N	n_A	n_{E_x}	n_{E_y}
S_2	sin	[-1.1 – 1.1]	100	35	25	25
S_5	HO	[-2.0 – 3.0]	75	35	20	20
S_6	HO	[-2.5 – 2.5]	75	35	20	20

Table 6.2: Details of the MCTDH calculations. Type of DVR, range (in au) and number (N) of grid points employed for each degree of freedom. n_A, n_{E_x} and n_{E_y} columns represent the numbers of SPFs used for each degree of freedom.

6.3.3 $\tilde{X}^2A_2''$ photoelectron band of NH_3

The three-dimensional initial wave packet in the ground state of PH_3 has been evolved in time on the ground-state PE surface of PH_3^+ with the MCTDH method [72, 119]. The $\tilde{X}^2A_2''$ band of the photoelectron spectrum has been obtained by Fourier transformation of the autocorrelation function. To have similar resolution as in the experimental spectrum, a Gaussian damping of 200 fs has been applied to the autocorrelation function of the $\tilde{X}^2A_2''$ state. The theoretical spectrum thus obtained is given in Fig. 6.5. The vibrational structure of the theoretical spectrum consists mainly of an single extended progression which reflects the change of equilibrium geometry, from pyramidal to planar, upon ionization. The most intense transition corresponds to the 0-6 vibrational line both in theoretical and in experimental spectrum. An additional very weak vibrational progression has been observed in the experimental spectrum. The origin of this progression has been discussed controversially in the literature. However, the most recent theoretical study has assigned it to the excitation of the totally symmetric stretching (ν_1) vibration peaks.

6.3.4 $\tilde{A}^2E'$ photoelectron band of NH_3

Ionization to the ^2E state of the NH_3^+ cation leads to the second ($\tilde{A}^2E'$) band of the photolectron spectrum. The $\tilde{A}^2E'$ band has been simulated in a reduced dimensional calculation involving the three bending modes of

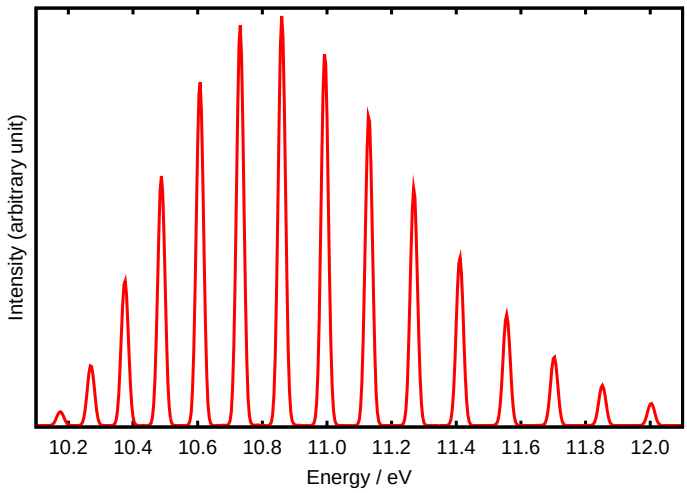

Figure 6.5: $\tilde{X}^2A_2''$ band of the photoelectron spectrum of NH_3 calculated with a 3-mode Hamiltonian.

vibration (see Fig. 6.6). An exponential damping of 50 fs has been applied to the autocorrelation function to account for finite experimental resolution. The large overall width of the band and the diffuseness and irregularity of the vibronic structure, in the experimental spectrum are the consequence of strong JT and PJT coupling involving five of the six vibrational modes of PH_3^+. The 3-mode spectrum presented here may be considered as a very crude approximation of the experimental spectrum. The clear double-hump band shape present in Fig. 6.6 reveals the presence of a strong $E\times e$ JT effect. The existence of a regular vibronic structure is as expected for a 3D model. However, we emphasize that the results are too preliminary. 6D calculations are presently in progress and we hope to obtain more complete results in the near future.

6.3.5 Electronic population dynamics

The time-dependent populations of the adiabatic electronic states have been calculated up to 100 fs after the initial preparation of the $\tilde{A}^2E'$ state, employing the 3-dimensional Hamiltonian. The results are shown in Fig. 6.7. Starting with equal population (50% each) of the two components of the diabatic $\tilde{A}^2E'$ state, the electronic population undergoes a rapid redistribution from the upper to the lower adiabatic surface of the $\tilde{A}^2E'$ state. The lower component of the $^2E'$ state (green line) receives 95% of the total population within 5 fs and the population of the upper component (blue line) reaches its minimum at $\approx 12fs$. The fast initial (first 5 fs) transfer of electronic

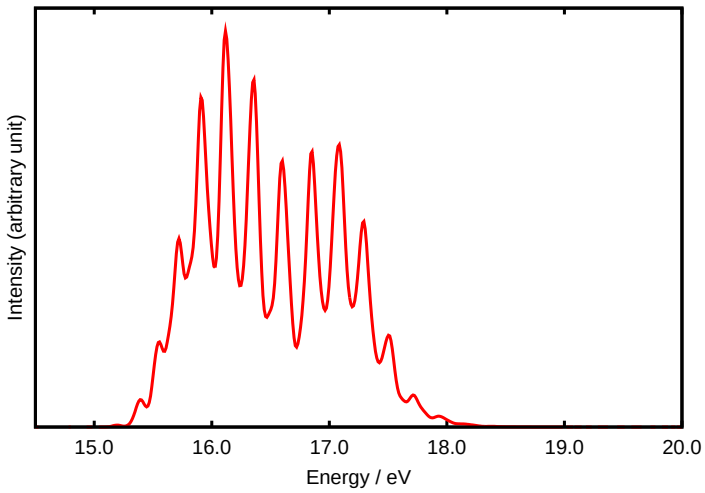

Figure 6.6: $\tilde{A}^2E'$ band of the photoelectron spectrum of NH_3 calculated with a 3-mode Hamiltonian.

population within the ^2E manifold reflects the extremely strong $E \times e$ JT effect involving the e bending mode. On the other hand, the ground state (red line) becomes populated at $\approx$ 10 fs, which demonstrates the efficiency of the PJT coupling in facilitating the fast internal conversion. At 10 fs, the ground state is almost 45% populated. However, after 10 fs transfer of electronic population slows down considerably. A small recurrence in the second excited adiabatic state is seen at about 18 fs. The excited state population starts to decay again after 20 fs and continues until 100 fs. At the end of the propagation, 68% of the total population has been transfered to the ground electronic state with $\approx$ 32% population still remaining on the excited electronic state. The total population (magenta line), as is seen in in Fig. 6.7, remains essentially constant throughout the propagation, which reflects the numerical accuracy of the integrations carried out in this calculation. The results of the present 3-mode electronic population dynamics calculation clearly illustrate the effects of the three bending modes in the strong JT/PJT-induced internal-conversion dynamics of NH_3^+. While the present results already agree qualitatively with those obtained by the other workers with a full-mode Hamiltonian [41], it is still far from being complete. We hope to obtain a complete 6-dimensional population dynamics calculation with our improved PE surface in recent future, which will explain the absence of excited state fluorescence of NH_3^+ in a more satisfactory way.

To illustrate the complexities of the non-adiabatic dynamics, time-dependent single-mode densities have also been calculated. Probability densities of the

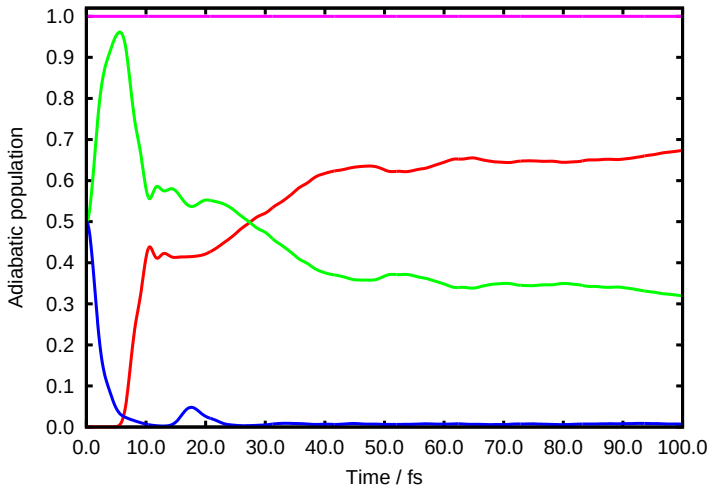

Figure 6.7: Evolution of the populations of the adiabatic ground state (red line), the first excited state (green line), and the second excited state (blue line) of NH_3^+ with time, computed with the full 3-mode Hamiltonian.

wave packet for single vibrational modes were computed by integrating out the other vibrational modes and summing over the three electronic states. The contours of these probability densities are shown in Fig. 6.8. The combined picture of the motion of the wave packet in the bending coordinates illustrates the complexity of the non-adiabatic dynamics of NH_3^+ in bending coordinate space. The wave packet spreads in S_2 within 10 fs, i. e., as soon as it reaches its classical turning point for the first time. A comparison with the PE surfaces along S_2 (see Fig. 6.1) demonstrates that most of the wave packet cannot access the point of triple intersection, at least within the first vibrational period. A look at the wave-packet dynamics in the other two bending coordinates (S_5 and S_6) reveals that the wave packet spreads along S_5 and S_6 within 10 fs. As a result, the wave packet gets access to the seam of CIs between the $\tilde{A}^2E'$ state and the $\tilde{X}^2A_2''$ state in the 3-dimensional bending coordinate space within a very short time. It can be seen from Fig. 6.8 that the structure of the wave packet is mostly destroyed in all three bending coordinates within 40 fs. To obtain additional insight into the microscopic picture of the 3-mode dynamics, single-mode densities have also been obtained for three diabatic electronic states separately and the contour plots are shown in Appendix C. Fig. C.1 for example, illustrates that the wave packet cannot cross the energy barrier in the ^2E state up to 50 fs.

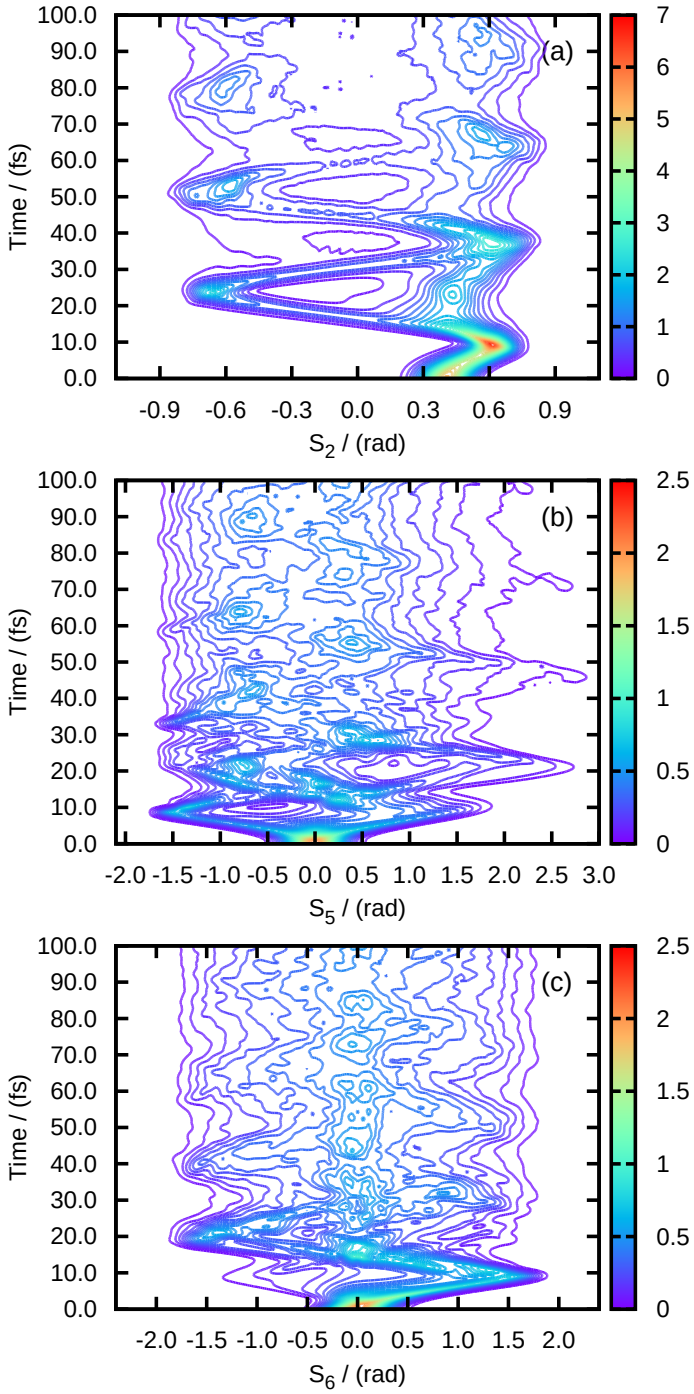

Figure 6.8: Density contour plots of the wave packet as functions of the bending coordinates and time.

Chapter 7

Summary and outlook

The systematic extension of JT theory beyond the so-called standard model is at the core of this thesis. The standard JT model has been the paradigm for the analysis of static and dynamic JT effects in Physics and Chemistry since many decades. The motivation for a substantial extension of JT theory arises from modern computational electronic-structure theory, which can provide an essentially unlimited amount of PE data for JT systems. The traditional expansions of the electrostatic PE surfaces up to second order are, in many cases, insufficient for an accurate modeling of the *ab initio* data.

The $E \times e$ JT Hamiltonian in trigonal and tetrahedral systems has been expanded up to 8th-order in nuclear displacement coordinates, replacing the Taylor expansion of the electronic Hamiltonian by an expansion in invariant polynomials, using the powerful tools of invariant theory [61, 67]. Invariant theory allows extension of JT expansions up to arbitrary orders in a straightforward way. Since C_{3v} is a subgroup of C_{6h}, D_{3h}, T_d and O_h, the $E \times e$ master JT Hamiltonian is also valid for these groups.

The theory of $(E + A) \times (e + a)$ JT/PJT coupling, which represents a generic problem in the JT theory of trigonal systems, has been developed beyond the quadratic approximation. All matrix elements of the Hamiltonian, expanded up to 8th order, have been given explicitly which can be used without any alteration to describe the strong JT/PJT couplings exhibited by many trigonal (XY_3) systems. Analogous to the high-order expansion of the $T_2 \times t_2$ JT Hamiltonian, use of the invariant theory of homogeneous polynomials ensures the most general expansion of the $(E + A) \times (e + a)$ JT/PJT Hamiltonian up to any order, while keeping the parameter space minimal. This model Hamiltonian extends the previous $(E + A) \times (e + a)$ JT/PJT model by treating all three large-amplitude bending modes in a consistent manner, while the previous model included the umbrella coordinate up to second order only [41].

The three applications of JT theory reported in this work are the P_4^+, PH_3^+ and NH_3^+ cations. While it has been known for a long time that the P_4^+ cation shows a very strong $E \times e$ JT effect in its electronic ground state, the best calculations performed so far included the JT coupling up to second order only [101–103]. The high-order expansion of the $E \times e$ JT Hamiltonian constructed during the present work has been employed to explore the influence of the higher-order JT coupling terms on the PE surfaces and on the vibronic dynamics of P_4^+. It has been shown that a 6th-order JT expansion is necessary for an accurate representation of the *ab initio* PE surface of the $\tilde{X}^2E$ state of P_4^+.

A comparison of the vibronic structures of the photoelectron spectra calculated with the 2nd-order and the 6th-order models reveals the effect of higher-order terms. The high-resolution vibronic spectra reveal a significant decrease in the spectral line density from the 2nd to the 6th-order expansion. This can be explained by the fact that at large displacements along the e vibrational mode some of the P atoms come close to each other and the repulsion between the electron densities of the atoms leads to a strong positive anharmonicity in the potential. The low-resolution envelope of the 6th-order spectrum exhibits a lower onset as well as a lower cut-off than the 2nd-order spectrum. In the experimental photoelectron spectrum [101], the E and the T_2 bands are overlapping. Moreover, the totally symmetric breathing mode is significantly excited and its progression conceals the structures arising from the JT effect [101]. For these reasons, the theoretical JT spectra presented here cannot be compared with the available experimental spectra.

A three-sheeted six-dimensional PE surface has been developed for the ground state and the first excited electronic state of the PH_3^+ cation. For the JT and PJT active vibrational modes, an 8th-order polynomial expansion of the $({}^2E' + {}^2A_2'') \times (e' + a_2'')$ JT/PJ Hamiltonian, developed in the present work, was employed. This model Hamiltonian extends the previous $(E+A) \times (e+a)$ JT/PJT model by treating all three large-amplitude bending modes in a consistent manner. The symmetry-adapted expansion reduces the cost of the *ab initio* calculations substantially by eliminating thousands of redundant nuclear configurations.

The non-adiabatic nuclear dynamics initiated by photoionization of PH_3 has been explored by performing time-dependent wave-packet propagations, employing the MCTDH method [85]. The calculations have been carried out in symmetry-adapted internal coordinates, employing an approximate kinetic-energy operator. The vibronic structure of the first two photoelectron bands of PH_3, which correspond to the ionization of the system to the ground and the first excited states of the cation respectively, has been computed. The $\tilde{X}^2A_2''$ band shows an extended single progression which reflects

the large change of the umbrella angle upon ionization. The overall bandshape of the nearly structureless second photoelectron band agrees well with the experimental spectrum. Exceptionally strong JT and PJT coupling is primarily responsible for the diffuse and irregular vibronic structure of the band.

The calculation of time-dependent populations of the three adiabatic electronic states reveals the timescales of several ultrafast decay mechanisms. The JT dynamics within the components of the ^2E state takes place within first the 5 fs. The deactivation of the excited state to the ground state, which is controlled by the strong PJT coupling, occurs on a timescale of 10 fs. More than 80% of the population of the excited electronic state decay within 20 fs. The adiabatic populations calculated employing a 3-dimensional Hamiltonian reveal the importance of the three bending modes in the ultrafast non-adiabatic dynamics of PH_3^+. Up to 10 fs, the calculation including the three bending modes shows the same timescales of the JT/PJT dynamics as does the six-mode calculation. Overall, we have shown that the $\tilde{A}^2E'$ state of PH_3^+ decays to the electronic ground state within less than 20 fs, which is truly ultrafast and may be one of the fastest internal conversion processes in nature.

In comparison to the PH_3^+ cation, the dynamics in the NH_3^+ cation has been more extensively studied both in the ground and in the excited electronic states. In spite of the success of the previous studies, we have revisited this system to explain its complex non-adiabatic dynamics in the light of an improved JT/PJT Hamiltonian. While the diffuse shape of the $\tilde{A}^2E'$ photoelectron band of NH_3 is relatively insensitive to the accuracy of the PE surfaces, the adiabatic electronic populations are more sensitive to detailed properties of the PE surfaces. A six-dimensional three-sheeted diabatic PE surface has been constructed for the NH_3^+ cation which is an improved version of the same reported by Viel and Eisfeld. Preliminary quantum dynamical calculations including three bending modes exhibit a qualitative agreement of the theoretical photoelectron bands with the experimental ones. The time-dependent electronic populations of the three adiabatic electronic states also match quite well with the previous full-mode calculations, which illustrate the predominance of the considered vibrational modes on the non-adiabatic dynamics. Work is currently in progress to obtain complete six-dimensional quantum dynamical results which include several coupling mechanisms which were not considered before for NH_3^+.

Despite the extensive research on JT theory over several decades, not everything is yet fully understood from first principles. This work illustrates some aspects of the state of the art of current research in this area which may potentially open up several directions to pursue further investigations.

The $(E + T_2) \times (e + t_2)$ JT/PJT problem may be considered as the generic problem in JT theory in tetrahedral and octahedral systems. While Köppel and coworkers have investigated this problem long ago within the framework of linear vibronic coupling theory [102], a systematic high-order expansion involving all five vibrational modes in a consistent way does not yet exist. Being symmetric in the electronic and the nuclear vector spaces, the $(E + T_2) \times (e + t_2)$ JT/PJT Hamiltonian may be expanded up to arbitrarily high orders by the use of Weyl's polarization method and other tools of invariant algebra. The availability of such an expansion would be beneficial to describe the JT/PJT activities in many strongly JT-active tetrahedral and octahedral systems. Moreover, this five-state five-mode vibronic problem includes the $E \times e$ and $T_2 \times t_2$ JT and the $(E + T_2) \times t_2$ PJT effects as its subproblems.

As is well known, the JT effect in E electronic states in tetragonal (D_{2d}, C_{4v}, D_{4h}) symmetry is fundamentally different from those in trigonal, tetrahedral or octahedral symmetry [18]. In tetragonal groups, b_1 and b_2 vibrational modes are JT active in first order, giving rise to the $E \times (b_1 + b_2)$ JT effect. On the other hand, the e vibrational mode exhibits PJT activity in first order by mixing the E state with energetically close B_2 states, which is known as the $(E + B_2) \times e$ PJT effect [126]. These JT/PJT Hamiltonians have been discussed and applied extensively in the literature considering up to quadratic coupling terms [18, 126–130]. The availability of a high-order expansion of the $(E + B_1 + B_2) \times (e + b_1 + b_2)$ JT/PJT Hamiltonian in tetragonal symmetry would be very helpful for the further theoretical studies of the spectra of tetragonal systems.

Appendices

Appendix A

Weyl's polarization method

Polarization is a very useful tool in invariant theory and representation theory of abstract mathematics. The name, Weyl's polarization, refers to the pioneering work by the famous mathematician Hermann Weyl on this topic. Here, we would try to closely follow the original formulation of Weyl.

The derivative of a polynomial $f(x)$, designated as $f'(x)$, may be defined as the coefficient of t in the expansion of $f(x+t)$ as a polynomial in t:

$$f(x+t) = f(x) + t \cdot f'(x) + \cdots \tag{A.1}$$

The above definition may be generalized for the case of multiple variables as:

$$f(\boldsymbol{x} + t\boldsymbol{y}) = f(\boldsymbol{x}) + t \cdot f_1(\boldsymbol{x}, \boldsymbol{y}) + \cdots \tag{A.2}$$

where $\boldsymbol{x} = (x_1, x_2, \cdots, x_n)$ and $\boldsymbol{y} = (y_1, y_2, \cdots, y_n)$. The coefficient of t, $f_1(\boldsymbol{x}, \boldsymbol{y})$, in the above expression (Eq. (A.2)) is called the polarized polynomial of f. The polarization is performed by applying the so-called polarization operator (D_{yx}) on the homogeneous polynomial f as

$$D_{yx} \circ (f) = \frac{\partial x}{\partial x_1} y_1 + \cdots + \frac{\partial f}{\partial x_n} y_n \tag{A.3}$$

It is interesting to note that, by identifying y_i with dx_i, the polarized form of f actually provides the total differential of f. Being a differential operator by definition, the polarization operator acts linearly and obeys all other properties of differentiation. Polarization, in other words, may be defined as a mapping of a homogeneous polynomial to a multilinear form, from which it is straightforward to retrieve the original one.

Appendix B

Matrix elements of the $(E + A) \times (e + a)$ JT/PJT Hamiltonian up to 8th order

The polynomials representing the elements of the Hamiltonian matrix are given below. $\mathcal{H}_{ij}^{(n)}$ represents the nth order element in the ith row and jth column, where $i, j = x, y, z$. Only the elements of the upper triangle of the real-symmetric matrices are given.

$$
\begin{aligned}
\mathcal{H}_{zz}^{(0)} &= E_A \\
\mathcal{H}_{zz}^{(1)} &= 0 \\
\mathcal{H}_{zz}^{(2)} &= b_1^{(2)} z^2 + b_2^{(2)} (x^2 + y^2) \\
\mathcal{H}_{zz}^{(3)} &= b_1^{(3)} (x^3 - 3xy^2) \\
\mathcal{H}_{zz}^{(4)} &= b_1^{(4)} z^4 + b_2^{(4)} z^2 (x^2 + y^2) + b_3^{(4)} (x^2 + y^2)^2 \\
\mathcal{H}_{zz}^{(5)} &= b_1^{(5)} z^2 (x^3 - 3xy^2) + b_2^{(5)} (x^5 - 2x^3 y^2 - 3xy^4) \\
\mathcal{H}_{zz}^{(6)} &= b_1^{(6)} z^6 + b_2^{(6)} z^4 (x^2 + y^2) + b_3^{(6)} z^2 (x^2 + y^2)^2 \\
&\quad + b_4^{(6)} (x^2 + y^2)^3 + b_5^{(6)} (x^3 - 3xy^2)^2 \\
\mathcal{H}_{zz}^{(7)} &= b_1^{(7)} z^4 (x^3 - 3xy^2) + b_2^{(7)} z^2 (x^2 + y^2)(x^3 - 3xy^2) \\
&\quad + b_3^{(7)} (x^4 + 2x^2 y^2 + y^4)(x^3 - 3xy^2) \\
\mathcal{H}_{zz}^{(8)} &= b_1^{(8)} z^8 + b_2^{(8)} z^6 (x^2 + y^2) + b_3^{(8)} z^4 (x^4 + 2x^2 y^2 + y^4) \\
&\quad + b_4^{(8)} z^2 (x^2 + y^2)^3 + b_5^{(8)} z^2 (x^3 - 3xy^2)^2 \\
&\quad + b_6^{(8)} (x^2 + y^2)^4 + b_7^{(8)} (x^2 + y^2)(x^3 - 3xy^2)^2
\end{aligned}
\tag{B.1}
$$

$$
\begin{aligned}
\mathcal{H}_{xz}^{(0)} &= 0 \\
\mathcal{H}_{xz}^{(1)} &= 0 \\
\mathcal{H}_{xz}^{(2)} &= c_1^{(2)} zx \\
\mathcal{H}_{xz}^{(3)} &= c_1^{(3)} z(x^2-y^2) \\
\mathcal{H}_{xz}^{(4)} &= c_1^{(4)} z^2(zx) + c_2^{(4)} zx(x^2+y^2) \\
\mathcal{H}_{xz}^{(5)} &= c_1^{(5)} z^3(x^2-y^2) + c_2^{(5)} zx(x^3-3xy^2) + c_3^{(5)} z(x^4-y^4) \\
\mathcal{H}_{xz}^{(6)} &= c_1^{(6)} xz^5 + c_2^{(6)} xz^3(x^2+y^2) + c_3^{(6)} zx(x^2+y^2)^2 \\
&\quad + c_4^{(6)} z(x^2-y^2)(x^3-3xy^2) \\
\mathcal{H}_{xz}^{(7)} &= c_1^{(7)} z^5(x^2-y^2) + c_2^{(7)} xz^3(x^3-3xy^2) \\
&\quad + c_3^{(7)} z(x^2-y^2)(x^4+2x^2y^2+y^4) \\
\mathcal{H}_{xz}^{(8)} &= c_1^{(8)} xz^7 + c_2^{(8)} xz^5(x^2+y^2) + c_3^{(8)} xz^3(x^4+2x^2y^2+y^4) \\
&\quad + c_4^{(8)} xz(x^2+y^2)^3 + c_5^{(8)} xz(x^3-3xy^2)^2 \\
&\quad + c_6^{(8)} z^3(x^2-y^2)(x^3-3xy^2) \\
&\quad + c_7^{(8)} z(x^2-y^2)(x^2+y^2)(x^3-3xy^2)
\end{aligned}
\tag{B.2}
$$

$$
\begin{aligned}
\mathcal{H}_{yz}^{(0)} &= 0 \\
\mathcal{H}_{yz}^{(1)} &= 0 \\
\mathcal{H}_{yz}^{(2)} &= c_1^{(2)} zy \\
\mathcal{H}_{yz}^{(3)} &= c_1^{(3)} (-2xy) z \\
\mathcal{H}_{yz}^{(4)} &= c_1^{(4)} yz^3 + c_2^{(4)} zy(x^2+y^2) \\
\mathcal{H}_{yz}^{(5)} &= c_1^{(5)} z^3(-2xy) + c_2^{(5)} zy(x^3-3xy^2) + c_3^{(5)} z(-2xy)(x^2+y^2) \\
\mathcal{H}_{yz}^{(6)} &= c_1^{(6)} yz^5 + c_2^{(6)} yz^3(x^2+y^2) + c_3^{(6)} yz(x^2+y^2)^2 \\
&\quad + c_4^{(6)} z(-2xy)(x^3-3xy^2) \\
\mathcal{H}_{yz}^{(7)} &= c_1^{(7)} z^5(-2xy) + c_2^{(7)} yz^3(x^3-3xy^2) \\
&\quad + c_3^{(7)} z(-2xy)(x^4+2x^2y^2+y^4) \\
\mathcal{H}_{yz}^{(8)} &= c_1^{(8)} yz^7 + c_2^{(8)} yz^5(x^2+y^2) + c_3^{(8)} yz^3(x^4+2x^2y^2+y^4) \\
&\quad + c_4^{(8)} yz(x^2+y^2)^3 + c_5^{(8)} yz(x^3-3xy^2)^2 \\
&\quad + c_6^{(8)} z^3(-2xy)(x^3-3xy^2) + c_7^{(8)} z(-2xy)(x^2+y^2)(x^3-3xy^2)
\end{aligned}
\tag{B.3}
$$

$$
\begin{aligned}
\mathcal{H}^{(0)}_{xx} &= E_E \\
\mathcal{H}^{(1)}_{xx} &= a^{(1)}_1 x \\
\mathcal{H}^{(2)}_{xx} &= a^{(2)}_1 z^2 + a^{(2)}_2 (x^2+y^2) + a^{(2)}_3 (x^2-y^2) \\
\mathcal{H}^{(3)}_{xx} &= a^{(3)}_1 (x^3 - 3xy^2) + a^{(3)}_2 x(x^2+y^2) + a^{(3)}_3 z^2 x \\
\mathcal{H}^{(4)}_{xx} &= a^{(4)}_1 z^4 + a^{(4)}_2 (x^2+y^2)^2 + a^{(4)}_3 z^2 (x^2+y^2) \\
&\quad + a^{(4)}_4 (x^4 - 6x^2y^2 + y^4) + a^{(4)}_5 (x^4 - y^4) + a^{(4)}_6 z^2 (x^2-y^2) \\
\mathcal{H}^{(5)}_{xx} &= a^{(5)}_1 z^2 (x^3 - 3xy^2) + a^{(5)}_2 (x^2+y^2)(x^3 - 3xy^2) \\
&\quad + a^{(5)}_3 z^4 x + a^{(5)}_4 z^2 x (x^2+y^2) + a^{(5)}_5 x (x^2+y^2)^2 \\
&\quad + a^{(5)}_6 (x^3 - 3xy^2)(x^2-y^2) \\
\mathcal{H}^{(6)}_{xx} &= a^{(6)}_1 z^6 + a^{(6)}_2 z^4 (x^2+y^2) + a^{(6)}_3 z^2 (x^2+y^2)^2 + a^{(6)}_4 (x^2+y^2)^3 \\
&\quad + a^{(6)}_5 (x^3 - 3xy^2)^2 + a^{(6)}_6 z^4 (x^2-y^2) + a^{(6)}_7 z^2 (x^4 - y^4) \\
&\quad + a^{(6)}_8 x z^2 (x^3 - 3xy^2) + a^{(6)}_9 z^2 (x^4 - 6x^2y^2 + y^4) \\
&\quad + a^{(6)}_{10} (x^2+y^2)^2 (x^2-y^2) + a^{(6)}_{11} (x^2+y^2)(x^4 - 6x^2y^2 + y^4) \\
\mathcal{H}^{(7)}_{xx} &= a^{(7)}_1 z^4 (x^3 - 3xy^2) + a^{(7)}_2 z^2 (x^2+y^2)(x^3 - 3xy^2) \\
&\quad + a^{(7)}_3 (x^4 + 2x^2y^2 + y^4)(x^3 - 3xy^2) + a^{(7)}_4 x z^6 + a^{(7)}_5 x z^4 (x^2+y^2) \\
&\quad + a^{(7)}_6 x z^2 (x^4 + 2x^2y^2 + y^4) + a^{(7)}_7 (x^2-y^2)(z^2)(x^3 - 3xy^2) \\
&\quad + a^{(7)}_8 x (x^3 - 3xy^2)^2 + a^{(7)}_9 (x^4 - 6x^2y^2 + y^4)(x^3 - 3xy^2) \\
&\quad + a^{(7)}_{10} x (x^2+y^2)^3 \\
\mathcal{H}^{(8)}_{xx} &= a^{(8)}_1 z^8 + a^{(8)}_2 z^6 (x^2+y^2) + a^{(8)}_3 z^4 (x^4 + 2x^2y^2 + y^4) \\
&\quad + a^{(8)}_4 z^2 (x^2+y^2)^3 + a^{(8)}_5 z^2 (x^3 - 3xy^2)^2 + a^{(8)}_6 (x^2+y^2)^4 \\
&\quad + a^{(8)}_7 (x^2+y^2)(x^3 - 3xy^2)^2 + a^{(8)}_8 z^6 (x^2-y^2) \\
&\quad + a^{(8)}_9 z^4 (x^2+y^2)(x^2-y^2) \\
&\quad + a^{(8)}_{10} z^2 (x^4 + 2x^2y^2 + y^4)(x^2-y^2) + a^{(8)}_{11} x z^4 (x^3 - 3xy^2) \\
&\quad + a^{(8)}_{12} x z^2 (x^2+y^2)(x^3 - 3xy^2) + a^{(8)}_{13} z^4 (x^4 - 6x^2y^2 + y^4) \\
&\quad + a^{(8)}_{14} z^2 (x^2+y^2)(x^4 - 6x^2y^2 + y^4) \\
&\quad + a^{(8)}_{15} (x^8 + 2x^6y^2 - 2x^2y^6 - y^8) \\
&\quad + a^{(8)}_{16} (x^8 - 7x^6y^2 + 15x^4y^4 - 9x^2y^6) \\
&\quad + a^{(8)}_{17} (x^8 - 4x^6y^2 - 10x^4y^4 - 4x^2y^6 + y^8)
\end{aligned}
\tag{B.4}
$$

$$
\begin{aligned}
\mathcal{H}_{xy}^{(0)} &= 0 \\
\mathcal{H}_{xy}^{(1)} &= -a_1^{(1)} y \\
\mathcal{H}_{xy}^{(2)} &= a_3^{(2)}(2xy) \\
\mathcal{H}_{xy}^{(3)} &= -a_2^{(3)} y(x^2+y^2) - a_3^{(3)} z^2 y \\
\mathcal{H}_{xy}^{(4)} &= -2a_4^{(4)}(2xy)(x^2-y^2) + a_5^{(4)}(2xy)(x^2+y^2) + a_6^{(4)} z^2(2xy) \\
\mathcal{H}_{xy}^{(5)} &= -a_3^{(5)} z^4 y - a_4^{(5)} z^2 y(x^2+y^2) - a_5^{(5)} y(x^2+y^2)^2 \\
&\quad + a_6^{(5)}(2xy)(x^3-3xy^2) \\
\mathcal{H}_{xy}^{(6)} &= a_6^{(6)} z^4(2xy) + a_7^{(6)} z^2(2xy)(x^2+y^2) - a_8^{(6)} z^2 y(x^3-3xy^2) \\
&\quad - 2a_9^{(6)} z^2(2xy)(x^2-y^2) + a_{10}^{(6)}(2xy)(x^2+y^2)^2 \\
&\quad - 2a_{11}^{(6)}(2xy)(x^4-y^4) \\
\mathcal{H}_{xy}^{(7)} &= -a_4^{(7)} y z^6 - a_5^7 y z^4(x^2+y^2) - a_6^{(7)} y(z^2)(x^4+2x^2y^2+y^4) \\
&\quad + a_7^{(7)}(2xy)(z^2)(x^3-3xy^2) + a_8^{(7)} y(x^3-3xy^2)^2 \\
&\quad + 4a_9^{(7)} xy(x^2-y^2)(x^3-3xy^2) + a_{10}^{(7)} y(x^2+y^2)^3 \\
\mathcal{H}_{xy}^{(8)} &= a_8^{(8)}(2xy)z^6 + a_9^{(8)} z^4(x^2+y^2)(2xy) \\
&\quad + a_{10}^{(8)} z^2(x^4+2x^2y^2+y^4)(2xy) \\
&\quad - a_{11}^{(8)} y z^4(x^3-3xy^2) - a_{12}^{(8)} y z^2(x^2+y^2)(x^3-3xy^2) \\
&\quad - 4a_{13}^{(8)} xy z^4(x^2-y^2) - 4a_{14}^{(8)} xy z^2(x^2+y^2)(x^2-y^2) \\
&\quad + 2a_{15}^{(8)}(x^7y+3x^5y^3+3x^3y^5+xy^7) \\
&\quad + 2a_{16}^{(8)}(x^7y-6x^5y^3+9x^3y^5) \\
&\quad - 4a_{17}^{(8)}(x^7y+x^5y^3-x^3y^5-xy^7)
\end{aligned}
\tag{B.5}
$$

$$
\begin{aligned}
\mathcal{H}^{(0)}_{yy} &= a^{(0)}_1 \\
\mathcal{H}^{(1)}_{yy} &= -a^{(1)}_1 x \\
\mathcal{H}^{(2)}_{yy} &= a^{(2)}_1 z^2 + a^{(2)}_2 (x^2+y^2) - a^{(2)}_3 (x^2-y^2) \\
\mathcal{H}^{(3)}_{yy} &= a^{(3)}_1 (x^3 - 3xy^2) - a^{(3)}_2 x(x^2+y^2) - a^{(3)}_3 z^2 x \\
\mathcal{H}^{(4)}_{yy} &= a^{(4)}_1 z^4 + a^{(4)}_2 (x^2+y^2)^2 + a^{(4)}_3 z^2 (x^2+y^2) \\
&\quad - a^{(4)}_4 (x^4 - 6x^2y^2 + y^4) - a^{(4)}_5 (x^4 - y^4) - a^{(4)}_6 z^2 (x^2-y^2) \\
\mathcal{H}^{(5)}_{yy} &= a^{(5)}_1 z^2 (x^3 - 3xy^2) + a^{(5)}_2 (x^2+y^2)(x^3 - 3xy^2) \\
&\quad - a^{(5)}_3 z^4 x - a^{(5)}_4 z^2 x (x^2+y^2) - a^{(5)}_5 x (x^2+y^2)^2 \\
&\quad - a^{(5)}_6 (x^3 - 3xy^2)(x^2-y^2) \\
\mathcal{H}^{(6)}_{yy} &= a^{(6)}_1 z^6 + a^{(6)}_2 z^4 (x^2+y^2) + a^{(6)}_3 z^2 (x^2+y^2)^2 + a^{(6)}_4 (x^2+y^2)^3 \\
&\quad + a^{(6)}_5 (x^3 - 3xy^2)^2 - a^{(6)}_6 z^4 (x^2-y^2) - a^{(6)}_7 z^2 (x^4 - y^4) \\
&\quad - a^{(6)}_8 x z^2 (x^3 - 3xy^2) - a^{(6)}_9 z^2 (x^4 - 6x^2y^2 + y^4) \\
&\quad - a^{(6)}_{10} (x^2+y^2)^2 (x^2-y^2) - a^{(6)}_{11} (x^2+y^2)(x^4 - 6x^2y^2 + y^4) \\
\mathcal{H}^{(7)}_{yy} &= a^{(7)}_1 z^4 (x^3 - 3xy^2) + a^{(7)}_2 z^2 (x^2+y^2)(x^3 - 3xy^2) \\
&\quad + a^{(7)}_3 (x^4 + 2x^2y^2 + y^4)(x^3 - 3xy^2) - a^{(7)}_4 x z^6 \\
&\quad - a^{(7)}_5 x z^4 (x^2+y^2) - a^{(7)}_6 x z^2 (x^4 + 2x^2y^2 + y^4) \\
&\quad - a^{(7)}_7 (x^2-y^2)(z^2)(x^3 - 3xy^2) - a^{(7)}_8 x (x^3 - 3xy^2)^2 \\
&\quad - a^{(7)}_9 (x^4 - 6x^2y^2 + y^4)(x^3 - 3xy^2) - a^{(7)}_{10} x (x^2+y^2)^3 \\
\mathcal{H}^{(8)}_{yy} &= a^{(8)}_1 z^8 + a^{(8)}_2 z^6 (x^2+y^2) + a^{(8)}_3 z^4 (x^4 + 2x^2y^2 + y^4) \\
&\quad + a^{(8)}_4 z^2 (x^2+y^2)^3 + a^{(8)}_5 z^2 (x^3 - 3xy^2)^2 \\
&\quad + a^{(8)}_6 (x^2+y^2)^4 + a^{(8)}_7 (x^2+y^2)(x^3 - 3xy^2)^2 \\
&\quad - a^{(8)}_8 z^6 (x^2-y^2) - a^{(8)}_9 z^4 (x^2+y^2)(x^2-y^2) \\
&\quad - a^{(8)}_{10} z^2 (x^4 + 2x^2y^2 + y^4)(x^2-y^2) - a^{(8)}_{11} x z^4 (x^3 - 3xy^2) \\
&\quad - a^{(8)}_{12} x z^2 (x^2+y^2)(x^3 - 3xy^2) - a^{(8)}_{13} z^4 (x^4 - 6x^2y^2 + y^4) \\
&\quad - a^{(8)}_{14} z^2 (x^2+y^2)(x^4 - 6x^2y^2 + y^4) \\
&\quad - a^{(8)}_{15} (x^8 + 2x^6y^2 - 2x^2y^6 - y^8) \\
&\quad - a^{(8)}_{16} (x^8 - 7x^6y^2 + 15x^4y^4 - 9x^2y^6) \\
&\quad - a^{(8)}_{17} (x^8 - 4x^6y^2 - 10x^4y^4 - 4x^2y^6 + y^8)
\end{aligned}
\tag{B.6}
$$

Appendix C

State-resolved density contour plots of the 3D wavepacket of NH_3^+

Single-mode density contour plots have already been shown in Chapter 6, which represents as summed over the three diabatic electronic states. Here, we present the density contour plots along the three bending modes of NH_3^+ separately for each of the three diabatic electronic states.

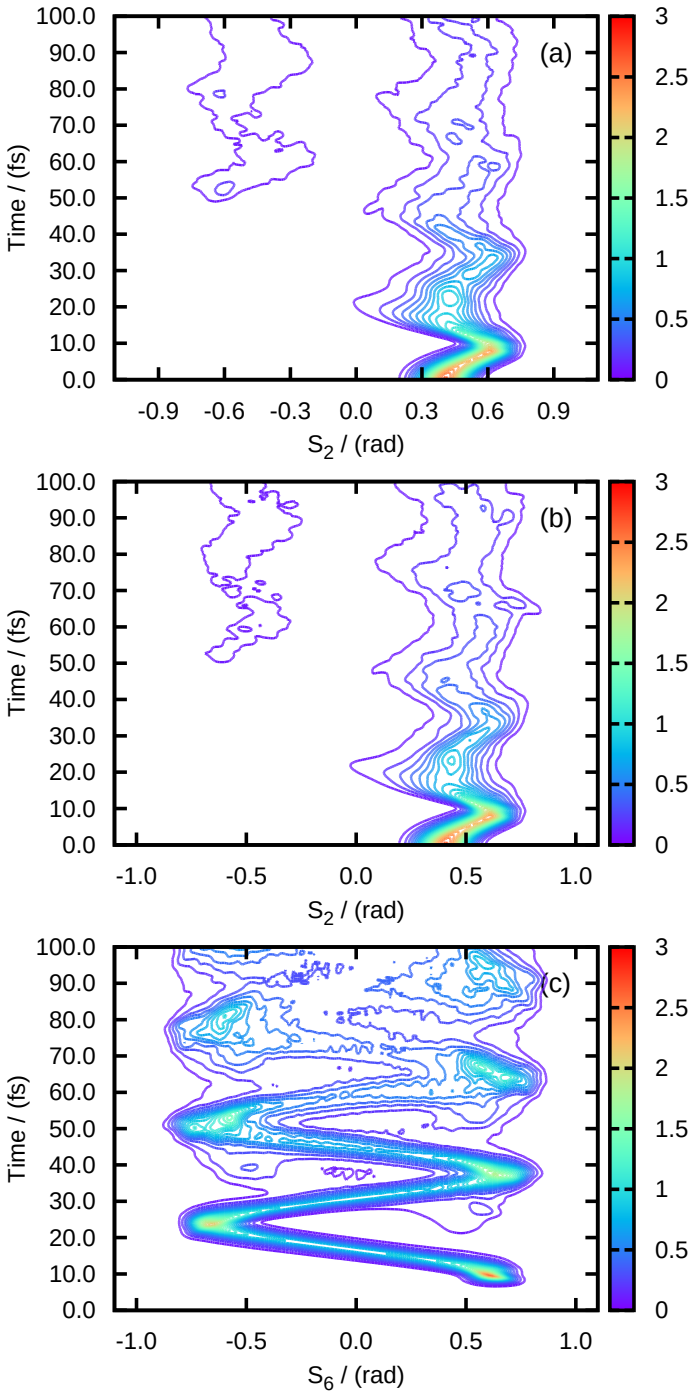

Figure C.1: Density contour plots of the wave packet for three lowest electronic states of NH_3^+ as functions of the S_2 coordinates and time.

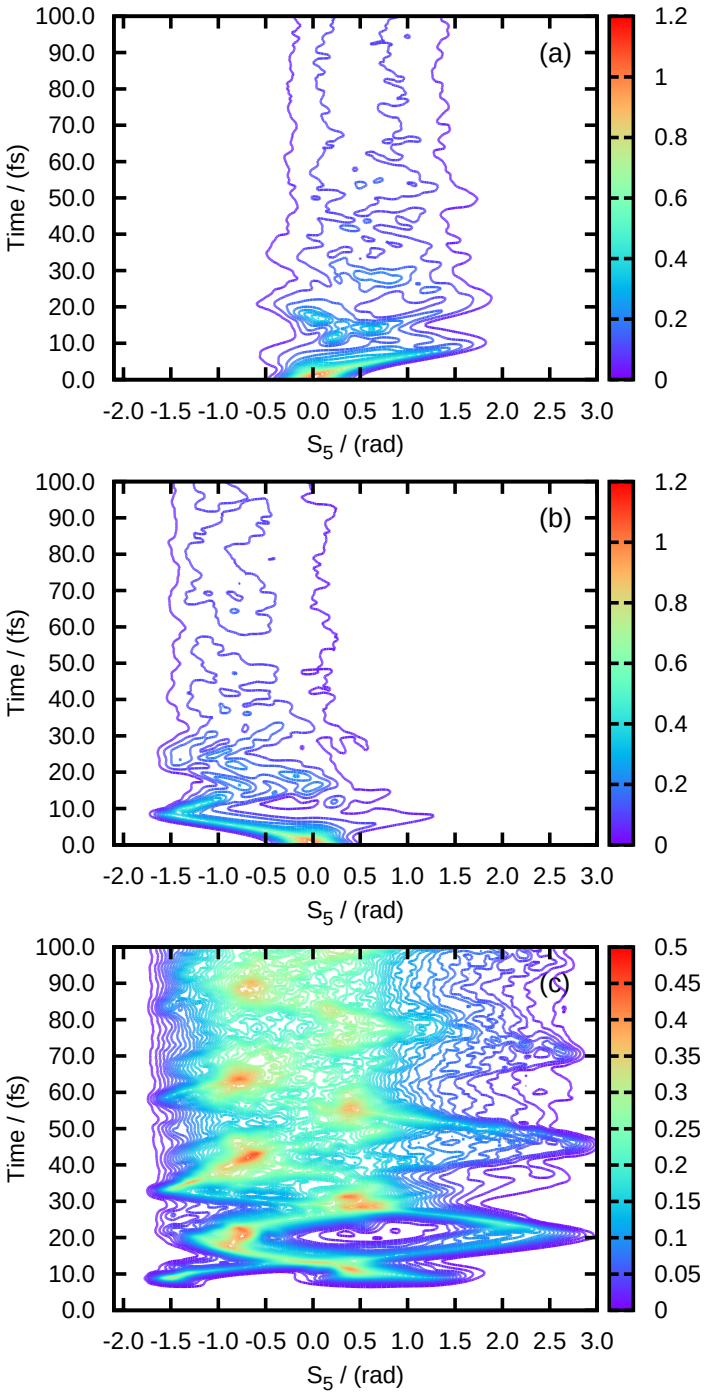

Figure C.2: Density contour plots of the wave packet for three lowest electronic states of NH_3^+ as functions of the S_5 coordinates and time.

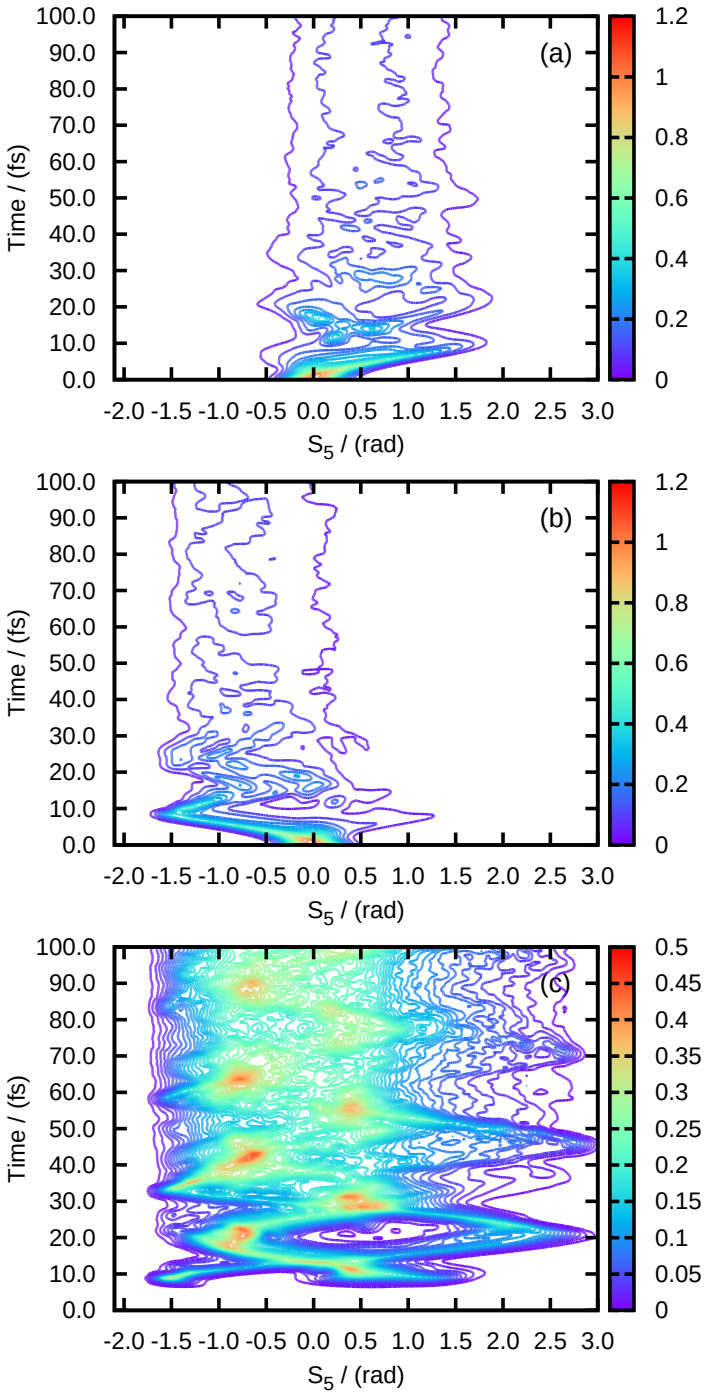

Figure C.3: Density contour plots of the wave packet for three lowest electronic states of NH_3^+ as functions of the S_6 coordinates and time.

Bibliography

[1] H. A. Jahn and E. Teller, in *Proc. Roy. Soc. London A* (The Royal Society, 1937), vol. 161, pp. 220–235.

[2] H. Jahn, in *Proc. Roy. Soc. London A* (1938), vol. 164, p. 117.

[3] H. Kramers, Proc. Akad. Sci. Amst. **33**, 959 (1930).

[4] M. Born and R. Oppenheimer, Ann. Physik **389**, 457 (1927).

[5] W. Domcke, D. Yarkony, and H. Köppel, *Conical intersections: electronic structure, dynamics & spectroscopy*, vol. 15 (World Scientific, 2004).

[6] W. Domcke, D. R. Yarkony, and H. Köppel, *Conical intersections: theory, computation and experiment*, vol. 17 (World Scientific, 2011).

[7] M. H. Perrin and M. Gouterman, J. Chem. Phys. **46**, 1019 (1967).

[8] J. H. Van der Waals, A. M. D. Berghuis, and M. S. De Groot, Mol. Phys. **13**, 301 (1967).

[9] H. Köppel, W. Domcke, and L. S. Cederbaum, Adv. Chem. Phys. **57**, 59 (1984).

[10] H. C. Longuet-Higgins, in *Advances in Spectroscopy*, edited by H. W. Thompson (Interscience, New York, 1961), vol. II.

[11] M. D. Sturge, Solid State Phys. **20**, 91 (1968).

[12] R. Englman, *The Jahn-Teller Effect in Molecules and Crystals* (Wiley-Interscience, New York, 1972).

[13] M. C. M. O'Brien, Journal of Physics C: Solid State Physics **5**, 2045 (1972).

[14] I. B. Bersuker and V. Z. Polinger, *Vibronic Interactions in Molecules and Crystals* (Springer-Verlag, Berlin, 1989).

[15] I. B. Bersuker, Chem. Rev. **101**, 1067 (2001).

[16] B. E. Applegate, T. A. Barckholtz, and T. A. Miller, Chem. Soc. Rev. **32**, 38 (2003).

[17] H. Köppel, L. S. Cederbaum, and S. Mahapatra, in *Handbook of High-resolution Spectroscopy*, edited by M. Quack and F. Merkt (Wiley, New York, 2011).

[18] I. B. Bersuker, *The Jahn-Teller Effect* (Cambridge University Press, 2006).

[19] H. Köppel, D. R. Yarkony, and H. Barentzen, *The Jahn-Teller Effect: Fundamentals and Implications for Physics and Chemistry*, vol. 97 (Springer Science & Business Media, 2009).

[20] J. Bednorz and K. Müller, Zeitschrift für Physik B Condensed Matter **64**, 189 (1986), ISSN 0722-3277.

[21] A. P. Ramirez, Journal of Physics: Condensed Matter **9**, 8171 (1997).

[22] A. Viel and W. Eisfeld, J. Chem. Phys. **120**, 4603 (2004).

[23] W. Eisfeld and A. Viel, J. Chem. Phys. **122**, 204317 (2005).

[24] D. Opalka and W. Domcke, J. Chem. Phys. **132**, 154108 (2010).

[25] D. Opalka and W. Domcke, Chem. Phys. Lett. **494**, 134 (2010).

[26] S. Bhattacharyya, D. Opalka, L. V. Poluyanov, and W. Domcke, J. Phys. Conf. Ser. **428**, 012015 (2013).

[27] S. Bhattacharyya, D. Opalka, L. V. Poluyanov, and W. Domcke, J. Phys. Chem. A **118**, 11962 (2014).

[28] S. Bhattacharyya, D. Opalka, and W. Domcke, Chem. Phys. (2015).

[29] L. D. Landau, Phys. Z. Sowjetunion **2**, 46 (1932).

[30] C. Zener, Proc. Roy. Soc. London A **137**, 696 (1932), ISSN 0950-1207.

[31] E. C. G. Stueckelberg, Helvetica Physica Acta **5**, 369 (1932).

[32] W. Domcke and G. Stock, Advances in Chemical Physics, Volume 100 pp. 1–169 (1997).

[33] K. Blum, *Density matrix theory and its application* (Plenum Press, New York, 1981).

[34] A. Kühl and W. Domcke, J. Chem. Phys. **116**, 263 (2002).

[35] H.-D. Meyer, U. Manthe, and L. S. Cederbaum, Chem. Phys. Lett. **165**, 73 (1990).

[36] U. Manthe, H.-D. Meyer, and L. S. Cederbaum, J. Chem. Phys. **97**, 3199 (1992).

[37] T. Venkatesan, S. Mahapatra, H.-D. Meyer, H. Köppel, and L. Cederbaum, J. Phys. Chem. A **111**, 1746 (2007).

[38] H. Köppel, M. Döscher, I. Baldea, H.-D. Meyer, and P. G. Szalay, J. Chem. Phys. **117**, 2657 (2002).

[39] I. Baldea and H. Köppel, J. Chem. Phys. **124**, 064101 (2006).

[40] S. Mahapatra and H. Köppel, J. Chem. Phys. **109**, 1721 (1998).

[41] A. Viel, W. Eisfeld, S. Neumann, W. Domcke, and U. Manthe, J. Chem. Phys. **124**, 214306 (2006).

[42] S. Bhattacharyya, Z. Dai, and W. Domcke, J. Chem. Phys. **143**, 194301 (2015).

[43] M. Born and K. Huang, *Dynamical theory of crystal lattices* (Oxford university press, 1998).

[44] C. Ballhausen and A. E. Hansen, Ann. Rev. Phys. Chem. **23**, 15 (1972).

[45] T. Azumi and K. Matsuzaki, Photochemistry and Photobiology **25**, 315 (1977).

[46] E. B. Wilson, J. C. Decius, and P. C. Cross, *Molecular Vibrations: The Theory of Infrared and Raman Vibrational Spectra* (Dover Publications, New York, 1980).

[47] G. Herzberg, *Molecular spectra and molecular structure* (Van Nostrand reinhold Company, New York, 1966).

[48] A. C. Albrecht, J. Chem. Phys. **33**, 156 (1960).

[49] F. S. Ham, Int. J. Quant. Chem. **5**, 191 (1971).

[50] A. C. Albrecht, J. Chem. Phys. **34**, 1476 (1961).

[51] W. Lichten, Phys. Rep. **164**, 131 (1967).

[52] F. T. Smith, Phys. Rep. **179**, 111 (1969).

[53] M. Baer, Chem. Phys. Lett. **35**, 112 (1975).

[54] M. Baer, *Beyond Born-Oppenheimer: electronic nonadiabatic coupling terms and conical intersections* (John Wiley & Sons, 2006).

[55] T. Pacher, L. S. Cederbaum, and H. Köppel, Adv. Chem. Phys. **84**, 293 (1993).

[56] C. A. Mead and D. G. Truhlar, J. Chem. Phys. **77**, 6090 (1982).

[57] F. A. Cotton, *Chemical applications of group theory* (Wiley, New York, 1990).

[58] D. Gay and E. Ascher, Linear and Multilinear Algebra **18**, 91 (1985).

[59] E. Ascher and D. Gay, J. Phys. A: Math. Gen. **18**, 397 (1985).

[60] P. R. Bunker and P. Jensen, *Molecular symmetry and spectroscopy*, vol. 2 (NRC Research Press, 1998).

[61] H. Derksen and G. Kemper, *Computational Invariant Theory, Volume 130 of Encyclopaedia of Mathematical Sciences* (Springer, New York, 2002).

[62] D. Hilbert, Math. Ann. **42**, 313 (1893).

[63] E. Noether, Math. Ann. **77**, 89 (1915).

[64] W. Decker, G.-M. Greuel, G. Pfister, and H. Schönemann, SINGULAR *3-0-4 — A computer algebra system for polynomial computations*, `http://www.singular.uni-kl.de` (2007).

[65] A. E. Heydtmann, `finvar.lib` *A* SINGULAR *4-0-2 library for computing invariant rings of finite groups* (2008).

[66] B. J. Braams and J. M. Bowman, International Reviews in Physical Chemistry **28**, 577 (2009).

[67] H. Weyl, *The Classical Groups, Their Invariants and Representations* (Princeton University Press, 1946).

[68] D. J. Tannor, *Introduction to quantum mechanics A Time-Dependent Perspective* (University Science Books, Sausalito, California, 2007).

[69] R. Schinke, *Photodissociation Dynamics: Spectroscopy and Fragmentation of Small Polyatomic Molecules*, 1 (Cambridge University Press, 1995).

[70] W. Domcke, in *Conical intersections: electronic structure, dynamics & spectroscopy*, edited by W. Domcke, D. Yarkony, and H. Köppel (World Scietific, 2004), vol. 15.

[71] M. R. Brill, F. Gatti, D. Lauvergnat, and H.-D. Meyer, Chemical Physics **338**, 186 (2007).

[72] H.-D. Meyer, F. Gatti, and G. A. Worth, *Multidimensional quantum dynamics* (WILEY-VCH, Weinheim, 2009).

[73] A. Askar and A. S. Cakmak, J. Chem. Phys. **68**, 2794 (1978).

[74] U. Manthe and H. Köppel, J. Chem. Phys. **93**, 345 (1990).

[75] H. Tal-Ezer and R. Kosloff, J. Chem. Phys. **81**, 3967 (1984).

[76] G. G. Balint-Kurti, Int. Rev. Phys. Chem. **27**, 507 (2008).

[77] S. K. Gray, J. Chem. Phys. **96**, 6543 (1992).

[78] S. K. Gray and G. G. Balint-Kurti, J. Chem. Phys. **108**, 950 (1998).

[79] R. Chen and H. Guo, J. Chem. Phys. **105**, 3569 (1996).

[80] P. A. M. Dirac, Math. Proc. Cambridge Philos. Soc. **26**, 376 (1930).

[81] J. Frenkel, *Wave Mechanics: Advanced General Principles* (Clarendon Press, Oxford, 1934).

[82] J. Kucar, H.-D. Meyer, and L. Cederbaum, Chem. Phys. Lett. **140**, 525 (1987).

[83] H.-D. Meyer, U. Manthe, and L. S. Cederbaum, Chem. Phys. Lett. **165**, 73 (1990).

[84] U. Manthe, H.-D. Meyer, and L. Cederbaum, J. Chem. Phys. **97**, 9062 (1992).

[85] M. H. Beck, A. Jäckle, G. Worth, and H.-D. Meyer, Phys. Rep. **324**, 1 (2000).

[86] G. Worth, H.-D. Meyer, H. Köppel, L. Cederbaum, and I. Burghardt, Int. Rev. Phys. Chem. **27**, 569 (2008).

[87] P. García-Fernández, I. B. Bersuker, J. A. Aramburu, M. T. Barriuso, and M. Moreno, Phys. Rev. B **71**, 184117 (2005).

[88] A. V. Marenich and J. E. Boggs, Chem. Phys. Lett. **404**, 351 (2005).

[89] A. W. Hauser, C. Callegari, P. Soldán, and W. E. Ernst, Chem. Phys. **375**, 73 (2010).

[90] A. W. Hauser, G. Auböck, C. Callegari, and W. E. Ernst, J. Chem. Phys. **132**, 164310 (2010).

[91] P. Mondal, D. Opalka, L. V. Poluyanov, and W. Domcke, Chem. Phys. **387**, 56 (2011).

[92] P. Mondal, D. Opalka, L. V. Poluyanov, and W. Domcke, J. Chem. Phys. **136**, 084308 (2012).

[93] C. Woywod, S. Scharfe, R. Krawczyk, W. Domcke, and H. Köppel, J. Chem. Phys. **118**, 5880 (2003).

[94] S. Mahapatra, V. Vallet, C. Woywod, H. Köppel, and W. Domcke, Chem. Phys. **304**, 17 (2004).

[95] U. Höper, P. Botschwina, and H. Köppel, J. Chem. Phys. **112**, 4132 (2000).

[96] P. Cassam-Chenaï and F. Patras, J./ Math./ Chem. **44**, 938 (2008).

[97] M. Z. Zgiersky and M. Pawlikowski, J. Chem. Phys. **70**, 3444 (1979).

[98] E. Haller, H. Köppel, L. S. Cederbaum, W. von Niessen, and G. Bieri, J. Chem. Phys. **78**, 1359 (1983).

[99] S. Faraji, H. Köppel, W. Eisfeld, and S. Mahapatra, Chem. Phys. **347**, 110 (2008).

[100] Z. Shao, H. Li, S. Zhang, J. Li, Z. Dai, Y. Mo, Y. J. Bae, and M. S. Kim, J. Chem. Phys. **136**, 064308 (2012).

[101] L.-S. Wang, B. Niu, Y. Lee, D. Shirley, E. Ghelichkhani, and E. Grant, J. Chem. Phys. **93**, 6318 (1990).

[102] R. Meiswinkel and H. Köppel, Chem. Phys. Lett. **201**, 449 (1993).

[103] D. Opalka, L. V. Poluyanov, and W. Domcke, J. Chem. Phys. **135**, 104108 (2011).

[104] S. Evans, P. Joachim, A. Orchard, and D. Turner, Int. J. Mass Spectrom. Ion Phys. **9**, 41 (1972), ISSN 0020-7381.

[105] C. R. Brundle, N. A. Kuebler, M. B. Robin, and H. Basch, Inorg. Chem. **11**, 20 (1972).

[106] H. Bock and H. Mueller, Inorg. Chem. **23**, 4365 (1984).

[107] D. E. Woon and T. H. Dunning Jr, J. Chem. Phys. **98**, 1358 (1993).

[108] H.-J. Werner, P. J. Knowles, R. Lindh, F. R. Manby, M. Schütz, P. Celani, T. Korona, G. Rauhut, R. D. Amos, A. Bernhardsson, et al., MOLPRO *version - 2006.1*, See http://www. molpro. net. (2006).

[109] J. Light, I. Hamilton, and J. Lill, J. Chem. Phys. **82**, 1400 (1985).

[110] D. O. Harris, G. G. Engerholm, and W. D. Gwinn, J. Chem. Phys. **43**, 1515 (1965).

[111] J. C. Slonczewski, Phys. Rev. **131**, 1596 (1963).

[112] G. Branton, D. Frost, C. McDowell, and I. Stenhouse, Chem. Phys. Lett. **5**, 1 (1970).

[113] A. W. Potts and W. C. Price, Proc. Roy. Soc. London A **326**, 181 (1972).

[114] R. Maripuu, I. Reineck, H. Ågren, W. Nian-Zu, J. M. Rong, H. Veenhuizen, S. Al-Shamma, L. Karlsson, and K. Siegbahn, Mol. Phys. **48**, 1255 (1983).

[115] R. G. Cavell and K. H. Tan, Chem. Phys. Lett. **197**, 161 (1992).

[116] J. Yang, J. Li, Y. Hao, C. Zhou, and Y. Mo, J. Chem. Phys. **125**, 054311 (2006).

[117] D. S. Marynick, J. Chem. Phys. **74**, 5186 (1981).

[118] S. Creve and M. T. Nguyen, J. Phys. Chem. A **102**, 6549 (1998).

[119] G. A. Worth, M. H. Beck, A. Jäckle, and H.-D. Meyer, The MCTDH Package, Version 8.2, (2000). H.-D. Meyer, Version 8.3 (2002), Version 8.4 (2007). Current version: 8.4.10 (2014). See http://mctdh.uni-hd.de.

[120] D. W. Turner, C. Baker, and C. R. Brundle, *Molecular Photoelectron Spectroscopy* (Wiley, London, 1970).

[121] M. Banna and D. Shirley, J. Chem. Phys. **63**, 4759 (1975).

[122] M. Piancastelli, C. Cauletti, and M.-Y. Adam, J. Chem. Phys. **87**, 1982 (1987).

[123] D. Edvardsson, P. Baltzer, L. Karlsson, B. Wannberg, D. Holland, D. Shaw, and E. Rennie, J. Phys. B **32**, 2583 (1999).

[124] E. Haller, L. Cederbaum, W. Domcke, and H. Köppel, Chem. Phys. Lett. **72**, 427 (1980).

[125] G. Dujardin and S. Leach, Can. J. Chem. **63**, 1386 (1985).

[126] L. V. Poluyanov and W. Domcke, Chem. Phys. **407**, 1 (2012).

[127] L. Cederbaum, W. Domcke, and H. Köppel, Chem. Phys. **33**, 319 (1978).

[128] I. Bersuker and S. Stavrov, Coord. Chem. Rev. **88**, 1 (1988).

[129] M. Pernpointner, T. Rapps, and L. S. Cederbaum, J. Chem. Phys. **129**, 174302 (2008).

[130] S. Mahapatra, G. Worth, H.-D. Meyer, L. Cederbaum, and H. Köppel, J. Phys. Chem. A **105**, 5567 (2001).